

**Nguyen Huy Bang**

**Investigation of electronic states of the NaLi  
molecule by polarization labelling spectroscopy**

**Doctoral dissertation written in the Institute of Physics, Polish Academy  
of Sciences under the supervision of Professor Włodzimierz Jastrzębski**



**October 2008**

*To my parents, my wife, and my sons*

## **Acknowledgments**

The four years of my PhD studies at the Institute of Physics, Polish Academy of Sciences (IF PAS) were very enjoyable, although often challenging. I found that every moment there was someone on whom I could rely on support, either for my research or my life. Without them, I would not have been able to finish this thesis. Therefore, I would like to take this chance to express my sincere thanks to all of them.

First and foremost, I am deeply grateful to my supervisor, Professor Włodzimierz Jastrzębski, for his enthusiasm, patience, support, insightful guidance, and mentoring of my doctoral study. It was he who introduced me into this fascinating field, guided me towards coherent thinking, and provided me with invaluable advice about the academic career. He patiently taught me laser spectroscopy techniques and ways to solve challenges in daily experimental work.

Very sincere thanks are due to Professor Paweł Kowalczyk for his support to perform part of experiments in his laboratory, reading of the manuscript and valuable comments.

Discussions with Dr Asen Pashov from Sophia University about numerical codes were valuable. I sincerely thank him for reading the manuscript, and his comments which make it clearer.

The construction of potential energy curves in terms of analytical functions was initially guided by Professor Robert J LeRoy of Waterloo University during his short visit in Warsaw. Discussions on analytical potential models were very fruitful. I am very grateful for his kind guidance and support.

I would like to thank Professor Cao Long Van for recommending me to the IP PAS. Sincere thanks are due to the IP PAS and Professor Maciej Kolwas for kindly providing me with the doctoral scholarship.

I would like to acknowledge my colleagues. Special thanks are due to P. Kortyka, M. Kubkowska, and A. Grochola for their helpful collaborations.

I greatly appreciate help from the staff at the IP PAS during my PhD study.

The support and encouragement by Professor Dinh Xuan Khoa from Vinh University during my PhD study are greatly acknowledged.

Last but not least, I would like to dedicate this thesis to my family. To my parents for their supports and encouragements. To my sons, Cong and Dung, with my all love. To Lan Anh, my wife, for her sacrifices for me, her love and understanding.

Nguyen Huy Bang

## **Abstract**

In this thesis we present the results of our experimental investigations of highly excited electronic states of the NaLi molecules. In the course of current investigations we observed for the first time four excited electronic states of  $^1\Pi$  symmetry. Measurements of rotationally resolved spectra were carried out with the V-type polarisation labelling technique and covered the 26000-36300  $\text{cm}^{-1}$  spectral region with resolution of better than 0.1  $\text{cm}^{-1}$ . The use of high power pulsed lasers enabled us to also record spectral lines resulting from very weak transition and finally to collect a comprehensive set of raw data which allowed performing several precise numerical analyses. In particular, the salient molecular (Dunham) constants and potential energy curves for the  $3^1\Pi$ ,  $4^1\Pi$ ,  $6^1\Pi$ , and  $7^1\Pi$  states were determined for the first time, while description of the  $4^1\Sigma^+$  state was considerably refined in comparison with the literature.

Comparison of the experimental results with theoretical ones has become possible only very recently, since first theoretical calculations dealing with these states appeared in August 2008, and were published by two independent groups. The present experimental results pose some intriguing questions about the assignment of the observed states and we hope that they will be explained by revisiting the theoretical calculations.

## **List of tables**

- 2.1. Correlations between molecular and atomic states (for unlike atoms).
- 2.2. Correlations between atomic and molecular multiplicities.
- 3.1. Relative intensities ( $\sqrt{I}$ ) in PLS spectrum when pumping via the  ${}^1\Pi \leftarrow {}^1\Sigma^+$  band.
- 3.2. Relative intensities ( $\sqrt{I}$ ) in PLS spectrum when pumping via the  ${}^1\Sigma^+ \leftarrow {}^1\Sigma^+$  band.
- 3.3. Relative intensities ( $\sqrt{I}$ ) in PLS spectrum when pumping via the  ${}^1\Pi \leftarrow {}^1\Sigma^+$  band.
- 3.4. Relative intensities ( $\sqrt{I}$ ) in PLS spectrum when pumping via the  ${}^1\Sigma^+ \leftarrow {}^1\Sigma^+$  band.
- 3.5. The laser lines used in this work as a probe.
- 4.1. Molecular constants of the  $4^1\Sigma^+$  state of NaLi.
- 4.2. The rotationless point-wise IPA potential of the  $4^1\Sigma^+$  state of NaLi.
- 4.3. Dunham coefficients of the  $3^1\Pi$  state of NaLi.
- 4.4. The RKR potential energy curve of the  $3^1\Pi$  state of NaLi.
- 4.5. The point-wise IPA potential energy of the  $3^1\Pi$  state of NaLi.
- 4.6. The parameters of the MLR{4, 5, 7} potential model of the  $3^1\Pi$  state of NaLi.
- 4.7. Molecular constants of the  $4^1\Pi$  state of NaLi.
- 4.8. The RKR potential of the  $4^1\Pi$  state of NaLi.
- 4.9. The point-wise IPA potential of the  $6^1\Pi$  state of NaLi.
- 4.10. Molecular constants of the  $6^1\Pi$  and  $7^1\Pi$  states of NaLi.
- 4.11. The RKR potentials of the  $6^1\Pi$  and  $7^1\Pi$  states of NaLi.
- 4.12. The point-wise IPA potential of the  $6^1\Pi$  state of NaLi.
- 4.13. The point-wise IPA potential of the  $7^1\Pi$  state of NaLi.
- 4.14. Theoretical and experimental molecular constants of the  $4^1\Sigma^+$ ,  $3^1\Pi$ ,  $4^1\Pi$ ,  $6^1\Pi$  and  $7^1\Pi$  states of NaLi.

## List of figures

- 2.1. Coupling diagram of the angular momenta in Hund's case (a).
- 2.2. The PEC of the  $1^1\Sigma^+$  state of the NaLi molecule calculated theoretically [24]. The equilibrium distance is  $R_e = 2.89 \text{ \AA}$ , and the dissociation energy  $D^e = 7057 \text{ cm}^{-1}$ .
- 2.3. Schematic outline of the algorithm for the IPA and DPotFit techniques.
- 2.4. Illustration of parity of rotational levels in the  $1^1\Sigma^+$ ,  $1^1\Sigma^-$ , and  $1^1\Pi$  states.
- 2.5. Potential energy diagrams with vertical transitions (Franck–Condon principle).
- 3.1. Scheme of the PLS method:  $P_1$  and  $P_2$  are the pair of crossed polarizers, D is detector employed to detect polarization signal of the probe beam.
- 3.2.  $M_J$  - dependence of absorption cross-section (blue curves) for transitions between Zeeman sublevels.
- 3.3. Excitation schemes in polarization labelling spectroscopy.
- 3.4. The three-section heat-pipe oven.
- 3.5. Experimental arrangement when the LD 500 dye laser system is used.
- 3.6. Experimental arrangement when the Frequency doubler-OPO/OPA system is used.
- 4.1. The PECs of the  $1-7^1\Pi$  and  $1-10^1\Sigma^+$  states of NaLi calculated by Mabrouk *et al* [79]. The blue curves stand for  $1^1\Sigma^+$  states, and the red ones stand for  $1^1\Pi$  states.
- 4.2. A part of the PLS spectrum that consists of P and R lines when pump beam is circularly polarized and probe at  $15486.1 \text{ cm}^{-1}$  excites simultaneously three transitions starting at levels (0,30), (1,21) and (1,40) in the ground state. The vibrational quantum numbers are denoted in figure.
- 4.3. Distribution of the experimental data in the field of quantum numbers of the  $4^1\Sigma^+$  state in NaLi.
- 4.4. Upper part: the solid curve represents the theoretical PEC for the  $4^1\Sigma^+$  state calculated in [24], the solid-circle represents the IPA potential curve covered by experimental data, and the circles represent the extrapolation of the IPA potential. Bottom: the dot-star represents difference in energy between the current IPA potential and the previous one [18].
- 4.5. A part of the PLS spectrum of the  $3^1\Pi \leftarrow 1^1\Sigma^+$  transitions observed in cases of linearly (upper) and circularly (lower) polarized pumping light. In both cases the probe line is set at 496.5 nm, thus labels level (0, 30) of the ground state.

- 4.6. The envelope function (dashed) of the square of the FCFs (grey bar) and intensity distribution of the observed spectral lines when labelling at level (1, 25).
- 4.7. Distribution of the experimental data in the field of quantum numbers of the  $3^1\Pi$  state in NaLi.
- 4.8. Plot  $R^6[D^e - U_{MLR}(R)]$  versus  $1/R^2$  for different combinations of  $\{p, NS, NL\}$  parameters in the MLR potential function.
- 4.9. Upper: the analytical MLR $\{4, 5, 7\}$  potential of the  $3^1\Pi$  state of NaLi. Lower: the curve of difference in energy between the IPA and MLR $\{4, 5, 7\}$  potentials.
- 4.10. Lambda-doubling strength function of the  $3^1\Pi$  state of NaLi.
- 4.11. A part of PLS spectrum consists of  $P$ -,  $Q$ -, and  $R$ -lines of the  $4^1\Pi \leftarrow 1^1\Sigma^+$  band in NaLi, observed in case of linearly polarized pump beam and 496.5 nm probe laser line.
- 4.12. Distribution of the experimental data in the field of quantum numbers of the  $4^1\Pi$  state in NaLi.
- 4.13. The IPA potential of the  $4^1\Pi$  state of NaLi, the red-solid circles stand for region covered by experimental data, and the blue circles stand for extrapolation region.
- 4.14. Parts of PLS spectrum of the  $6^1\Pi \leftarrow 1^1\Sigma$  band (red) and  $7^1\Pi \leftarrow 1^1\Sigma$  (blue) observed in the case of linearly polarized pump beam and  $15539.3 \text{ cm}^{-1}$  probe laser line. The labelled level in this case is  $v'' = 0$  and  $J'' = 22$  in the ground state. Vibrational quantum numbers of the progressions are indicated in figure.
- 4.15. Distribution of the experimental data in the field of quantum numbers of the  $6^1\Pi$  state in NaLi.
- 4.16. Distribution of the experimental data in the field of quantum numbers of the  $7^1\Pi$  state in NaLi.
- 4.17. The IPA potential curves of the  $6^1\Pi$  and  $7^1\Pi$  states of NaLi
- 4.18. The potential energy curves of the  $4^1\Sigma^+$  and  $3-7^1\Pi$  states of NaLi calculated [79] (the solid curves) and in our work (the solid-circles). The  $5^1\Pi$  state has not been observed in our experiment.
- 4.19. The theoretical potential energy curves of the  $4^1\Sigma^+$  and  $3-7^1\Pi$  states from [80] (the solid curves) and the experimental ones (the solid-circles).
- 4.20. The theoretical potential curves of the  $5-7^1\Pi$  states in [79] and [80], and the IPA potential curves of the  $6^1\Pi$  and  $7^1\Pi$  states determined in this work.

<b>Contents</b>		<b>Page</b>
<b>Abstract</b>		
<b>List of tables</b>		
<b>List of figures</b>		
<b>1. Introduction</b>		<b>1</b>
<b>2. Spectra of diatomic molecules and interpretation of experimental data .....</b>		<b>5</b>
2.1. Angular momenta and classification of electronic states .....		5
2.2. Correlations between atomic and molecular states .....		7
2.3. Schrödinger equation within the Born-Oppenheimer approximation .....		9
2.4. Molecular constants and models of the potential .....		12
2.4.1 <i>Molecular constants</i> .....		12
2.4.2 <i>Dunham expansion</i> .....		15
2.4.3 <i>Morse and Hulbert-Hirschfelder potentials</i> .....		17
2.4.4 <i>RKR potential</i> .....		18
2.4.5 <i>Long-range behaviour of potential energy curves</i> .....		19
2.4.6 <i>Inverse perturbation approach and direct potential fit</i> .....		21
2.5. Selection rules for optical transitions .....		23
2.5.1 <i>Total parity and general selection rules</i> .....		23
2.5.2 <i>Selection rules</i> .....		25
2.5.3 <i>Franck-Condon principle</i> .....		26
2.6. Perturbations in molecular spectra.....		27
2.6.1 <i>Electrostatic and non-adiabatic perturbations</i> .....		27
2.6.2 <i>Spin-orbit coupling</i> .....		29
2.6.3 <i>Rotational perturbations</i> .....		30

<b>3. Polarization labelling spectroscopy and experimental arrangement.....</b>	<b>33</b>
3.1. Polarization labelling spectroscopy .....	33
3.1.1 <i>Basic principles</i> .....	33
3.1.2 <i>Amplitude of polarization signal</i> .....	35
3.1.3 <i>Excitation schemes</i> .....	38
3.1.4 <i>Relative intensities of spectral lines</i> .....	39
3.2. Experimental.....	42
3.2.1 <i>Preparation of NaLi molecules</i> .....	42
3.2.2 <i>Laser sources</i> .....	44
3.2.3 <i>Experimental arrangement</i> .....	45
3.3. Determination of the absolute wavelength in PLS spectrum .....	47
<b>4. Experimental results for the NaLi molecule .....</b>	<b>48</b>
4.1. Introduction .....	48
4.1.1 <i>Historical overview of investigations of NaLi</i> .....	48
4.1.2 <i>Outline of the electronic states observed in this work</i> .....	51
4.2. Methods of data analysis.....	52
4.3. The $4^1\Sigma^+$ state .....	53
4.3.1 <i>Observation and assignment of the spectra</i> .....	53
4.3.2 <i>Molecular constants</i> .....	55
4.3.3 <i>Potential energy curve</i> .....	56
4.4. The $3^1\Pi$ state .....	59
4.4.1 <i>Observation and assignment of the spectra</i> .....	59
4.4.2 <i>Dunham coefficients</i> .....	62
4.4.3 <i>Potential energy curve</i> .....	63
4.5. The $4^1\Pi$ state .....	71
4.5.1 <i>Observation and assignment of the spectra</i> .....	71
4.5.2 <i>Dunham coefficients</i> .....	72
4.5.3 <i>Potential energy curve</i> .....	73
4.6. The $5^1\Pi$ and $6^1\Pi$ states .....	76

4.6.1	<i>Observation and assignment of the spectra</i> .....	76
4.6.2	<i>Dunham coefficients</i> .....	78
4.6.3	<i>Potential energy curves</i> .....	79
4.7	Comparison of the current results with recent theoretical calculations.....	83
<b>5.</b>	<b>Summary and conclusions</b> .....	<b>87</b>
	<b>Bibliography</b> .....	<b>91</b>

---

## Chapter 1

### Introduction

The alkali-metal diatomic molecules (dimers) have been for a long time very attractive both for the theoreticians and experimentalists because they have a relatively simple electronic structure. Their electronic structure is frequently considered by theoreticians as a very convenient model for introducing and testing of several approximations which can be further applied to more complex molecular systems. But the final verification of applied theoretical assumptions and approximations is always provided by experiment. From the experimental point of view alkali-metal dimers with their main absorption bands placed in the visible and UV regions are very convenient objects for investigations with modern laser spectroscopy techniques. Investigations of alkali-metal dimers have recently experienced additional impetus since Bose-Einstein condensate in dilute alkali-metal vapors was obtained [1] and presently there are many efforts to create ultra-cold molecules and molecular condensates consisting of different alkali-metal mixtures [2-8]. This makes the precision data delivered by spectroscopists crucial for planning and interpretation of this new class of experiments. The heteronuclear cold molecules are considered to be particularly interesting because they possess a permanent dipole moment and can therefore interact (be manipulated) with external electric fields.

Among alkali-metal dimers, the knowledge of the electronic structure of heteronuclear molecules is less advanced than for homonuclear ones. In particular for NaLi, the lightest and simplest heteronuclear alkali-metal dimer, the number of investigated electronic states is quite modest. The first experimental observation of the spectrum of this molecule was reported only in 1971 by Hessel [11] while other dimers were observed experimentally as early as 1928 [9]. Up to now, only few singlet-electronic states have been studied experimentally [12-18]. On the theoretical side, the pioneering study of the NaLi molecule was performed by Bertocini *et al* [19] in 1970. After that

several research groups used ab initio techniques to explore the electronic structure of this molecule [20-24]; the most systematic and accurate were carried out by Schmidt-Mink *et al* [24] and concerned the first sixteen singlet and triplet states of NaLi. Relatively poor knowledge of the electronic structure of the NaLi molecule when compared with those for the other dimers was one of the motivations of the present study. But it is also worth mentioning at this point that Li and Na atoms have been already simultaneously trapped and cooled in a magneto-optical trap (MOT) [4-6] which gives good prospects for further work on cold NaLi in the near future.

Growing interest in the NaLi molecule resulted very recently (June and August 2008) in two new theoretical papers [79, 80] by two independent research teams. For the first time the authors give comprehensive descriptions of highly excited states, particularly of those that were for the first time investigated experimentally in the present study. Since theoretical results presented in both papers differ considerably this makes comparison with our results particularly relevant, and therefore we anticipate that the existing discrepancy between the two theoretical predictions will be explained by theoreticians.

In fact we carried out our experiments much earlier, before the theoretical calculations were made and we were able to interpret and assign the observed spectral lines to individual electronic states on the basis of results of our experiments, analysed by numerical algorithms developed in our laboratory. Presently, when we have two theoretical sources for comparison we are able to critically evaluate them.

In order to attempt experimental investigations of the NaLi molecule one has to find a way to form a sufficiently dense sample of the molecules and then to selectively observe the spectra originating from the NaLi molecule, even though they coexist with the Na<sub>2</sub> and Li<sub>2</sub> ones. The main problem in production of NaLi molecules comes from a big difference of melting temperatures of metallic sodium and lithium resulting in big difference of Na and Li densities in the gas phase. In the present experiment we overcame this difficulty by using a special design of a heat-pipe oven, similar to the construction already proved in investigations of KLi molecules [32]. Furthermore, selective observations of NaLi spectra were carried out by means of polarization labelling spectroscopy (PLS). Originally this method was invented by Schawlow and Hänsch [27] and with some modifications [28] has been used in Warsaw for investigations of Li<sub>2</sub> [29], Na<sub>2</sub> [30], K<sub>2</sub> [31], NaK [31], KLi [32] and NaRb [33]. The method depends on the use of two lasers: one selectively labels molecular levels while the other one induces optical

transitions from labelled levels to the investigated electronic state. By proper choice of the wavelength of the labelling laser we could strongly suppress unwanted spectra of homonuclear molecules thus making the analysis feasible. The experiment was performed using the polarization labeling spectroscopy technique, in a version based on the V-type optical - optical double resonance scheme.

The analysis of raw data and finally the description of the electronic states were performed by several methods with computer codes already developed in our laboratory. First of all we identified in the recorded spectra spectral lines corresponding to the investigated states and assigned quantum numbers of levels involved in each transition. For all states molecular constants (Dunham coefficients) were determined. Potential energy curves were then constructed numerically by different methods: semiclassical one (RKR, based WKB approximation), by fully quantum inverted perturbation approach technique [54, 55] (IPA, point-wise implementation [57]) and in the case of one state with the direct-potential-fit technique (DPotFit, with codes from [58]). The most reliable and accurate potential energy curves capable of reproducing experimental data within the demanded accuracy were obtained with the IPA technique and together with the molecular constants were the subject of comparison with the theoretical results.

In this thesis the results of experimental investigation by means of the PLS technique on the  $4^1\Sigma^+$ ,  $3^1\Pi$ ,  $4^1\Pi$ ,  $6^1\Pi$ , and  $7^1\Pi$  states of NaLi are described. All  $^1\Pi$ -symmetry states mentioned above were observed for the first time. Some of these results were already published in the following papers:

1. Nguyen Huy Bang, W. Jastrzębski, and P. Kowalczyk. *New observation and analysis of the  $E(4)^1\Sigma^+$  state in NaLi*. **J. Mol. Spectr.** 233 (2005) 290-292.
2. Nguyen Huy Bang, A. Grochola, W. Jastrzębski, P. Kowalczyk, and H. Salami. *Investigation of a highly excited electronic  $^1\Pi$  state of NaLi molecule*. **Optica Applicata** 36 N<sub>o</sub>4 (2006) 499-504.
3. Nguyen Huy Bang, A. Grochola, W. Jastrzębski, and P. Kowalczyk. *First observation of  $3^1\Pi$  and  $4^1\Pi$  states of NaLi molecule*. **Chem. Phys. Lett**, 440 (2007) 199-202.
4. Nguyen Huy Bang, A. Grochola, W. Jastrzębski, and P. Kowalczyk. *Spectroscopy of mixed alkali dimers by polarization labelling technique: application to NaLi and NaRb molecules*. **Opt. Mat.** (2008) in press.

**This thesis is organized in the following way:**

- **Chapter 2** is devoted to presentation of the basic information about the electronic structure of diatomic molecules, standard approximations made in descriptions of electronic states, selection rules for optical transitions and different techniques of processing and interpretation of experimental data (i.e. molecular constants and potential energy curves). Additionally some information about the origin of perturbations of molecular levels is presented.
- **Chapter 3** discusses the basic concepts of polarization labelling spectroscopy, presents comparison of different schemes which can be used in experiments and of relative intensities of spectral lines (polarization signal) observed for different arrangements of polarization and different symmetry of states involved in labelling process. Also a short description of the main parts of the experimental set-up is given together with the procedure for precise frequency calibration of the spectra.
- **Chapter 4** collects results obtained for the  $4^1\Sigma^+$ ,  $3^1\Pi$ ,  $4^1\Pi$ ,  $6^1\Pi$ , and  $7^1\Pi$  states of NaLi with first comparison with theoretical predictions for these states. For each of the investigated states molecular (Dunham) constants and potential energy curves calculated with different methods are presented.
- **Chapter 5** includes conclusions, and discussion of discrepancies between experimental and theoretical results in a review of the most recent calculations.
- Finally there is a bibliography concerning literature presented in this thesis.

## Chapter 2

### Spectra of diatomic molecules and interpretation of experimental data

#### 2.1. Angular momenta and classification of electronic states

Consider a diatomic molecule that consists of two nuclei A and B surrounded by fast-moving electrons. If we disregard nuclear spin, which is responsible for the hyperfine structure, then there are three sources of angular momentum in a diatomic molecule: the spin of the electrons  $\vec{S}$ , the angular momenta due to orbital motion of electrons  $\vec{L}$ , and the rotation of the molecular framework  $\vec{R}$ . The nuclear charges produce an axial symmetric electric field about the internuclear axis. In such field the resultant electronic angular momentum  $\vec{L}$  precesses very fast about the axis. Hence, only the component  $M_L$  of  $\vec{L}$  along the internuclear axis is well defined. On the other hand, if one reverses the sense of moving direction of all electrons the sign of  $M_L$  is changed to  $-M_L$  but the energy of system will not be changed. Thus the states that differ only by the sign of  $M_L$  have the same energy (two-fold degeneracy) whereas the states with different values of  $|M_L|$  have in general different energies. Therefore it is convenient to classify the electronic states of diatomic molecules according to:

$$\Lambda = |M_L|, \Lambda = 0, 1, 2 \dots \text{ (in } \hbar \text{ unit)} \quad (2.1)$$

According to  $\Lambda = 0, 1, 2, 3 \dots$  the corresponding electronic states are denoted as  $\Sigma, \Pi, \Delta, \Phi, \dots$ . Among those, the  $\Pi, \Delta, \Phi, \dots$  states are doubly degenerated since  $M_L$  can have two  $+\Lambda$  and  $-\Lambda$  values, whereas the  $\Sigma$  states are non-degenerated.

In a diatomic molecule symmetric properties of electronic wavefunctions depend on the symmetry of the electric field in which the electrons move. Any plane through the internuclear axis is the plane of symmetry. Namely, the electronic wavefunctions either do not change or change their sign to opposite under a reflection of electronic coordinates in respect to the plane of symmetry. The first kind of states are classified as (+) parity

whereas the last one as (-) parity. The parity symbol (+/-) is placed as right superscript for the notation of electronic state. In addition to the plane of symmetry, homonuclear diatomic molecules also have a centre of symmetry (middle point of internuclear distance) which leaves the electric field unaltered under reflection of coordinates of the nuclei against this point. Upon such reflection the electronic wavefunctions either do not change or change their sign. The states belong to the first type are called *gerade* (labelled by right subscript *g*), and the states belong to the second type are called *ungerade* (right subscript *u*).

Whenever spin of electrons is taken in to account, the spin of individual electrons can form a resultant spin moment  $\vec{S}$  with the corresponding quantum number *S*. Since upon the orbital motion of electrons a magnetic field is produced along internuclear axis, this causes a precession of  $\vec{S}$  about the axis with a component along axis denoted by  $\Sigma$ . For a given value of *S* there are  $2S+1$  possible values of  $\Sigma$  which correspond to different energies for a given value of  $\Lambda$ . The value of  $2S+1$  called the multiplicity of the electronic state is marked as left superscript in the notation of electronic state,  $^{2S+1}\Lambda$ . In addition to the  $\Lambda$  and  $\Sigma$  quantum numbers in some notations also quantum number  $\Omega$  is used and defined as follows:

$$\Omega = | \Lambda + \Sigma |. \quad (2.2)$$

In spectroscopic nomenclature there are two ways to number electronic states: The first one is to label electronic states by letters in which *X* is for the ground state, while *A*, *B*, *C*, ... label successively excited states of the same multiplicity as the ground state. States with multiplicity different from that of the ground state are labelled with lowercase letters *a*, *b*, *c*, ... . An alternative way, becoming currently a standard one, is to label states of the same symmetry by integers: 1 for the state of lowest energy state of each multiplicity, and 2, 3, ... for the successive excited states (in each multiplicity-class).

The angular momenta described above are referred to fixed- molecular frame. Since the rotation of the molecule leads to a rotation of nuclear framework a rotational angular momentum  $\vec{R}$  perpendicular to the internuclear axis is formed. Therefore,  $\vec{\Omega}$  couples with  $\vec{R}$  (fig. 2.1) resulting in a total angular momentum  $\vec{J}$  determined by:

$$\vec{J} = \vec{R} + \vec{\Omega} = \vec{R} + \vec{\Lambda} + \vec{\Sigma}. \quad (2.3)$$

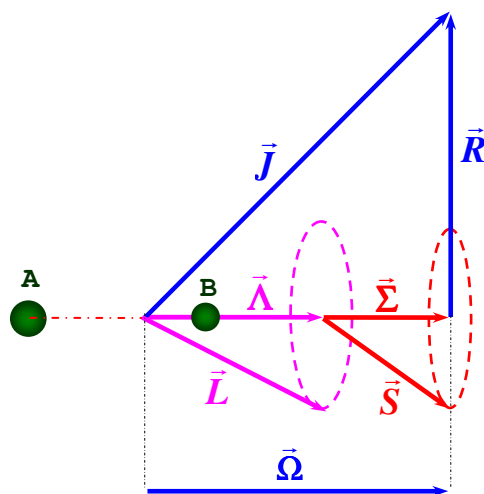


**Figure 2.1.** Coupling diagram of the angular momenta in Hund's case (a).

Such coupling scheme of angular momentums is known as Hund's case (a) [34] and it is a good approximation for many electronic states of diatomic molecules. Following this scheme the total angular momentum is quantized in a fixed free-space with the quantum number  $J$ . It is worth to point out that within the framework of Hund's case (a), the  $\{J, S, \Omega, \Lambda, \Sigma\}$  is a good set of quantum numbers to represent quantum states of rotating molecule. In addition to the Hund's case (a) coupling scheme there are also other coupling schemes which are called Hund's case (b), (c), and (d) [34].

## 2. 2. Correlations between atomic and molecular states

In diatomic molecules correlations between atomic and molecular states might be derived within the separated-atom model [34]. Following assumptions of this model, couplings between angular momenta in the constituent atoms are assumed to obey the Russell-Saunders scheme, where atomic states are determined in the central field approximation [36]. By adding the components (along the internuclear axis) of the total angular momenta of individual atoms one can obtain several possible values of  $\Lambda$  giving rise to different molecular electronic states. The parity in particular case of  $\Sigma$ -symmetry states is determined according to parity of electronic atomic states and total angular momentum of atoms, following Wigner and Witmer correlation rules [34]. Namely, the parity of the  $\Sigma$  states depends on  $L_A + L_B + \sum l_{iA} + \sum l_{iB}$ , where  $L_k$  is total angular

momentum of atom  $k$  ( $k = A, B$ );  $\sum l_{iA}$  and  $\sum l_{iB}$  are the parities of atomic state of A- and B- atom, respectively. If the total value of the above expression is even the parity of  $\Sigma$  states is (+), otherwise it is (-). In table 2.1, there is a list of correlations between atomic and molecular states in some cases of unlike atoms.

**Table 2.1.** Correlations between molecular and atomic states (for unlike atoms) [34]

Atomic states	Resulting molecular states
$S_g + S_g$ or $S_u + S_u$	$\Sigma^+$
$S_g + S_u$	$\Sigma^-$
$S_g + P_g$ or $S_u + P_u$	$\Sigma^-, \Pi$
$S_g + P_u$ or $S_u + P_g$	$\Sigma^+, \Pi$
$S_g + D_g$ or $S_u + D_u$	$\Sigma^+, \Pi, \Delta$
$S_g + D_u$ or $S_u + D_g$	$\Sigma^-, \Pi, \Delta$
$S_g + F_g$ or $S_u + F_u$	$\Sigma^-, \Pi, \Delta, \Phi$
$S_g + F_u$ or $S_u + F_g$	$\Sigma^+, \Pi, \Delta, \Phi$
$P_g + P_g$ or $P_u + P_u$	$\Sigma^+(2), \Pi(2), \Delta$
$P_g + P_u$	$\Sigma^+, \Sigma^-(2), \Pi(2), \Delta$
$P_g + D_g$ or $P_u + D_u$	$\Sigma^+, \Sigma^-(2), \Pi(3), \Delta(2), \Phi$
$P_g + D_u$ or $P_u + D_g$	$\Sigma^+(2), \Sigma^-, \Pi(3), \Delta(2), \Phi$
$P_g + F_g$ or $P_u + F_u$	$\Sigma^+(2), \Sigma^-, \Pi(3), \Delta(3), \Phi(2), \Gamma$
$P_g + F_u$ or $P_u + F_g$	$\Sigma^+, \Sigma^-(2), \Pi(3), \Delta(3), \Phi(2), \Gamma$

The correlations between atomic and molecular multiplicities might be derived from the analysis of possible combinations giving the certain total spin and can be readily determined as in table 2.2.

**Table 2.2.** Correlations between atomic and molecular state multiplicities [34]

Atomic states	Resulting molecular states
Singlet + Singlet	Singlet
Singlet + Doublet	Doublet
Singlet + Triplet	Triplet
Doublet + Doublet	Singlet, triplet
Doublet + Triplet	Doublet, quartet
Doublet + Quartet	Triplet, quintet
Triplet + triplet	Singlet, triplet, quintet
Triplet + quartet	Doublet, quartet, sextet
Quartet + quartet	Singlet, triplet, quintet, septet

### 2.3. Schrödinger equation within the Born-Oppenheimer approximation

Consider a molecule consisting of  $n$  electrons and two nuclei,  $A$  and  $B$ . In a laboratory frame the non-relativistic Schrödinger equation of the system can be written as

$$\hat{\mathbf{H}}\Psi = E\Psi. \quad (2.4)$$

Here,  $\Psi$  - total wavefunction,  $\hat{\mathbf{H}}$  - the total Hamiltonian operator which consists of kinetic energy operator of nuclei ( $\hat{\mathbf{T}}^{\text{N}}$ ), interaction potential between the two nuclei ( $\mathbf{V}^{\text{NN}}$ ) and the Hamiltonian of electrons ( $\hat{\mathbf{H}}^{\text{el}}$ ). In details the total Hamiltonian is written by:

$$\hat{\mathbf{H}} = \hat{\mathbf{T}}^{\text{N}} + \mathbf{V}^{\text{NN}} + \hat{\mathbf{H}}^{\text{el}}, \quad (2.5)$$

$$\hat{\mathbf{T}}^{\text{N}} = -\frac{\hbar^2}{2} \left( \frac{\nabla_A^2}{M_A} + \frac{\nabla_B^2}{M_B} \right), \quad (2.6)$$

$$\mathbf{V}^{\text{NN}} = \frac{Z_A Z_B e^2}{R}, \quad (2.7)$$

$$\hat{\mathbf{H}}^{\text{el}} = -\frac{\hbar^2}{2m_e} \sum_{i=1}^n \nabla_i^2 - \sum_{i=1}^n \left[ \frac{Z_A e^2}{r_{Ai}} + \frac{Z_B e^2}{r_{Bi}} \right] + \sum_{i < j=1}^n \frac{e^2}{r_{ij}}. \quad (2.8)$$

In the above expressions,  $i$  stands for the  $i^{\text{th}}$  electron,  $R$  is the internuclear distance,  $r_{ij}$  is relative distance between  $i^{\text{th}}$  electron and  $j^{\text{th}}$  particle (electron or nucleus),  $M$  and  $m_e$  are respectively masses of nucleus and electron;  $Z_A$  and  $Z_B$  are atomic numbers of the nuclei  $A$  and  $B$ , respectively.

In order to solve Eq. (2.4) Born and Oppenheimer proposed an approximation (so called Born-Oppenheimer approximation, abbreviated by BO) in which the motion of electrons and nuclei can be treated separately in two steps. In the first step it is recognized that the nuclei as much heavier than the electrons ( $\frac{m_e}{M} < 1/1800$ ) move very slowly in comparison to the electronic motion. Thus the kinetic energy operator of nuclei can be neglected when considering  $\hat{\mathbf{H}}^{\text{el}}$ . Therefore the total wavefunction can be factorised as product of the nuclear and electronic parts:

$$\Psi^{\text{tot}} \approx \Psi^{\text{BO}} = \psi(\vec{R}) \Phi(\vec{r}, R). \quad (2.9)$$

The electronic wavefunction  $\Phi(\vec{r}, R)$  depends parametrically on internuclear separation, and it satisfies the following equation:

$$\hat{\mathbf{H}}^{\text{el}}\Phi(\vec{r}, R) = \varepsilon(R)\Phi(\vec{r}, R), \quad (2.10)$$

where  $\varepsilon(R)$  is an eigenvalue of  $\hat{\mathbf{H}}^{\text{el}}$  at a fixed internuclear distance  $R$ ,  $\vec{r}$  - position vector of electron relative to nucleus. Taking into account the electrostatic internuclear repulsion  $V_m$  one can obtain a potential energy:

$$U(R) = \varepsilon(R) + V^{\text{NN}}(R). \quad (2.11)$$

The potential energy can be determined for various internuclear distances giving a potential energy curve (PEC). The potential energy curve describes the potential well in which the nuclei are bound together. As a second step within the BO approximation we consider motion of the nuclei described by the following equation:

$$[\hat{\mathbf{T}}^N + U(R)]\psi(\vec{R}) = E\psi(\vec{R}). \quad (2.12)$$

The kinetic energy operator  $\hat{\mathbf{T}}^N$  in Eq. (2.12) consists of translational, rotational and vibrational parts. Because the translational motion does not change relative energy levels in the molecule it can be separated out by transforming Eq. (2.12) into the centre of mass of the two nuclei [35]. In the spherical coordinates  $(r, \theta, \varphi)$  frame, by introducing phenomenologically spin of electrons and assuming angular momenta follow Hund's case (a), the kinetic energy operator is given by:

$$\hat{\mathbf{T}}^N = -\frac{\hbar^2}{2\mu} \left[ \frac{\partial^2}{\partial R^2} + \frac{2}{R} \frac{\partial}{\partial R} \right] + \frac{\hbar^2}{2\mu R^2} \bar{\mathbf{R}}^2, \quad (2.13)$$

where  $\mu$  is the reduced mass of the nuclei:

$$\mu = \frac{M_A M_B}{M_A + M_B}. \quad (2.14)$$

The first grouped term in (2.13) describes motion of the nuclei along the internuclear axis, thus it is recognized as vibrational kinetic operator  $\hat{\mathbf{T}}^{\text{vib}}$  of the nuclei. The last term in

(2.13) depends on the rotational angular momentum  $\vec{R}$  and it is recognized as rotational kinetic operator  $\hat{T}^{\text{rot}}$ . Since the rotational and vibrational motions are separable the wavefunction  $\psi(r, \theta, \varphi)$  of the nuclei can therefore be factorized as the product of the vibrational and rotational parts:

$$\psi(R, \theta, \varphi) = \xi^{\text{vib}}(R) u^{\text{rot}}(\theta, \varphi) = \frac{1}{R} \chi(R) u^{\text{rot}}(\theta, \varphi). \quad (2.15)$$

The operator  $\hat{T}^{\text{rot}}$  acts on the wavefunction  $u^{\text{rot}}(\theta, \varphi)$  giving rotational energy given by:

$$E^{\text{rot}} = B[J(J+1) - \Omega^2 + S(S+1) - \Sigma^2], \quad (2.16)$$

where

$$B = \frac{\hbar^2}{2\mu R^2}. \quad (2.17)$$

Substituting (2.15) and (2.13) into (2.12) and regarding (2.16), we obtain:

$$\left\{ \frac{-\hbar^2}{2\mu R^2} \frac{d^2}{dR^2} + E^{\text{rot}} + U(R) \right\} \chi_q(R) = E_q \chi_q(R), \quad (2.18)$$

where,  $q$  stands for all quantum numbers representing the state of the molecule. The expression (2.18) is known as the Radial Schrödinger Equation (RSE) and describes rovibrational motion of the nuclei under an effective potential energy,  $U_{\text{eff}}(R)$ :

$$U_{\text{eff}}(R) = U(R) + E^{\text{rot}}. \quad (2.19)$$

For the singlet states ( $\Sigma = 0, \Omega = \Lambda$ ) the RSE is reduced to:

$$\left[ \frac{-\hbar^2}{2\mu} \frac{d^2}{dR^2} + B[J(J+1) - \Lambda^2] + U(R) \right] \chi_q(R) = E_q \chi_q(R). \quad (2.20)$$

It is worth to remark here that within the framework of the BO approximation the Schrödinger equation of a diatomic molecule is greatly simplified to the RSE from the Eq. (2.18). From the theoretical point of view, in order to calculate  $U(R)$  one needs to have a model that is capable to represent adequately interactions in the molecule (see [38], for example). The theoretical methods for calculations of potential energy curve are presented

in many textbooks and are beyond the scope of this thesis. From the experimental point of view, the determination of  $U(R)$  is carried out in a different way. Namely, from the experimentally observed spectral lines one can determine the energy levels of the molecule. Having energy levels it is possible to determine the potential energy curve of the molecule (see sect.2.4). Therefore such experimental potential curve besides giving spectroscopic characterization of the molecular state, also gives the way to compare experimental PEC with obtained theoretically.

In practice, the RSE (2.18) is well applicable to represent experimental level energies of heavy molecules. However, for light molecules like hydrides the RSE is often inadequate to describe experimental data because in these molecules the assumption for neglecting the kinetic energy of the nuclei when describing electrons motion is no longer valid. Therefore, in this case higher-order corrections must be taken in to account. These corrections will be presented in section 2.6.

## 2.4. Molecular constants and models of the potential

### 2.4.1 Molecular constants

In case of bound electronic states the PEC has the following common properties [34, 39-40] (fig. 2.2):

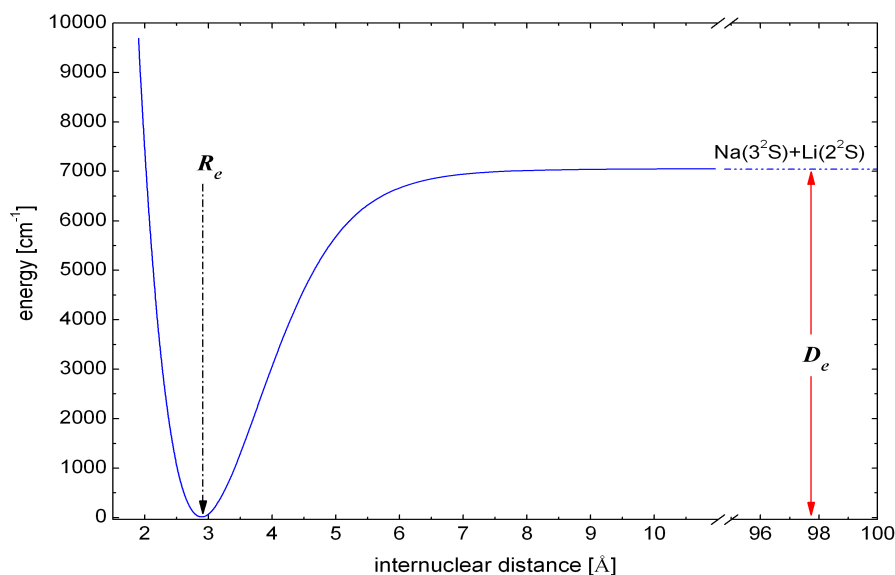


**Figure 2.2.** The PEC of the  $1^1\Sigma^+$  state of the NaLi molecule calculated theoretically [24]. The equilibrium distance is  $R_e = 2.89$  Å, and the dissociation energy  $D_e = 7057$  cm<sup>-1</sup>.

- It has a minimum at an equilibrium internuclear distance, denoted as  $R_e$ .
- It should approach asymptotically to a finite value as  $R$  goes to infinity. The energy which is needed to separate the atoms forming the molecule from the equilibrium distance to infinity is called dissociation energy, denoted by  $D^e$ .
- Around the equilibrium, the potential function behaves approximately as the harmonic one.
- It should become infinite at  $R = 0$ . This is merely a pure mathematic condition. The repulsive electrostatic force between the nuclei increases rapidly when nuclei approach each other from the equilibrium internuclear distance.

Following those properties, one can derive an expression of level energies. The potential energy function  $U(R)$  can be expanded in Taylor's series around the equilibrium internuclear distance:

$$U(R) = U(R_e) + U^{(1)}(R_e)(R - R_e) + \frac{1}{2!}U^{(2)}(R_e)(R - R_e)^2 + \frac{1}{3!}U^{(3)}(R_e)(R - R_e)^3 + \frac{1}{4!}U^{(4)}(R_e)(R - R_e)^4 + \dots, \quad (2.21)$$

where:

$$U^{(m)}(R_e) = \left. \frac{d^m U(R)}{dR^m} \right|_{R=R_e}, \quad m = 1, 2, \dots$$

In (2.21), the second term vanishes due to the minimum at  $R_e$ , the third term corresponds to harmonic potential with a *force constant*  $k = U^{(2)}(R_e)$ . By introducing a new variable  $y = R - R_e$  the expression (2.21) has a form as:

$$U(q) = U(0) + \frac{1}{2}ky^2 + \frac{1}{6}U^{(3)}(0)y^3 + \frac{1}{24}U^{(4)}(0)y^4 + \dots \quad (2.22)$$

The RSE (2.20) now becomes:

$$\left[ \frac{-\hbar^2}{2\mu} \frac{d^2}{dy^2} + \frac{\hbar^2}{2\mu} \frac{1}{(R_e + y)^2} [J(J+1) - \Lambda^2] + U(y) \right] \chi_q(y) = E_q \chi_q(y). \quad (2.23)$$

Around the equilibrium distance we can expand:

$$\frac{1}{(R_e + y)^2} = \frac{1}{R_e^2 \left(1 + \frac{y}{R_e}\right)^2} = \frac{1}{R_e} \left(1 - \frac{2y}{R_e} + \frac{3y^2}{R_e^2} - \dots\right). \quad (2.24)$$

In the zero-order approximation we retain the first two terms in (2.22) and the first term in (2.24) and then substituting them into (2.23) we obtain the so called spectroscopic term as follows:

$$T(v, J) = \frac{E_{v,J}}{hc} = T_e + \omega_e \left(v + \frac{1}{2}\right) + B_e [J(J+1) - \Lambda^2], \quad (2.25)$$

where

$$\omega_e = \frac{1}{2\pi\hbar c} \sqrt{k/\mu}, \quad (2.26)$$

$$B_e = \frac{\hbar}{4\pi c \mu R_e^2}. \quad (2.27)$$

The first term on the right-hand side of (2.25) is called electronic energy which corresponds to the value of potential energy at the equilibrium internuclear distance. The second term represents energy of harmonic oscillator with a vibrational constant  $\omega_e$  which relates to strength of chemical bonding between the two atoms. The last term is the energy due to the rotation of the molecule. It is described by a rotational constant  $B_e$  relating to bond length.

In the first-order approximation the expanded potential is retained up to  $y^4$  whereas expression (2.24) is retained up to  $y^2$ . Using perturbation theory, we obtain:

$$T(v, J) = T_e + \omega_e \left(v + \frac{1}{2}\right) - \omega_e x_e \left(v + \frac{1}{2}\right)^2 + B_e [J(J+1) - \Lambda^2] - D_e [J^2(J+1)^2 - \Lambda^2] - \alpha_e \left(v + \frac{1}{2}\right) [J(J+1) - \Lambda^2]. \quad (2.28)$$

The third term in (2.28) represents a contribution to the unharmonicity of the potential. In most cases  $\omega_e x_e > 0$  and  $\omega_e x_e \ll \omega_e$ , thus vibrational spacing decreases gradually as one approaches to higher vibrational levels. The fifth term in (2.28) is responsible for centrifugal effect due to the rotation of molecule. The last term in (2.28) represents coupling between rotations and vibrations.

In general, higher approximations can be carried out to obtain the higher corrections for the spectroscopic term. Following these, the spectroscopic term is given by [34]:

$$T(v, J) = T_e + G(v) + F_v(J), \quad (2.29)$$

where

$$G(v) = \omega_e(v + \frac{1}{2}) - \omega_e x_e(v + \frac{1}{2})^2 + \omega_e y_e(v + \frac{1}{2})^3 + \dots \quad (2.30)$$

$$F_v(J) = B_v J(J+1) - D_v [J(J+1)]^2 + H_v [J(J+1)]^3 + \dots, \quad (2.31)$$

$$B_v = B_e - \alpha_e(v + \frac{1}{2}) + \dots, \quad B_e = \frac{\hbar}{4c\mu R_e^2} \quad (2.32)$$

$$D_v = D_e - \beta_e(v + \frac{1}{2}) + \dots, \quad D_e = \frac{4B_e^3}{\omega_e^2} \quad (2.33)$$

$$H_v = H_e + \dots, \quad H_e = \frac{2D_e}{3\omega_e^2(12B_e^2 - \alpha_e\omega_e)}. \quad (2.34)$$

### 2.4.2 Dunham expansion

An alternative, but more general, form than the molecular constants for representation of level energies of a diatomic molecule was derived by Dunham [41]. In this method the effective potential in (2.19) is expanded in terms of power series

$$U_{eff}(\xi) = T_e + a_0 \xi^2 (1 + a_1 \xi + a_2 \xi^2 + \dots) + \\ + B_e [J(J+1) - \Lambda^2] (1 - 2\xi + 3\xi^2 - 4\xi^3 + \dots), \quad (2.35)$$

with

$$\xi = \frac{R - R_e}{R_e}, \quad (2.36)$$

and  $a_i$  ( $i = 0, 1, 2, \dots$ ) are constants determined with derivatives of the Dunham potential. The first term in (2.35) is electronic energy, the second grouped-term represents vibrational potential of the nuclei, and the last grouped-term stands for the rotational energy of the molecule.

Although the exact solution of the RSE is not possible to derive with the Dunham potential but one can find it within the semiclassical approximation. Indeed, using the first-order semiclassical quantization condition (Wentzel-Kramers-Brillouin (WKB) theory [42]) Dunham solved the RSE with the potential (2.35) yielding expression for the spectroscopic term as follows:

$$T(v, J) = T_e + \sum_i \sum_k Y_{ik} (v + \frac{1}{2})^i [J(J+1) - \Lambda^2]^k. \quad (2.37)$$

In (2.37),  $Y_{jk}$  ( $i = 0, 1, 2, \dots$ ;  $k = 0, 1, 2, \dots$ ) are Dunham coefficients which are related to the expansion coefficients  $\{a_i\}$  in (2.35). The relations between the  $Y_{ik}$  and  $a_i$  coefficients can be found in [41]. On the other hand, by comparing (2.37) with (2.29) we obtain the following relations between the Dunham coefficients and molecular constants:

$$\begin{aligned} Y_{10} &= \omega_e, & Y_{20} &= -\omega_e x_e, & Y_{30} &= \omega_e y_e \\ Y_{01} &= B_e, & Y_{11} &= -\alpha_e, & Y_{21} &= \gamma_e \\ Y_{02} &= -D_e, & Y_{12} &= -\beta_e, & Y_{03} &= H_e. \end{aligned} \quad (2.38)$$

Actually it was pointed out by Dunham that there are some small deviations between Dunham coefficients and molecular constants in relations (2.38). These deviations are of the order of  $B_e^2 / \omega_e^2 \sim 10^{-6}$ ; therefore they are negligible. There is also a small non-zero term  $Y_{00}$ :

$$Y_{00} = \frac{B_e}{4} + \frac{\alpha_e \omega_e}{12B_e} + \frac{\alpha_e^2 \omega_e^2}{144B_e^4} - \frac{\omega_e x_e}{4}. \quad (2.39)$$

Small value of  $Y_{00}$  is because the first three terms in (2.39) are almost cancelled by the last one, and in most cases  $Y_{00}$  is incorporated into the electronic energy  $T_e$ .

Since the molecular constants are nuclear mass-dependent the values of the Dunham coefficients are therefore altered from one isotopomer to the other. Within the BO approximation the vibrational potential energy curves of different isotopomers are identical. Therefore for an isotope with a reduced-mass  $\mu^\alpha$ , the Dunham expansion should be modified to [34]:

$$T^{(\alpha)}(v, J) = T_e + \sum_i \sum_k Y_{ik} [\rho(v + \frac{1}{2})]^i [\rho^2 [J(J+1) - \Lambda^2]]^k, \quad (2.40)$$

where

$$\rho = \sqrt{\frac{\mu}{\mu^\alpha}}. \quad (2.41)$$

The Dunham expansion is widely used to represent level energies of diatomic molecules because such representation is quite simple and is able to represent the high order effects such as unharmonicities of the potential, centrifugal forces, as well as

couplings between vibrational and rotational motions. However some drawbacks may be encountered in application of the Dunham method. Indeed, as pointed out by Beckel [43], the Dunham potential is convergent in the region for which  $R < 2R_e$ . For low vibrational levels the inner and outer turning points of the potential are around the equilibrium internuclear distance, thus the Dunham expansion represents fairly well experimental data. When experimental data lie closely the dissociation limit, the outer turning points of highly vibrational levels exceed  $2R_e$ , the power series is thus gradually diverged. In this case more coefficients, some of them of no physical meaning, are needed to describe the overall experimental data.

### 2.4.3 Morse and Hulbert-Hirschfelder potentials

One of the important models of the analytical potential was proposed by Morse [44] in the following form

$$U^{Morse}(R) = T_e + D^e \left[ 1 - e^{-\beta(R-R_e)/R_e} \right]^2. \quad (2.42)$$

Where:  $T_e$ ,  $D^e$ , and  $R_e$  stand for the electronic energy, dissociation energy, and the internuclear equilibrium distance, respectively;  $\beta$  is a parameter. If one disregards the rotation of molecule, the RSE with this potential can be solved analytically yielding the vibrational energy. Comparing this analytical result to expression (2.30), we obtain correspondence of  $\beta$  and  $D^e$  with the molecular constants:

$$\beta = \sqrt{\frac{\pi c \mu}{\hbar D^e}} \omega_e, \quad D^e = \frac{\omega_e^2}{4\omega_e x_e}. \quad (2.43)$$

Additionally taking into account the rotational motion of molecule Pekeris [47] solved the RSE with Morse potential by using perturbation techniques. He obtained an expression for rotational energy of the form (2.31) and among some molecular constants:

$$\alpha_e = B_e x_e \left[ 3(B_e / \omega_e x_e)^{\frac{1}{2}} - 3(B_e / \omega_e x_e) \right], \quad D_e = \frac{4B_e^3}{\omega_e^2}. \quad (2.44)$$

The first expression of (2.44) gives quantitative relation between the rotational and vibrational motions of the molecule; the second expression represents a relation among the

centrifugal, rotational and vibrational constants. By replacing these molecular constants with the corresponding Dunham coefficients we obtain the so called Kratzer relation [47]:

$$Y_{02} = -4 \frac{(Y_{01})^3}{(Y_{10})^2}. \quad (2.45)$$

The Morse potential is an attractive model because of its simple analytical form. It is often used as a criterion to estimate a regularity of a PEC by considering the consistency among the molecular constants in (2.44) or (2.45). However, since the Morse potential is determined by only three parameters it is only rough approximation, not flexible enough to interpret entire experimentally obtained data. Following the works by Dunham [41] and Coolidge et al [45], Hulbert and Hirschfelder developed more sophisticated five-parameter potential [46] in the following form:

$$U^{HH}(R) = T_e + D^e \left[ (1 - e^{-x})^2 + cx^3 e^{-2x} (1 + bx) \right], \quad (2.46)$$

where,

$$x = \frac{\omega_e}{2(B_e D^e)^{\frac{1}{2}}} \left[ \frac{R - R_e}{R_e} \right] \quad (2.47)$$

$$c = 1 - \frac{1}{\beta R_e} \left( 1 + \frac{\omega_e \alpha_e}{6B_e^2} \right) \quad (2.48)$$

$$b = 2 - \frac{1}{c} \left[ \frac{7}{12} - \frac{1}{\beta^2 R_e^2} \left( \frac{5}{4} + \frac{5\omega_e \alpha_e}{12B_e^2} + \frac{5\omega_e^2 \alpha_e^2}{144B_e^4} - \frac{2\omega_e x_e}{3B_e} \right) \right]. \quad (2.49)$$

With five parameters the  $U^{HH}(R)$  potential is more flexible than the Morse function, however also not adequate to describe highly precise data from nowadays experiments.

#### 2.4.4 RKR potential

Another approach to the problem of searching a potential curve for representing experimentally measured level energies is to construct the PEC from experimental data. One of the widely used methods to construct potential energy curve was proposed by Rydberg, Klein, and Rees [35]. They used the first-order WKB approximation to calculate turning points for each vibrational energy level. The basic idea of the calculation is to start from the following quantization condition

$$(v + \frac{1}{2})\pi = \left( \frac{\sqrt{2\mu}}{\hbar} \right) \int_{R_1(v)}^{R_2(v)} [E_{v,J} - U_J(R)]^{1/2} dR. \quad (2.50)$$

In (2.50),  $U_J(R)$  is the effective potential;  $R_1(v)$  and  $R_2(v)$  are inner and outer turning points, respectively. The turning points are determined from:

$$E_{v,J} = U_J(R_1(v)) = U_J(R_2(v)).$$

Next, the vibrational quantum number  $v$  is treated as a continuous function of energy. The equation (2.50) can therefore be partially differentiated with respect to  $E$  and to  $J$  ( $J+1$ ). Finally one obtains two coupled equations for turning points:

$$R_1(v) - R_2(v) = 2\sqrt{\frac{\hbar^2}{2\mu}} \int_{v_0}^v \frac{dv'}{[G(v) - G(v')]^{1/2}}, \quad (2.51a)$$

$$\frac{1}{R_1(v)} - \frac{1}{R_2(v)} = 2\sqrt{\frac{2\mu}{\hbar^2}} \int_{v_0}^v \frac{B_{v'}}{[G(v) - G(v')]^{1/2}} dv'. \quad (2.51b)$$

Here,  $v_0$  is an extrapolated value of the vibrational quantum number to the potential minimum, it is given by:

$$v_0 = -\frac{1}{2} - \frac{Y_{00}}{\omega_e}. \quad (2.52)$$

In practice, the functions  $B_v$  and  $G(v)$  can be determined from experimental data therefore the RKR potential curve determined with pairs of turning points can be readily numerically calculated.

#### 2.4.5 Long-range behaviour of potential energy curves

Since depending on internuclear distance different forces (exchange or dispersion forces) dominate, it is convenient to divide the potential into the short-range and long-range parts in order to describe the PEC of a molecule. The short-range part involves chemical bonding which depends strongly on the overlap of electronic clouds between the two atoms and is governed by exchange forces. The long-range part involves the dispersion forces which are resulting from electrostatic, induction, and resonance forces. It is usual to represent the long-range part of a potential by the following form:

$$U(R) = D^e - \sum_n \frac{C_n}{R^n}. \quad (2.53)$$

From (2.53) one can see that the potential approaches the dissociation energy when the two atoms are separated infinitively. The dispersion coefficients  $C_n$  are determined according to the atomic electronic states at which the given molecule dissociates. From basic quantum - mechanical considerations one can see that dominant terms in the expansion (2.53) depend on symmetry of asymptotic atomic states. Namely [48]:

- For homonuclear diatomic molecules:

For  $nS - n'S$  asymptote, dominant terms in (2.53) are with  $n = 6, 8, 10 \dots$

$nS - n'P$  asymptote:  $n = 3, 6, 8, 10 \dots$

$nS - n'D$  asymptote:  $n = 5, 6, 8, 10 \dots$

$nP - n'P$  asymptote:  $n = 5, 6, 8, 10 \dots$

- For heteronuclear diatomic molecules:

$nS - n'S$  asymptote:  $n = 6, 8, 10 \dots$

$nS - n'P$  asymptote:  $n = 6, 8, 10 \dots$

$nS - n'D$  asymptote:  $n = 6, 8, 10 \dots$

$nP - n'P$  asymptote:  $n = 5, 6, 8, 10 \dots$

For alkali diatomic molecules, Marinescu et al [49-52] calculated coefficients  $C_n$  in framework of the second-order perturbation theory.

We determine the pure long-range region as a range for which the exchange interactions are weaker compared to the dispersion forces. LeRoy [48] proposed a quantitative criterion for determining the value of internuclear distance from which the expansion (2.53) is valid. Following his work the long-range expansion (2.53) is valid for atomic separation larger than the so called LeRoy radius  $R_{LR}$ , given by

$$R_{LR} = 2 \left[ \langle r^2 \rangle_A^{\frac{1}{2}} + \langle r^2 \rangle_B^{\frac{1}{2}} \right]. \quad (2.54)$$

Here  $\langle r^2 \rangle^{\frac{1}{2}}$  is the root mean square of radius of the outermost electron of the atom. Since for non-spherical atomic orbitals the spatial distribution of the charge-cloud of the outermost electron depends on spatial orientation of the overlap between outermost

electrons, thus depends on the projection of angular momentum  $\vec{l}$  along the internuclear axis. Therefore Bing Ji *et al* [53] proposed to use a modified LeRoy radius determined by:

$$R_{LR-m} = 2\sqrt{3} \left[ \langle nlm | z^2 | nlm \rangle_A^{\frac{1}{2}} + \langle n'l'm' | z^2 | n'l'm' \rangle_B^{\frac{1}{2}} \right]. \quad (2.55)$$

Here  $n$  is the principal quantum number, and  $l$  is quantum number of angular momentum of the outermost electron,  $z$  is the projection of position vector  $\vec{r}$  of the outermost electron on the internuclear axis, and  $m$  is the quantum number of the projection of  $\vec{l}$  along the internuclear axis. For alkali atoms, using hydrogen like wavefunctions the modified LeRoy radius can be determined by

$$R_{LR-m} = 2\sqrt{3} \left[ G_{l,m} \langle r^2 \rangle_{n*,l; A}^{\frac{1}{2}} + G_{l',m'} \langle r^2 \rangle_{n*,l'; B}^{\frac{1}{2}} \right], \quad (2.56)$$

where

$$G_{l,m} = \left( \frac{1}{3} - \frac{2}{3} \frac{3m^2 - l(l+1)}{(2l+3)(2l-1)} \right)^{\frac{1}{2}}, \quad (2.57)$$

$$\langle r^2 \rangle_{n*,l; N} = \frac{a_o^2 M_N^2 n_*^4}{\mu_N^2 Z_N^2} \left[ 1 + \frac{3}{2} \left( 1 - \frac{l(l+1) - 1/3}{n_*^2} \right) \right]. \quad (2.58)$$

In expression (2.58),  $a_o$  is the Bohr radius,  $M_N$  ( $N = A, B$ ) the mass of nucleus,  $Z$  is the nuclear charge,  $\mu_N$  is the reduced mass of the atom, and  $n_*$  is the effective principal quantum number of the outermost electron of the atom.

#### 2.4.6 Inverse perturbation approach and direct potential fit

The construction of a potential which is capable to reproduce experimental level energies with a desired accuracy plays a crucial role in present spectroscopic investigations. In the literature two quantum mechanical techniques were proposed to attain this goal. The first one is the inverse perturbation approach (IPA) which was proposed in 1975 [54-55]. This technique was originally applied to construct numerical potentials. The second one is the direct potential fit (DPotFit) which was proposed by LeRoy in 1974 for atom-diatom systems [56] and later applied for diatomic molecules [58]. The DPotFit technique involves analytical potentials containing adjustable parameters. Both IPA and DPotFit techniques have the same essential algorithm that is

outlined fig.2.3. The algorithm starts with an initial approximate trial potential. In the next step the RSE is solved with the trial potential and then the calculated eigenvalues are compared with the corresponding experimental level energies. If deviations are beyond a criterion (experimental uncertainty, for example), the trial potential is modified so that to minimize the deviations. The minimization of these deviations is performed by using least-squares fit methods. The corrected potential is then used as the trial one and the procedure is repeated until convergence.

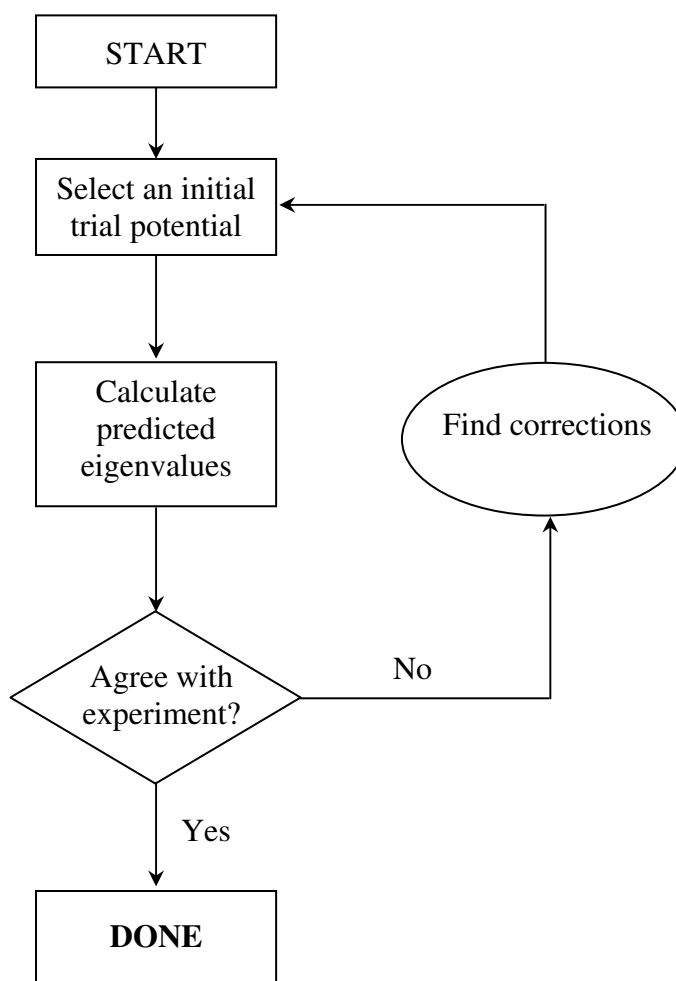


**Figure 2.3.** Schematic outline of the algorithm for the IPA and DPotFit techniques.

In the original IPA technique [54-55] the potential correction is expanded over the basis set of Legendre polynomials with adjustable coefficients. These coefficients are then determined by using linear least-squares fit method. In practice the method depends strongly on the choice of the number of basis functions in the calculations. Furthermore

shape of the potential may be quite irregular and it is difficult to guess an optimal number of basis functions to be used. An improvement overcoming this drawback was proposed by Pashov *et al.*, [57]. Instead of employing the basis functions the authors introduced a cubic-spline function to connect points of the numerical potential.

In DPotFit technique an analytical model potential including a set of adjustable parameters is used as the trial one. Since the trial potential is expressed in analytical form so the Hellmann-Feynman theorem is used to relate eigenvalues of the RSE to the parameters of the given potential. Such relations serve for the minimization of deviations between the experimental and calculated level energies, to find optimal values for the parameters of the trial potential function.

## 2.5. Selection rules for optical transitions

### 2.5.1 Total parity and general selection rules

Let us consider a symmetry operator  $\hat{\mathbf{I}}$  that inverts all the coordinates of particles (nuclei and electrons) in the laboratory frame with origin at the centre of masses. Upon such operation the total wavefunction is given by

$$\hat{\mathbf{I}}\Psi(X_i, Y_i, Z_i) = \Psi(-X_i, -Y_i, -Z_i) = \pm\Psi(X_i, Y_i, Z_i). \quad (2.59)$$

Using (2.59) and the BO approximation we obtain:

$$\hat{\mathbf{I}}\Psi = \hat{\mathbf{I}}[\Psi^{el} \xi^{vib} u^{rot}] = \pm\Psi. \quad (2.60)$$

Since the vibrational functions  $\xi^{vib}$  depend only on internuclear separation, they are unchanged by the inversion operator  $\hat{\mathbf{I}}$ . However, the effects of  $\hat{\mathbf{I}}$  on electronic and rotational wavefunctions are quite complicated because we only know the functions in the molecular fixed frame but not in the laboratory frame. Following the group theory the parity of a rotation level is given by [59]:

$$\hat{\mathbf{I}}u_{\Omega, J, M}^{rot} = (-1)^{J-\Omega} u_{-\Omega, J, M}^{rot}. \quad (2.61)$$

It was Hougen who pointed out that the action of  $\hat{\mathbf{I}}$  on the wavefunction in the laboratory frame is equivalent to the symmetry operation of the reflection operator  $\hat{\sigma}_v$  (see [86], for example) in the molecular frame.

The total parity under reflection of  $\hat{\sigma}_v$  is given by:

$$\begin{aligned}\hat{\sigma}_v[\Psi_{n,\Lambda,S,\Sigma}^{el} \xi_v^{vib} u_{\Omega,J,M}^{rot}] &= \hat{\sigma}_v[|n, \Lambda, S, \Sigma\rangle |v\rangle |\Omega, J, M\rangle] \\ &= (-1)^{J-2\Sigma+S+\sigma} |n, -\Lambda, S, -\Sigma\rangle |v\rangle |-\Omega, J, M\rangle,\end{aligned}\quad (2.62)$$

where,  $\sigma = 0$  for all states except  $\Sigma^-$  for which  $\sigma = 1$ .

The selection rules for electric dipole transitions can be derived by requiring a totally symmetric integrand in the following integral:

$$\mu_{ik} = \int \psi_i^* \vec{\mu} \Psi_k d\tau. \quad (2.63)$$

Because the electric dipole moment  $\vec{\mu}$  has negative (-) parity, therefore only the levels of opposite parities can be coupled by one photon electric dipole transitions. Namely,

$$+ \leftrightarrow -, + \leftrightarrow +, - \leftrightarrow -. \quad (2.64)$$

Since the total parity changes sign with  $J$  because of the factor  $(-1)^J$  in (2.62) so it is convenient to introduce  $e$  and  $f$  parity (or rotationless parity [86]) given by:

$$\hat{\mathbf{I}} \Psi = (-1)^J \Psi \text{ for } e, \quad (2.65a)$$

$$\hat{\mathbf{I}} \Psi = -(-1)^J \Psi \text{ for } f. \quad (2.65b)$$

From (2.65) and (2.62) one can see that all rotational levels in  $^1\Sigma^+$  states are of  $e$  parity, while levels in  $^1\Sigma^-$  states are of  $f$  parity. For singlet states having  $\Lambda > 0$  (i.e.,  $^1\Pi$ ,  $^1\Delta$  ...) each rotational level is composed of two components, one corresponds to  $e$ -parity and the other corresponds to  $f$ -parity. Figure 2.4 illustrates parity of the rotational levels in  $\Sigma^+$ ,  $\Sigma^-$ , and  $^1\Pi$  states.

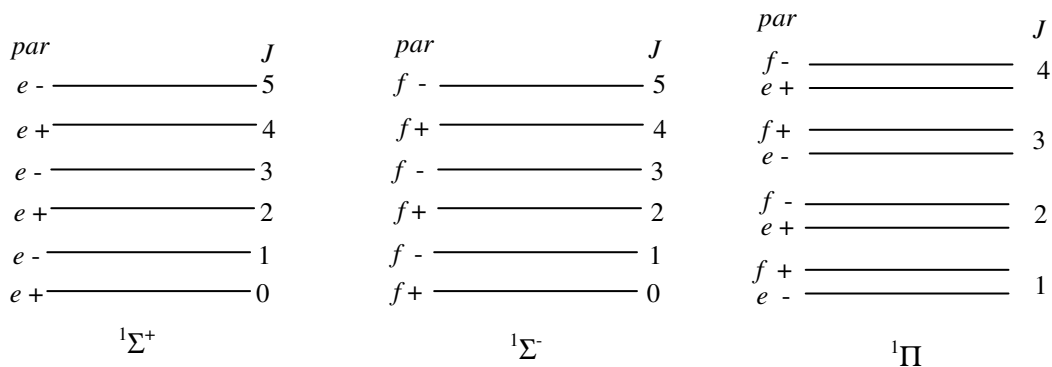


**Figure 2.4.** Illustration of parity of the rotational levels in the  ${}^1\Sigma^+$ ,  ${}^1\Sigma^-$ , and  ${}^1\Pi$  states.

### 2.5.2 Selection rules

In addition to the selection rules for the total parity, spectra of diatomic molecules are also governed by other rules. In this section we restrict our considerations to one-photon electric dipole transitions for electronic and rotational transitions. The rules are derived by requiring the non-vanishing transition matrix element in (2.63). It is convenient to separate the dipole moment ( $\vec{\mu}$ ) into two parts: electronic ( $\vec{\mu}_{el}$ ) and nuclear ( $\vec{\mu}_n$ ). Such separation eliminates contribution of the nuclear moment in (2.63) due to the orthogonality of electronic wavefunctions and therefore, one can consider only the electronic dipole moment. Following [34, 59], selection rules for electronic and rotational transitions are given by:

- **Electronic transitions**

$$\Delta\Lambda = 0, \pm 1 \quad (2.66)$$

$$\Delta S = 0 \quad (2.67)$$

$$\Delta\Sigma = 0. \quad (2.68)$$

$$\Sigma^+ \leftrightarrow \Sigma^+, \Sigma^- \leftrightarrow \Sigma^-, \Sigma^+ \leftrightarrow \Sigma^-. \quad (2.69)$$

$$g \leftrightarrow u, g \leftrightarrow g, u \leftrightarrow u. \quad (2.70)$$

- **Rotational transitions**

For  $\Delta\Lambda = \pm 1$ :

$$\Delta J = 0, \pm 1, J = 0 \leftrightarrow J = 0 \quad (2.71)$$

For  $\Delta\Lambda = 0$ :

$$\Delta J = \pm 1. \quad (2.72)$$

For  $e/f$  parity:

$$e \leftrightarrow f \quad \text{for } \Delta J = 0 \quad , \quad (2.73)$$

$$e \leftrightarrow e, f \leftrightarrow f \quad \text{for } \Delta J = \pm 1. \quad (2.74)$$

### 2.5.3 Franck-Condon principle

Spectra of diatomic molecules are not only governed by the above selection rules but also governed by the so called Franck-Condon principle, which states that an optical transition between two electronic states occurs so quickly that neither the positions nor the velocities of the nuclei change significantly during the transition. Therefore, in the potential energy diagram (fig.2.5) the electronic transition occurs vertically.

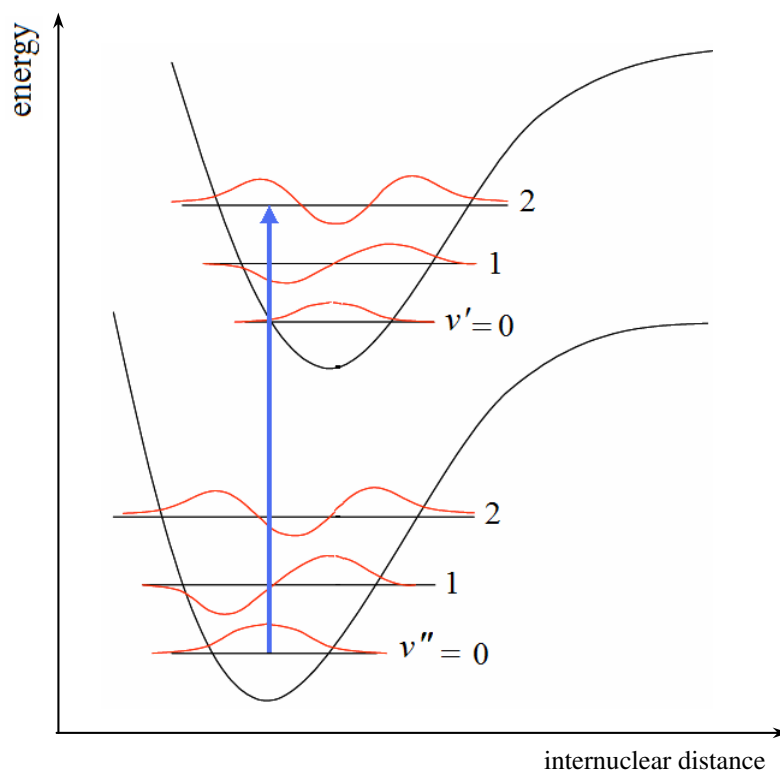


**Figure 2.5.** Potential energy diagram with vertical transitions (Franck-Condon principle), the red curves stand for vibrational wavefunctions.

Within the BO approximation, following the Franck-Condon principle, one can derive that the probability  $P_{v''v'}$  of a vibrational transition between two electronic states is proportional to the so called Franck-Condon factor (FCF) determined by:

$$P_{v''v'} \sim |FCF|_{v''v'}^2 \equiv \left| \int \xi_{v'}^{vib}(R) \xi_{v''}^{vib}(R) dR \right|^2. \quad (2.75)$$

Here  $\xi_{v'}^{vib}(R)$  and  $\xi_{v''}^{vib}(R)$  are vibrational wavefunction for level  $v'$  and  $v''$ , respectively. Since the integral (2.75) depends on vibrational wavefunctions and sensitively depends on vibrational quantum numbers ( $v'$ ,  $v''$ ) as a consequence changes of the transition intensity within the progressions starting from individual  $v''$  is observed. As an example in fig.2.5, is shown situation where intensity of the transition  $v' = 0 - v'' = 0$  is much weaker than that of the  $0 - 2$  due to different overlap between corresponding wavefunctions.

## 2.6. Perturbations in molecular spectra

In principle within the BO approximation it should be possible to deduce position of all observed spectral lines from potential energy curves. Nevertheless it turns out that it is not always the case - namely wavelengths of some spectral lines deviate more or less pronouncedly from that calculated from the potentials. We call these shifted spectral lines (or levels involved in certain transition) as perturbed. The perturbations in molecular spectra involve the terms neglected in the total Hamiltonian in the BO approximation. From the point of view of the perturbation theory one can consider the BO approximation as the zero-order approximation and take into account the neglected BO terms as higher order corrections. In general we can represent the total Hamiltonian  $\hat{H}$  by:

$$\hat{H} = \hat{H}^{el} + \hat{T}^N + \hat{H}^s. \quad (2.76)$$

In (2.76),  $\hat{H}^{el}$  stands for the electronic Hamiltonian including nuclear repulsion,  $\hat{T}^N$  stands for the nuclear kinetic operator, and  $\hat{H}^s$  stands for the operator for the spin interactions. The total energy of the molecule is calculated via the matrix elements of the above operators in the basis of BO wavefunctions. In particular, the diagonal elements of (2.76) give the energy of the molecule which we considered in the previous sections, while off-diagonal elements of (2.76) give rise to perturbations.

### 2.6.1 Electrostatic and non-adiabatic perturbations

The electrostatic and non-adiabatic perturbations arise from off-diagonal elements of  $\hat{H}^{el}$  and  $\hat{T}^N$  operators, respectively [60-63]. From the point of view of the perturbation

theory it is important to choose a basic functions in a way that the off-diagonal matrix elements,

$$\langle \Psi_i | \hat{\mathbf{H}}^{\text{el}} + \hat{\mathbf{T}}^N | \Psi_k \rangle = \langle \Psi_i | \hat{\mathbf{H}}^{\text{el}} | \Psi_k \rangle + \langle \Psi_i | \hat{\mathbf{T}}^N | \Psi_k \rangle \quad (2.77)$$

are small. Because  $\hat{\mathbf{H}}^{\text{el}}$  and  $\hat{\mathbf{T}}^N$  operators do not commute there is no way to find a basis of functions in which both two terms in (2.77) simultaneously vanish. In practice, two equivalent ways for choosing the basic functions are used to get each term in (2.77) alternatively vanished. The first, in which the off-diagonal elements of  $\hat{\mathbf{T}}^N$  vanish, is called the *diabatic* representation. In this representation the no-vanishing off-diagonal elements of  $\hat{\mathbf{H}}^{\text{el}}$  give rise to electrostatic perturbations. The second one is *adiabatic* representation where the off-diagonal elements of  $\hat{\mathbf{H}}^{\text{el}}$  vanish. In the adiabatic approximation, off-diagonal elements of  $\hat{\mathbf{T}}^N$  give rise to non-adiabatic couplings.

According to Neumann and Wigner any two potential curves of electronic states of identical symmetry do not cross each other. If in a certain approximation the potential curves cross each other then higher order corrections (electrostatic or non-adiabatic couplings) has to be taken into account. The resultant potential curves obtained in these cases usually have irregular shapes because of the avoided crossing.

In diabatic representation the electrostatic perturbations are represented by the following matrix elements:

$$H_{k,v_k;l,v_l} = \langle \Phi_k^d \chi_{v_k}^d | \hat{\mathbf{H}}^{\text{el}} | \Phi_l^d \chi_{v_l}^d \rangle \approx H^e \langle v_k | v_l \rangle, \quad (2.78)$$

where

$$H^e = \langle \Phi_k^d | \hat{\mathbf{H}}^{\text{el}} | \Phi_l^d \rangle, \text{ and } \langle v_k^d | v_l^d \rangle = \int \chi_{v_k}^d(R) \chi_{v_l}^d dR. \quad (2.79)$$

For most cases,  $H^e$  depends weakly on internuclear separation  $R$ . Therefore, using the  $R$ -centroid approximation [61] the off-diagonal matrix elements can be estimated theoretically.

In adiabatic representation the perturbations are due to the matrix elements of the kinetic energy operator of the two nuclei. The diagonal matrix element of this operator is called adiabatic correction, and the off-diagonal matrix elements are called non-adiabatic couplings. In most cases the magnitude of adiabatic correction is much larger than those of

non-adiabatic couplings. Including the adiabatic correction into the BO potential one obtains the so called adiabatic potential:

$$U_k^{ad}(R) = U_k^{BO}(R) + T_{kk}^N. \quad (2.80)$$

In higher approximations the potential energy of the molecule is calculated by adding adiabatic potential  $U_k^{ad}(R)$  to the non-adiabatic coupling terms  $T_{kl}^N$ , where

$$T_{kl}^N = T_{k,v_k;l,v_l}^N = \langle \Phi_k^{ad} \chi_{v_k}^{ad} | \hat{\mathbf{T}}^N | \Phi_l^{ad} \chi_{v_l}^{ad} \rangle. \quad (2.81)$$

Therefore it is necessary to know adiabatic wavefunctions in order to estimate non-adiabatic coupling.

### 2.6.2 Spin-Orbit coupling

In (2.76) the operator  $\hat{\mathbf{H}}^s$  can be represented as a sum of the spin-orbit ( $\hat{\mathbf{H}}^{s-1}$ ) and the spin-spin ( $\hat{\mathbf{H}}^{s-s}$ ) interactions. These interactions are responsible for spin perturbations and usually the spin-orbit interactions are much stronger than that of the spin-spin interactions. The spin-orbit interactions appear due to coupling among spins of electrons and the angular momenta caused by moving electrons and the rotating molecule. Let's consider a case where the couplings between the different angular momenta  $\vec{l}_i$  of the electrons and between their spins  $\vec{s}_i$  are stronger than the interaction between  $\vec{l}_i$  and  $\vec{s}_i$  (Hund's case (a)). In this case the  $\hat{\mathbf{H}}^{s-1}$  is approximated by [60-61]:

$$\hat{\mathbf{H}}^{s-1} = A \vec{L} \vec{S} \quad \text{with} \quad \vec{L} = \sum \vec{l}_i \quad \text{and} \quad \vec{S} = \sum \vec{s}_i, \quad (2.82)$$

where  $A$  is the spin-orbit coupling constant. It is then convenient to calculate  $\hat{\mathbf{H}}^{s-1}$  in the BO basis functions  $|\Lambda, \Sigma, S, \Omega, \nu\rangle$  of Hund's case (a). The matrix elements of  $\hat{\mathbf{H}}^{s-1}$  give the energies of the fine-structure components. In the next step the higher-order couplings ( $\vec{s}_i \vec{l}_k$  and  $\vec{s}_i \vec{s}_k$ ) are introduced. The selection rules for non-vanishing matrix elements

$$\langle \Lambda_i, \Sigma_i, S_i, \Omega_i, \nu_i | \hat{\mathbf{H}}^{s-1} | \Lambda_k, \Sigma_k, S_k, \Omega_k, \nu_k \rangle \quad (2.83)$$

of the spin-orbit coupling are following [60-61]:

$$\Delta J = 0; \Delta S = 0, \pm 1; \Delta \Omega = 0. \quad (2.84)$$

Generally only rotational levels with the same total angular momentum quantum number  $J$  can interact through spin-orbit interactions. From the rules in (2.84) we see that, if the two interacting states belong to the same electron configuration then  $\Delta \Lambda = \Delta \Sigma = 0$  holds. If the two states differ by one spin orbital then  $\Delta \Lambda = -\Delta \Sigma = \pm 1$ .

### 2.6.3 Rotational perturbations

The rotational perturbations arise from off-diagonal matrix elements of the rotational kinetic energy operator. These matrix elements are determined by terms neglected in BO approximation. In detail, the neglected terms are given by [61]:

$$\frac{1}{2\mu R^2}(\hat{\mathbf{L}}^+ \hat{\mathbf{S}}^- + \hat{\mathbf{L}}^- \hat{\mathbf{S}}^+) \quad (2.85)$$

$$-\frac{1}{2\mu R^2}(\hat{\mathbf{J}}^+ \hat{\mathbf{S}}^- + \hat{\mathbf{J}}^- \hat{\mathbf{S}}^+) \quad (2.86)$$

$$-\frac{1}{2\mu R^2}(\hat{\mathbf{J}}^+ \hat{\mathbf{L}}^- + \hat{\mathbf{J}}^- \hat{\mathbf{L}}^+), \quad (2.87)$$

where  $\hat{\mathbf{X}}^+$  and  $\hat{\mathbf{X}}^-$  ( $\hat{\mathbf{X}}$  stands for  $\hat{\mathbf{J}}$ ,  $\hat{\mathbf{L}}$ ,  $\hat{\mathbf{S}}$  operators) are lowering and rising operators, respectively. These terms are responsible for the following perturbations:

- ***Homogeneous spin-electronic perturbation***

The homogeneous spin-electronic perturbation arises from the off-diagonal matrix elements of (2.85). These couplings are non-zero between states having the same  $\Omega$  and  $S$ , but different  $\Lambda$  and  $\Sigma$ . The selection rules for the spin-electronic perturbations are given by [61]:

$$\Delta \Omega = 0, \Delta S = 0, \Delta \Lambda = -\Delta \Sigma = \pm 1. \quad (2.85a)$$

Therefore, the spin-electronic perturbation gives rise to local perturbations between electronic states of different symmetry.

- ***Heterogeneous electronic-rotation perturbations***

The heterogeneous electronic-rotation perturbations arise from the operator (2.86) which is called  $\vec{S}$ -uncoupling operator. This operator couples states having different  $\Omega$  and  $\Sigma$ , but

having the same  $\Lambda$  and  $S$ . The heterogeneous electronic-rotation perturbations obey the following selection rules [61]:

$$\Delta\Omega = \Delta\Sigma = \pm 1, \Delta S = \Delta\Lambda = 0. \quad (2.86a)$$

In the heterogeneous electronic-rotation perturbations, the  $\vec{S}$ -uncoupling operator mixes different components of the same electronic state, often between the substates of different vibrational levels. Therefore, it gives rise to local perturbations. When rotation increases, the  $\vec{S}$ -uncoupling operator tends to make transition from Hund's case (a) to case (b).

- ***Heterogeneous electronic-rotation perturbations***

The term given by (2.87) is called  $\vec{L}$ -uncoupling operator. It is responsible for heterogeneous electronic-rotation perturbations between states having different  $\Omega$ - and  $\Lambda$ -values but having the same  $\Sigma$  and  $S$ . The selection rules for this type of perturbations are determined by [61]:

$$\Delta\Omega = \Delta\Lambda = \pm 1, \Delta S = \Delta\Sigma = 0. \quad (2.87a)$$

As the rotation of the molecule increases, the  $\vec{L}$ -uncoupling operator tends to make transition from Hund's case (a) to case (d), which is called the uncoupling phenomenon. Upon such interactions the degenerated energy levels in states having  $\Lambda > 0$  are gradually split.

For  ${}^1\Pi$  symmetry states, under such interactions the two-fold degenerate levels are split - this is so called lambda-doubling. According to the selection rules (2.87a) levels in  ${}^1\Pi$  state couple with levels in states of  ${}^1\Sigma^+$ ,  ${}^1\Sigma^-$ , and  ${}^1\Delta$  symmetry. For a given  $J$ , there are two  $e$ - and  $f$ -components. If these degenerated levels are coupled by levels in a  ${}^1\Sigma^+$  electronic state, only  $e$ - parity components in  ${}^1\Pi$  state are affected. Alternatively if the degenerated levels are coupled with levels in a  ${}^1\Sigma^-$  state, only  $f$ -parity components in  ${}^1\Pi$  state are affected. In general, the amplitude of the lambda-doubling splitting depends on strength of coupling between vibrational and rotational motions. For convenience, such splitting is often given in terms of double power expansion of vibrational and rotational quantum numbers. Namely,

$$\Delta T(v, J) = \sum_{k,l} q_{kl} (v + \frac{1}{2})^k [J(J+1)]^l, \quad (2.88)$$

where  $q_{kl}$  represent the lambda-doubling coefficients. The representation of the lambda-doubling splitting in form (2.88) is convenient for cases where spectroscopic term values are determined by Dunham expansion (2.37) or for construction of potential curve in numerical form. An alternative form for representing the lambda-doubling splitting is a function of internuclear distance [58]:

$$\Delta T(v, J) = \Delta T(R) = \left( \frac{\hbar^2}{2\mu R^2} \right)^2 f_{\Lambda}(R) \quad (2.89)$$

where  $f_{\Lambda}(R)$  is a so called lambda-doubling strength function. This representation of lambda-doubling splitting is convenient for construction of potential curve in analytical form.

## Chapter 3

### Polarization labelling spectroscopy and experimental arrangement

#### 3.1. Polarization labelling spectroscopy

##### 3.1.1 Basic principles

The polarization labelling spectroscopy (PLS) method was proposed in 1976 [27]. It combines polarization spectroscopy and optical-optical double resonance techniques [64-66]. The basic idea of the method is to monitor changes of polarization of a weak probe laser beam after passing through a molecular sample optically pumped by a strong laser light coming from another laser. A typical experimental scheme of PLS experiment is shown in figure 3.1, where the molecular sample is placed between two crossed linear polarizers  $P_1$  and  $P_2$ .

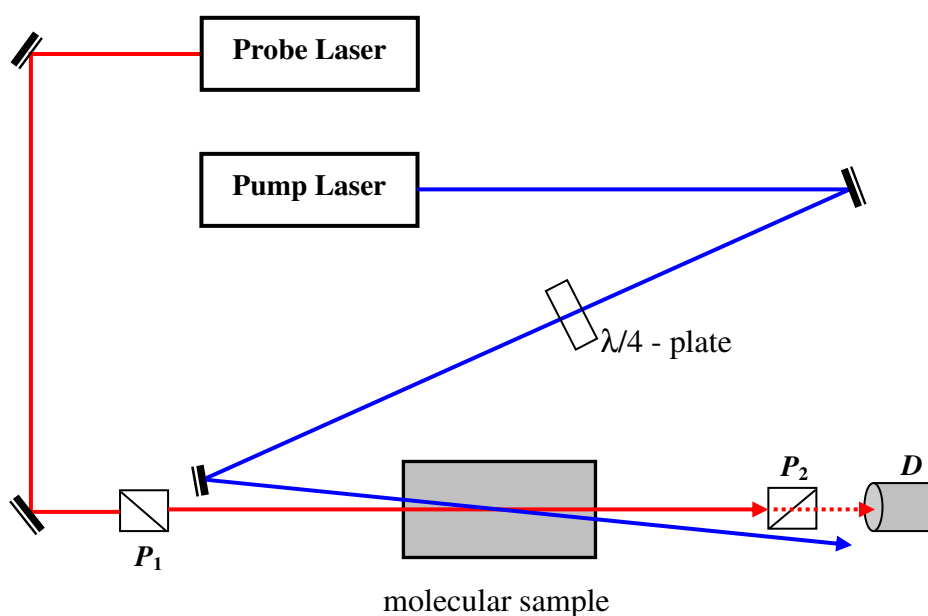


**Figure 3.1.** Scheme of the PLS method:  $P_1$  and  $P_2$  are the pair of crossed linear polarizers,  $D$  is detector to monitor signal of the probe beam.

When the pump laser is off, the molecular sample is optically isotropic because there is no preferential direction for total angular momentum  $\vec{J}$  of each molecule. Namely for a given value of quantum number  $J$  there are  $2J + 1$  degenerated Zeeman sublevels, each has the same statistical weight. Each Zeeman sublevel corresponds to a value of quantum number  $M_J$  which is a quantum number of the projection of  $\vec{J}$  on the propagation axis of the pump beam. Therefore, the linear polarization of the probe beam is unchanged after passing through the sample, thus any light from probe laser reaches the detector D.

When the pump beam is on, let's assume that the wavelength of the pump laser is tuned to excite molecular transition  $J'' \rightarrow J'$ . Hence, the pump light depopulates the absorbing molecules at the lower level  $J''$  and then populates them to upper level  $J'$ . It is known that the depopulation for the lower level (or the population for the upper level) is not the same among the Zeeman sublevels because of the two following reasons. The first one is the selection rules for transitions between Zeeman sublevels:  $\Delta M = 0, +1, \text{ or } -1$  for linear, right circular-, or left circular polarization, respectively. The second one is dependence of absorption cross-section on value of  $M_J$ , as illustrated in fig.3.2. As a result the sample becomes anisotropic for the probe light. Therefore, whenever the probe light excites a transition which shares the lower or upper level with the pumped transition, the polarization of the probe beam changes and the probe beam passes through the polarizer  $P_2$  and reaches the detector. Detail description for anisotropy due to optical pumping can be found in [64-71].

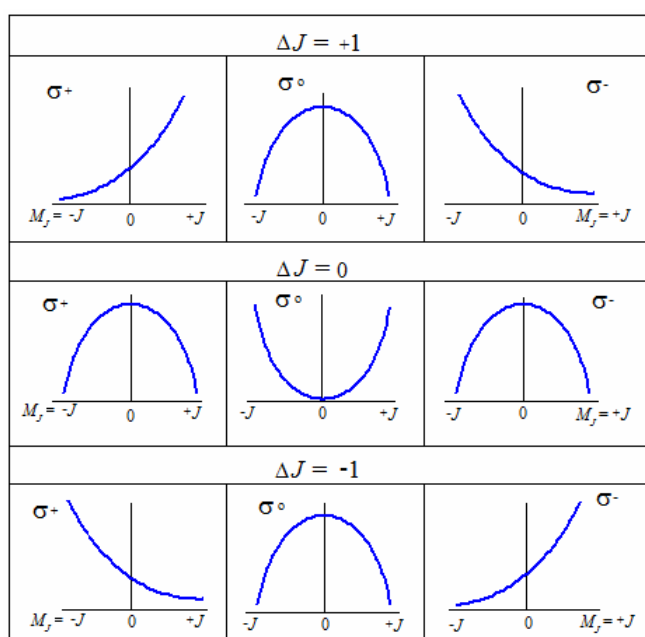


**Figure 3.2.**

$M_J$  - dependence of absorption cross-section [98]. The notations  $\sigma^+$ ,  $\sigma^-$ , and  $\sigma^0$  stand for right circular-, left circular-, and linear-polarization, respectively.

In the original version of PLS technique [27], wavelength of the probe laser was tunable whereas that of the pump laser was fixed. Consequently the PLS spectra exhibited rovibrational structure of electronic states on which probe transitions terminate. An alternative PLS version used in this work was based on a fixed-wavelength probe laser and a tunable pump laser [28]. Thus the PLS spectra exhibit rovibrational structure of electronic states on which pump transitions end on.

So summarizing, whenever the pump light is tuned to the transitions sharing common level with the probe transition, the polarization of the probe changes slightly. As a result, sweeping wavelength of the pump laser and monitoring probe light passing through the analyzer we obtain excitation spectrum of the molecule starting only from the chosen levels, as it is called labelled by the probe laser. In this way the spectrum is greatly simplified in comparison to the usual absorption spectrum and consequently, rotational resolution is obtained even for heavy molecules.

### 3.1.2 Amplitude of polarization signal

Let assume that the probe light propagates along  $z$  -axis and it is polarised in  $x$  - direction (this is the optical axis of the polarizer  $P_1$ )

$$\vec{E} = \vec{E}_o \exp[i(\omega t - kz)]; \quad \vec{E}_o = \{E_{ox}, 0, 0\}. \quad (3.1)$$

Let us consider the case of the circularly polarized pump light. The electric vector  $\vec{E}$  of the probe beam can be decomposed into left and right circularly polarized components in terms of the following expressions:

$$\vec{E}^+ = \vec{E}_o^+ \exp[i(\omega t - k^+ z)], \quad \vec{E}_o^+ = \frac{1}{2} E_o (\vec{e}_x + i\vec{e}_y) \quad (3.2a)$$

$$\vec{E}^- = \vec{E}_o^- \exp[i(\omega t - k^- z)], \quad \vec{E}_o^- = \frac{1}{2} E_o (\vec{e}_x - i\vec{e}_y). \quad (3.2b)$$

Here,  $\vec{e}_x$  and  $\vec{e}_y$  are unit vectors in the  $x$  and  $y$  directions, respectively;  $\vec{E}^+$  and  $\vec{E}^-$  are the right and left circularly polarized components, respectively. Passing through the sample of length  $L$  the two components experience a birefringence (due to the different refractive indexes  $n^+$  and  $n^-$ ) and dichroism (due to the different absorption coefficients  $\alpha^+$  and  $\alpha^-$ ). Therefore these two components of the probe beam after passing through the sample become

$$\vec{E}^+(z=L) = \vec{E}_o^+ \exp[i(\omega t - k^+ L + i \frac{\alpha^+}{2} L)], \quad (3.3a)$$

$$\vec{E}^-(z=L) = \vec{E}_o^- \exp[i(\omega t - k^- L + i \frac{\alpha^-}{2} L)]. \quad (3.3b)$$

Superposition of these two components yields an elliptic polarization

$$\vec{E} = \vec{E}^+ + \vec{E}^- = \frac{1}{2} E_o e^{i\omega t} e^{-i(\omega L/c - i\alpha L/2)} [(\vec{e}_x + i\vec{e}_y) e^{i\Delta} + (\vec{e}_x - i\vec{e}_y) e^{i\Delta}]. \quad (3.4)$$

Where,

$$n = \frac{1}{2}(n^+ + n^-); \quad \alpha = \frac{1}{2}(\alpha^+ + \alpha^-)$$

are the average quantities, and

$$\Delta = \omega L \Delta n / 2c - iL \Delta \alpha / 4$$

is phase factor which depending on the birefringence ( $\Delta n$ ) and dichroism ( $\Delta \alpha$ ):

$$\Delta n = n^+ - n^-; \quad \Delta \alpha = \alpha^+ - \alpha^-.$$

If the transmission axis of the analyser  $P_2$  is tilted with a small angle  $\theta \ll 1$  against the y-axis, the transmitted amplitude of the probe light could be written

$$E_t = E_x \sin \theta + E_y \cos \theta \approx E_x \theta + E_y. \quad (3.5)$$

For most practical cases  $\Delta \alpha L \ll 1$  and  $\Delta n L \ll 1$  thus one can expand  $\exp [i\Delta]$  into the Taylor series, retain the first term, and then substitute into (3.5). The transmitted amplitude is then given by

$$E_t = E_o \exp[i\omega t] \exp[i\omega n L / c - \frac{1}{2} \alpha L] (\theta - \Delta). \quad (3.6)$$

The polarization signal  $S(\omega)$  at the detector is proportional to the transmitted intensity given by:

$$\begin{aligned} S(\omega) &\propto I_t(\omega) = c \mathcal{E}_o E_t E_t^*, \\ I_t &= I_o e^{-\alpha L} (\xi + |\theta + \Delta|^2) \\ &= I_o e^{-\alpha L} \left[ \xi + \theta^2 + \frac{\omega}{c} \theta L \Delta n + \left( \frac{\omega}{c} L \Delta n \right)^2 + \left( \frac{L \Delta \alpha}{4} \right)^2 \right], \end{aligned} \quad (3.7)$$

where the  $\xi$ -coefficient was introduced due to imperfect extinction of the polarizers.

On the other hand from the Kramers-Krönig dispersion relation,  $\Delta n$  can be represented in terms of  $\Delta\alpha$  by:

$$\Delta n(\omega) = \frac{c}{\omega_0} \Delta\alpha(\omega)x = \frac{c}{\omega_0} \frac{\Delta\alpha(\omega_0)x}{1+x^2}, \quad (3.8)$$

where

$$x = \frac{2(\omega_0 - \omega)}{\gamma_s}, \quad \Delta\alpha(\omega) = \frac{\Delta\alpha(\omega_0)}{1+x^2} = \frac{\Delta\alpha_0}{1+x^2}, \quad (3.9)$$

and  $\omega_0$  central frequency of line with halfwidth  $\gamma_s$ .

Substituting (3.8) and (3.9) into (3.7) the transmitted intensity can be written as

$$I_t = I_o e^{-\alpha L} \left[ \xi + \theta^2 + \theta \Delta\alpha_0 L \frac{x}{1+x^2} + \left( \frac{\Delta\alpha_0 L}{4} \right)^2 \frac{1}{1+x^2} + 3 \left( \frac{L \Delta\alpha_0 x}{4(1+x^2)} \right)^2 \right]. \quad (3.10)$$

For the other case of linearly polarized pump light beam, maximum amplitude of the polarization signal appears when polarization planes of the pump and probe beams are tilted by  $45^\circ$ . In this case, the electric vector of the probe light could be decomposed into two components, one parallel and the other perpendicular to the polarization direction of the pump beam. After passing through the anisotropic sample the two components of the probe beam also experience the birefringence and dichroism in a similar way to the previously discussed case of the circularly polarized pump light. Therefore, the transmitted intensity could be written:

$$I_t = I_o e^{-\alpha L} \left[ \xi + \theta^2 - \theta \Delta\alpha_0 L \frac{x}{1+x^2} + \left( \frac{\Delta\alpha_0 L}{4} \right)^2 \frac{1}{1+x^2} + 3 \left( \frac{L \Delta\alpha_0 x}{4(1+x^2)} \right)^2 \right], \quad (3.11)$$

where  $\Delta\alpha_0$  is defined as the difference between  $\alpha_\perp$  and  $\alpha_\parallel$  for the perpendicular and parallel components, respectively.

If one tunes the wavelength of the probe laser into resonance and assuming  $\theta = 0$  (perfect crossing of the polarizer) both Eqs.(3.10) and (3.11) are reduced to

$$I_t = I_o e^{-\alpha L} \left[ \xi + \frac{(\Delta\alpha_0 L)^2}{16(1+x^2)} \right]. \quad (3.12)$$

The first term in (3.12) represents background signal ( $I_b$ ) due to the extinction of the polarizers, and the second term represents the polarization signal ( $I_p$ ), where:

$$I_b = I_o \xi \exp(-\alpha L) \quad (3.13a)$$

$$I_p = I_o e \exp(-\alpha L) \left[ \frac{(\Delta\alpha_o L)^2}{16(1+x^2)} \right]. \quad (3.13b)$$

At the resonance, a signal-to-background ratio can be estimated by

$$\frac{I_p}{I_B} = L^2 \frac{(\Delta\alpha_o)^2}{16\xi}. \quad (3.14)$$

Typical extinction of good quality polarizers is better than  $10^{-6}$  and the sensitivity of polarization spectroscopy is therefore greater several orders of magnitude in comparison to that of saturation spectroscopy [64].

### 3.1.3 Excitation schemes

There are five types of excitation scheme [69-70] which can give rise to polarization signal, as illustrated in figure 3.3.

In the type 1, also called V-type scheme, the pump and probe transitions share lower common rovibrational level in the ground electronic state. If wavelength of the probe light is fixed whereas that of pump laser is tuned over investigated spectral range, the polarization spectrum exhibits rovibrational structure of the upper electronic state in which the pumped transitions terminate.

In the type 2, also called  $\Lambda$ -type scheme, the pump and probe transitions share upper common rovibrational level, and the probe light dumps the pumped molecules into the rovibrational level in the lower electronic state. In this scheme, wavelength of the probe beam is tuned, thus the PLS spectrum reveals rovibrational structure of the electronic state in which the probe transition ends.

The transition scheme via type 3 is called step-wise scheme and occurs when the molecules in the upper level of the pumped transition absorb a photon of the probe light and they are excited to the higher levels. The step-wise PLS spectrum exhibits rovibrational structure of the electronic state in which the probe transition end.

After absorption of the pump-photon fluorescence to lower state occurs and populates unequally Zeeman sublevels in lower rovibrational levels (type 4 in fig. 3.3). If the probe beam excites molecules from one of these levels the polarization signal appears.

If we have high density of molecules or high pressure of inert (buffer) gas, collisional energy transfer between the pumped level and nearby rotational levels can be

efficient. Such process leads also to unequal populations of Zeeman sublevels and gives rise to polarization signal following scheme 5 in fig. 3.3.

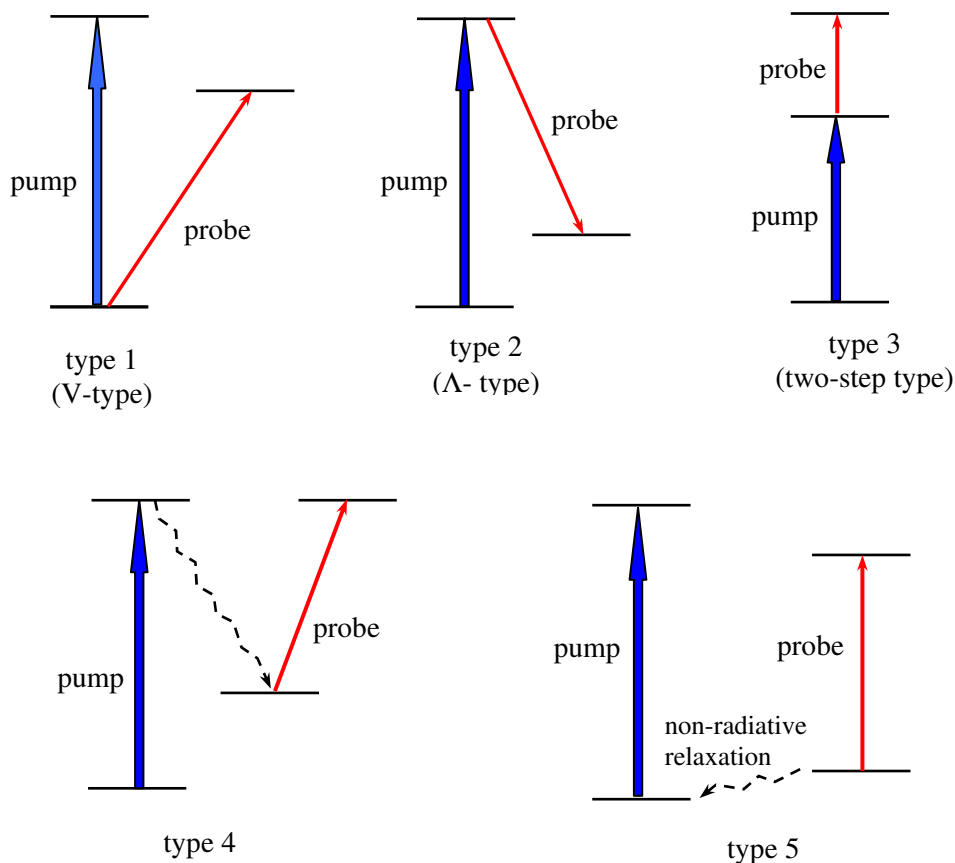


**Figure 3.3.** Excitation schemes in polarization labelling spectroscopy.

Actually PLS signals due to transitions via 4 and 5 types are rarely met in literature. Depending on particular purposes 1, 2, and 3 types are rather used. For instances, the  $\Lambda$ -type can be used to investigate the ground electronic state [32] while the V-type, and step-wise type is preferentially used for excited and Rydberg electronic states [33, 69].

### 3.1.4 Relative intensities of spectral lines

This section outlines expressions for relative intensities of spectral lines in V-type PLS scheme. Let us consider wavelength of the probe beam tuned to the centre of the line profile and let us neglect the background signal due to finite extinction of polarizers. Following (3.13b), the intensity of the polarization signal is given as

$$I_p = I_o \exp(-\alpha L) \left[ \frac{(\Delta\alpha_o L)^2}{16} \right] \propto (\Delta\alpha_o)^2. \quad (3.15)$$

By introducing notation for the set of quantum numbers of the levels  $(\Lambda_k, J_k, M_k)$ , where  $k = 1$  for upper level of the pumped transition,  $k = 2$  for the upper level of the probing transition, and  $k$  is omitted for the common lower level, the authors in [72] derived expressions of  $\Delta\alpha_o$  for cases of circularly and linearly polarized pump light as follows:

$$\Delta\alpha_o^{(C)} = \alpha^+ - \alpha^- = \frac{\Delta\sigma_o}{(2J_1 + 1)(2J_1 + 1)} S_{J_1 J}^{\Lambda_1 \Lambda} S_{J_2 J}^{\Lambda_2 \Lambda} \zeta_{J_2 J_1 J}^{(C)} \quad (3.16a)$$

$$\Delta\alpha_o^{(L)} = \alpha^z - \alpha^x = \frac{\Delta\sigma_o}{(2J_1 + 1)(2J_1 + 1)} S_{J_1 J}^{\Lambda_1 \Lambda} S_{J_2 J}^{\Lambda_2 \Lambda} \zeta_{J_2 J_1 J}^{(L)}. \quad (3.16b)$$

In these expressions the superscripts  $C$  and  $L$  denote the circular and linear polarizations of the pump beam, respectively;  $\Delta\sigma_o$  is a parameter depending on product of electronic transition dipole moment and the Franck-Condon factor;  $S$  is the Hönl-London factor describing intrinsic line strength of rotational intensity:

$$S_{J_1 J}^{\Lambda_1 \Lambda} = (2J + 1)(2J_1 + 1) \begin{pmatrix} J_1 & 1 & J \\ -\Lambda_1 & \Lambda_1 - \Lambda & \Lambda \end{pmatrix}^2. \quad (3.17)$$

The  $\zeta$ -factor describes the dependence of line intensity on "spatial distribution" of the angular momentum due to the optical pumping:

$$\begin{aligned} \zeta_{J_2 J_1 J}^{(C)} &= A_o (2J + 1) \\ &\times \sum_{M_2, M_1, M} \begin{pmatrix} J_1 & 1 & J \\ -M_1 & 1 & M \end{pmatrix}^2 \left[ \begin{pmatrix} J_2 & 1 & J \\ -M_2 & 1 & M \end{pmatrix}^2 - \begin{pmatrix} J_2 & 1 & J \\ -M_2 & -1 & M \end{pmatrix}^2 \right] \end{aligned} \quad (3.18a)$$

$$\begin{aligned} \zeta_{J_2 J_1 J}^{(L)} &= A_o (2J + 1) \times \sum_{M_2, M_1, M} \begin{pmatrix} J_1 & 1 & J \\ -M_1 & 0 & M \end{pmatrix}^2 \\ &\times \left\{ \begin{pmatrix} J_2 & 1 & J \\ -M_2 & 0 & M \end{pmatrix}^2 - \frac{1}{2} \left[ \begin{pmatrix} J_2 & 1 & J \\ -M_2 & -1 & M \end{pmatrix}^2 - \begin{pmatrix} J_2 & 1 & J \\ -M_2 & 1 & M \end{pmatrix}^2 \right] \right\}. \end{aligned} \quad (3.18b)$$

In the above expressions, the Wigner  $3j$ -symbols are used, and the summations are carried out over the  $M$ -sublevels.

For diatomic molecules having the ground states of  $^1\Sigma^+$ -symmetry, the selection rules (presented in chapter 2) show that the upper electronic states of the pumped or probe transitions are either of  $^1\Sigma^+$  or  $^1\Pi$  - symmetry. Thus the relative intensities between spectral lines can be derived by substituting expressions (3.16) - (3.18) into (3.15). Tables 3.1- 3.4 list relative intensities for P, Q, and R branches with all possible combinations of the probe and pump transitions, where for the sake of simplicity we present square roots of intensities [72].

**Table 3.1.** Relative intensities ( $\sqrt{I}$ ) in PLS spectrum when pumping via the  $^1\Pi \leftarrow ^1\Sigma^+$  band.

Pump	Probe via $^1\Pi \leftarrow ^1\Sigma^+$		
	P line	Q line	R line
<b>Cir - P line</b>	$\frac{3(J-1)^2(J+1)}{8J(2J-1)(2J+1)} \rightarrow \frac{3}{32}$	$\frac{3(J-1)}{8J(2J-1)} \rightarrow 0$	$\frac{3(J-1)(J+2)}{8(2J-1)(2J+1)} \rightarrow \frac{3}{32}$
<b>Cir - Q line</b>	$\frac{3(J-1)}{8J(2J+1)} \rightarrow 0$	$\frac{3}{8J(J+1)} \rightarrow 0$	$\frac{3(J+2)}{8(J+1)(2J+1)} \rightarrow 0$
<b>Cir - R line</b>	$\frac{3(J-1)(J+2)}{8(2J+1)(2J+3)} \rightarrow \frac{3}{32}$	$\frac{3(J+2)}{8(J+1)(2J+3)} \rightarrow 0$	$\frac{3J(J+2)^2}{8(J+1)(2J+1)(2J+3)} \rightarrow \frac{3}{32}$
<b>Lin - P line</b>	$\frac{3(J-1)^2(J+1)(2J+3)}{40J(2J-1)^2(2J+1)} \rightarrow \frac{3}{160}$	$\frac{3(J-1)(2J+3)}{40J(2J-1)} \rightarrow \frac{3}{40}$	$\frac{3(J-1)(J+2)}{40J(2J-1)(2J+1)} \rightarrow \frac{3}{160}$
<b>Lin - Q line</b>	$\frac{3(J-1)(2J+3)}{40J(2J+1)} \rightarrow \frac{3}{40}$	$\frac{3(2J-1)(2J+3)}{40J(J+1)} \rightarrow \frac{3}{10}$	$\frac{3(J+2)(2J-1)}{40(J+1)(2J+1)} \rightarrow \frac{3}{40}$
<b>Lin - R line</b>	$\frac{3(J-1)(J+2)}{40J(2J+1)(2J+3)} \rightarrow \frac{3}{160}$	$\frac{3(J+2)(2J-1)}{40(J+1)(2J+3)} \rightarrow \frac{3}{40}$	$\frac{3J(J+2)^2(2J-1)}{40(J+1)(2J+1)(2J+3)^2} \rightarrow \frac{3}{160}$

**Table 3.2.** Relative intensities ( $\sqrt{I}$ ) in PLS spectrum when pumping via the  $^1\Sigma^+ \leftarrow ^1\Sigma^+$  band.

Pump	Probe via $^1\Pi \leftarrow ^1\Sigma^+$		
	P line	Q line	R line
<b>Cir - P line</b>	$\frac{3(J-1)(J+1)}{4(2J-1)(2J+1)} \rightarrow \frac{3}{16}$	$\frac{3}{4(2J-1)} \rightarrow 0$	$\frac{3J(J+2)}{4(2J-1)(2J+1)} \rightarrow \frac{3}{16}$
<b>Cir - R line</b>	$\frac{3(J-1)(J+1)}{4(2J+1)(2J+3)} \rightarrow \frac{3}{16}$	$\frac{3}{4(2J+3)} \rightarrow 0$	$\frac{3J(J+2)}{4(2J+1)(2J+3)} \rightarrow \frac{3}{16}$
<b>Lin - P line</b>	$\frac{3(J-1)(J+1)(2J+3)}{20(2J-1)^2(2J+1)} \rightarrow \frac{3}{80}$	$\frac{3(2J+3)}{20(2J-1)} \rightarrow \frac{3}{20}$	$\frac{3J(J+2)}{20(2J-1)(2J+1)} \rightarrow \frac{3}{80}$
<b>Lin - R line</b>	$\frac{3(J-1)(J+1)}{20(2J+1)(2J+3)} \rightarrow \frac{3}{80}$	$\frac{3(2J-1)}{20(2J+3)} \rightarrow \frac{3}{20}$	$\frac{3J(J+2)(2J-1)}{20(2J+1)(2J+3)^2} \rightarrow \frac{3}{80}$

**Table 3.3.** Relative intensities ( $\sqrt{I}$ ) in PLS spectrum when pumping the  ${}^1\Pi \leftarrow {}^1\Sigma^+$  band.

Pump	Probe via ${}^1\Sigma^+ \leftarrow {}^1\Sigma^+$	
	P line	R line
<b>Cir</b> - P line	$\frac{3(J-1)(J+1)}{4(2J-1)(2J+1)} \rightarrow \frac{3}{16}$	$\frac{3(J-1)(J+1)}{4(2J-1)(2J+1)} \rightarrow \frac{3}{16}$
<b>Cir</b> - Q line	$\frac{3}{4(2J+1)} \rightarrow 0$	$\frac{3}{4(2J+1)} \rightarrow 0$
<b>Cir</b> - R line	$\frac{3J(J+2)}{4(2J+1)(2J+3)} \rightarrow \frac{3}{16}$	$\frac{3J(J+2)}{4(2J+1)(2J+3)} \rightarrow \frac{3}{16}$
<b>Lin</b> - P line	$\frac{3(J-1)(J+1)(2J+3)}{20(2J-1)^2(2J+1)} \rightarrow \frac{3}{80}$	$\frac{3(J-1)(J+1)}{20(2J-1)(2J+1)} \rightarrow \frac{3}{80}$
<b>Lin</b> - Q line	$\frac{3(2J+3)}{20(2J+1)} \rightarrow \frac{3}{20}$	$\frac{3(2J-1)}{20(2J+1)} \rightarrow \frac{3}{20}$
<b>Lin</b> - R line	$\frac{3J(J+2)}{20(2J+1)(2J+3)} \rightarrow \frac{3}{80}$	$\frac{3J(J+2)(2J-1)}{20(2J+1)(2J+3)^2} \rightarrow \frac{3}{80}$

**Table 3.4.** Relative intensities ( $\sqrt{I}$ ) in PLS spectrum when pumping via the  ${}^1\Sigma^+ \leftarrow {}^1\Sigma^+$  band.

Pump	Probe via ${}^1\Sigma^+ \leftarrow {}^1\Sigma^+$	
	P line	R line
<b>Cir</b> - P line	$\frac{3J(J+1)}{2(2J-1)(2J+1)} \rightarrow \frac{3}{8}$	$\frac{3J(J+1)}{2(2J-1)(2J+1)} \rightarrow \frac{3}{8}$
<b>Cir</b> - R line	$\frac{3J(J+1)}{2(2J+1)(2J+3)} \rightarrow \frac{3}{8}$	$\frac{3J(J+1)}{2(2J+1)(2J+3)} \rightarrow \frac{3}{8}$
<b>Lin</b> - P line	$\frac{3J(J+1)(2J+3)}{10(2J-1)^2(2J+1)} \rightarrow \frac{3}{40}$	$\frac{3J(J+1)}{10(2J-1)(2J+1)} \rightarrow \frac{3}{40}$
<b>Lin</b> - R line	$\frac{3J(J+1)}{10(2J+1)(2J+3)} \rightarrow \frac{3}{40}$	$\frac{3J(J+1)(2J-1)}{10(2J+1)(2J+3)^2} \rightarrow \frac{3}{40}$

## 3.2. Experimental

### 3.2.1 Preparation of NaLi molecules

Production of NaLi molecules from metallic Na and Li bulks encounters a difficulty because of the big difference in melting-points of both substances ( $T_1= 180.54^\circ\text{C}$  for Li and  $T_2= 97.8^\circ\text{C}$  for Na) and consequently big difference in concentration of Na and Li atoms in the saturated vapour. In order to overcome such difficulty we used the three-section heat-pipe, which was proposed in [73] to form NaLi molecules. The main arrangement of the apparatus (fig.3.4) is briefly described below.

The heat-pipe oven is made from a stainless steel pipe which is surrounded by three heaters connected to the separated power supplies that allow independent control of the temperature of each heater. The temperature of the each section of the pipe is measured with a chromel-alumel thermocouple placed between the heater and the pipe wall. At both ends, the pipe is closed with fused silica windows which are fixed by easily demountable clamped flanges. The windows are kept by rubber O-rings and adjustable screws which allow compensation of residual birefringence by gently squeezing. Both windows are tilted against the tube axis in order to eliminate multi-reflection between the windows. Two stainless steel pipes are welded at the ends of the pipe for connection to vacuum systems. At each end of the pipe two water-cooler rings are soldered. Three layers of steel mesh are inserted into the tube in order to assure circulation of the liquid metal by capillary forces. The mesh matches the distance between the water coolers. A metallic Li is loaded to the central part of the heat-pipe while Na is placed at outer parts. About 4 Torr of Helium is filled into the pipe as buffer gas.

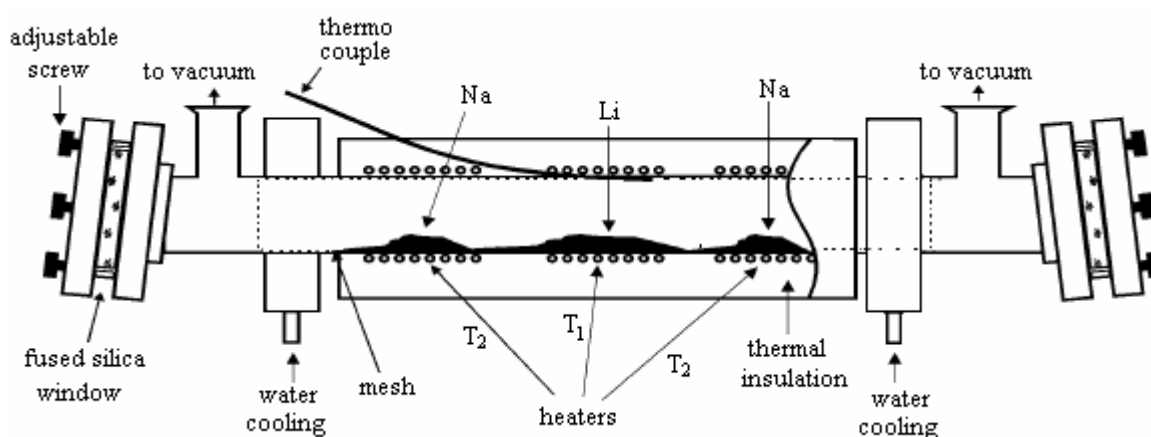


**Figure 3.4.** The three-section heat-pipe oven.

It was found that the best stable condition for forming NaLi molecules can be achieved with the temperature  $T_1 = 650^\circ\text{C}$  (for the central heater) and  $T_2 = 390^\circ\text{C}$  (for the outer ones). The NaLi molecules were produced mainly in the central zone of the pipe and could be maintained in several hours, which was enough long time for us to perform measurements.

### 3.2.2 Laser sources

#### a. Pump lasers

The purpose of our experiments was to investigate electronic states of NaLi in a wide spectral energy range, from 24500 up to 36000  $\text{cm}^{-1}$  by V-type PLS. In order to cover such spectral energy range we used two pump laser systems. The first one based on dye laser whereas the second based on optical parametric oscillator/amplifier (OPO/OPA).

- **Dye laser system.**

The dye laser system was the Lumonics HD 500 operating on BBQ, Butyl PBD, and BBD dyes pumped by a 308 nm XeCl excimer laser. The dye laser scans were controlled by a remote controller or by a software equipped computer. This laser generates light pulses with pulse energy of about 2 mJ, width 8 ns, and linewidth of less than 0.1  $\text{cm}^{-1}$ . Using three dyes mentioned above laser system was tunable in the 24500-27800  $\text{cm}^{-1}$  spectral range.

- **OPO/OPA- Frequency doubler system.**

The system consists of Nd:YAG (3<sup>rd</sup> harmonic, 355nm) pumped optical parametric oscillator/amplifier (OPO/OPA) and a frequency doubler. The laser system can be controlled from a computer via RS-232 interface to scan wavelength in desired spectral ranges. It generated light-pulses with energy of about 4 mJ, 10 Hz repetition rate and linewidth of 0.15  $\text{cm}^{-1}$ . With this system wavelength of radiation was tunable in 28900 - 40000  $\text{cm}^{-1}$  spectral range.

#### b. Probe lasers

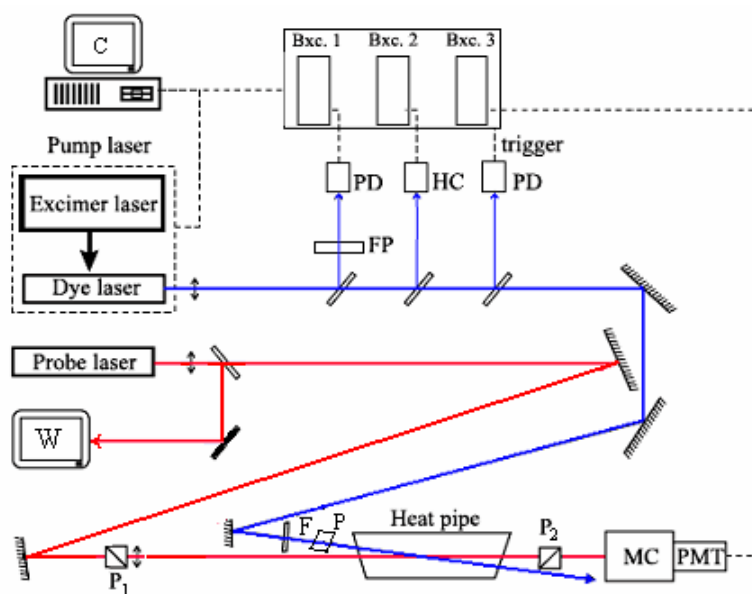
The probe laser was either a multi-mode CW ion Ar<sup>+</sup> laser (Carl Zeiss ILA 120) or a home-built Littman type dye laser. The Ar<sup>+</sup> laser was set at 496.5 nm line with power of about 40 mW. This laser line excites the  $1^1\Pi(1, 29) \leftarrow 1^1\Sigma^+(0, 30)$  transition what was known from literature in previous measurements in laboratory [16, 17]. The home-built Littman type laser operated on DCM dye, and was pumped by either the excimer or Nd:YAG laser. The dye laser generated radiation with energy pulse of about 0.003 mJ and was tuned to excite desired transitions via the  $2^1\Sigma^+ \leftarrow 1^1\Sigma^+$  band system [15-16]. The laser lines corresponding to the particular probe transition are listed in table 3.5.

**Table 3.5.** The laser lines used in this work as a probe.

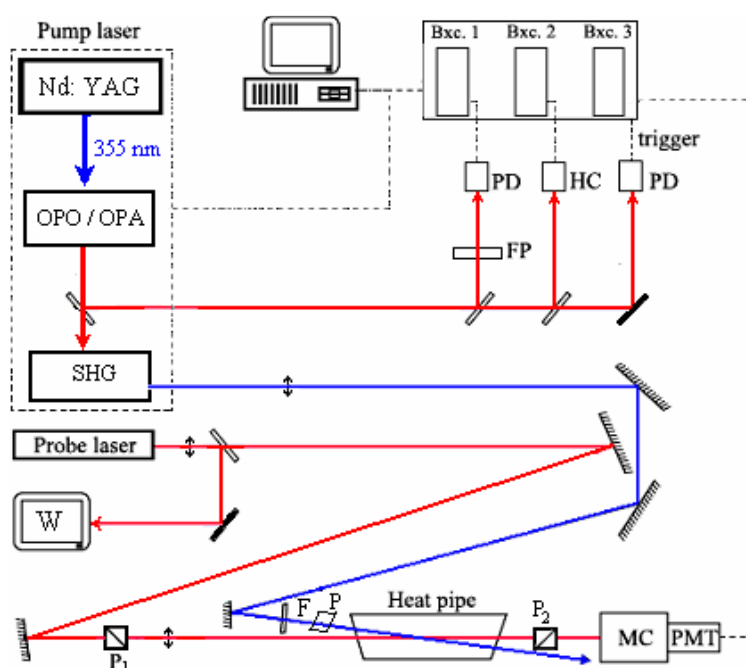
laser line	probe transition ( $v', J'$ ) $\leftarrow$ ( $v'', J''$ )
496.5 nm	$1^1\Pi(1, 29) \leftarrow 1^1\Sigma^+(0, 30)$
15293.3 $\text{cm}^{-1}$	$2^1\Sigma^+(8, 20) \leftarrow 1^1\Sigma^+(1, 21)$
15413.0 $\text{cm}^{-1}$	$2^1\Sigma^+(9, 28) \leftarrow 1^1\Sigma^+(0, 29)$
15440.2 $\text{cm}^{-1}$	$2^1\Sigma^+(9, 24) \leftarrow 1^1\Sigma^+(1, 25)$
15463.8 $\text{cm}^{-1}$	$2^1\Sigma^+(9, 20) \leftarrow 1^1\Sigma^+(1, 21)$ $2^1\Sigma^+(11, 55) \leftarrow 1^1\Sigma^+(1, 56)$
15484.2 $\text{cm}^{-1}$	$2^1\Sigma^+(9, 16) \leftarrow 1^1\Sigma^+(1, 17)$
15493.5 $\text{cm}^{-1}$	$2^1\Sigma^+(8, 28) \leftarrow 1^1\Sigma^+(0, 29)$ $2^1\Sigma^+(9, 46) \leftarrow 1^1\Sigma^+(0, 47)$
15521.2 $\text{cm}^{-1}$	$2^1\Sigma^+(8, 24) \leftarrow 1^1\Sigma^+(0, 25)$ $2^1\Sigma^+(9, 11) \leftarrow 1^1\Sigma^+(1, 10)$
15544.8 $\text{cm}^{-1}$	$2^1\Sigma^+(8, 20) \leftarrow 1^1\Sigma^+(0, 21)$
15560.6 $\text{cm}^{-1}$	$2^1\Sigma^+(8, 17) \leftarrow 1^1\Sigma^+(0, 18)$ $2^1\Sigma^+(9, 44) \leftarrow 1^1\Sigma^+(0, 45)$
15565.4 $\text{cm}^{-1}$	$2^1\Sigma^+(8, 16) \leftarrow 1^1\Sigma^+(0, 17)$

### 3.2.3 Experimental arrangement

Depending on which pump laser was used, our experimental setup was arranged as shown either in fig 3.5 or in fig. 3.6. In each arrangement the pump and probe laser beams passed nearly collinearly through the heat-pipe oven. Before and after the heat-pipe, two Glan-Thomson polarizers ( $P_1$ ,  $P_2$ ) were placed on the optical path of the probe beam. These polarizers were fixed in rotating mounts for fine tuning of their optical axes. In order to measure the wavelength of the probe beam, a small amount of radiation, extracted with the beam splitter from the main beam, was directed into a WS5-wavelength meter. The change of the polarization (circular or linear) of the pump beam was obtained by inserting a  $\lambda/4$  Fresnel rhomb before the heat-pipe into the optical path of the pump beam. The PLS signal after the polarizer  $P_2$  was registered with a photomultiplier tube. Before the photomultiplier, a monochromator was placed to suppress scattered light and fluorescence outgoing from the heat-pipe oven. The signal from the photomultiplier was measured by a Stanford SR 250- boxcar averager.

**Figure 3.5.**

Arrangement for V-type PLS with the dye laser system as pump laser. F-Fresnel rhomb, P-polarizer, MC-monochromator, PMT-photomultiplier tube, W-wavelength meter, FP-Fabry-Pérot interferometer, PD-photodiode, bxc-boxcar, HC-hollow cathode lamp, C-microcomputer.

**Figure 3.6.**

Arrangement for V-type PLS using the Frequency doubler-OPO/OPA system as the pump laser. The symbols are the same as in fig. 3.5.

There was a slight difference between the two arrangements. In the first one, fractions of the pump beam were directed to a Fabry-Pérot (FP) interferometer (free spectral range of about  $1 \text{ cm}^{-1}$ ) and to an Argon hollow-cathode lamp (HC) lamp were recorded by boxcars connected to a computer via a computer interface

SR-245. Both transmission peaks and optogalvanic lines were used for absolute calibration of wavelength of PLS spectrum. In the second arrangement, the fundamental beam (from the OPA) was used for the FP interferometer and HC lamp. This choice was convenient to adjust the laser beams for the HC lamp and FP interferometer.

### **3.3. Determination of the absolute wavelength in PLS spectrum**

In order to determine the absolute wavelength of the PLS spectrum we referred the PLS spectrum to the known wavelengths of Ar lines registered by the optogalvanic method. Actually the optogalvanic spectrum, the FP fringes, and PLS spectrum were recorded as functions of steps of the electric motor which tuned laser cavity. First we assigned the absolute wavenumber of the observed optogalvanic lines by comparing to the reference spectrum of Ar [74]. From the correspondence between the steps and wavenumbers of the reference lines, each point (in step) of the PLS spectrum could be converted into wavenumber. But such procedure, based on assumption that wavenumbers are perfectly linear as a function of steps, has been too rough. In order to improve precision of calibration by numerical linearization of the scan the fringes from the FP interferometer were used. With the assumption that the free-spectral range of the FP does not change during the scan, we used transmission peaks from the FP interferometer as a pattern of equidistant markers for numerical calibration of the PLS spectra.

Finally experimental precision of calibration was estimated to be  $0.05 \text{ cm}^{-1}$ . For measurements with the OPO system, we registered optogalvanic spectrum on the fundamental wave while the PLS spectra were induced by the second harmonic one. Thus this gave  $0.1 \text{ cm}^{-1}$  as the accuracy of calibration.

## Chapter 4

### Experimental results for the NaLi molecule

#### 4.1. Introduction

##### 4.1.1 Historical overview of investigations of NaLi

The electronic structure of NaLi was explored theoretically for the first time by Bertoncini *et al* [19] in 1970, where authors performed *ab initio* calculations by using the multiconfiguration self-consistent field method. They computed four potential curves for the  $1^1\Sigma^+$ ,  $1^3\Sigma^+$ ,  $1^1\Pi$ , and  $1^3\Pi$  states and the dipole moment for the ground state. Their results anticipated that the NaLi molecule, which had not been observed spectroscopically until that time, is physically stable with dissociation energy of  $6850\text{ cm}^{-1}$  in the ground state. Later, Green [20] performed calculations of electric dipole moment for the ground state within the framework of the configuration interaction (CI) theory. The author revealed that the value of the dipole moment obtained in [19], which was 1.24 debye, is too large owing to neglect in the previous calculations of contributions from core-polarization effects. Green's prediction was later tested experimentally by Graff, Dagdigian and Wharton [25-26], and results showed that the value of the dipole moment in the electronic ground state of NaLi is only 0.46 debye. In the following years the dynamical core-polarization effects in alkali dimer species were taken into consideration by Meyer's group [21-23]. The authors introduced operators which are responsible for the core-core and valence-core interactions into the standard Hamiltonian of the self-consistent field method. Upon these considerations they computed potential energy curves and some main spectroscopic constants for the electronic ground state of several alkali dimers, including NaLi. By using this method, Schmidt-Mink *et al* [24] computed potential energy curves and spectroscopic constants for the first sixteen singlet and triplet electronic states of NaLi. The calculated spectroscopic constants for the first six singlet states ( $1^1\Sigma^+$ ,  $2^1\Sigma^+$ ,  $1^1\Pi$ ,  $2^1\Pi$ ,  $3^1\Sigma^+$ , and  $4^1\Sigma^+$ ) were then confirmed by experimental works [12-18] with good overall agreement. Very recently, Mabrouk *et al* [79] treated the first forty electronic states of NaLi by using

the parameterized  $l$ -dependent polarization potential and full configuration interaction calculations. Their values of spectroscopic constants for several electronic states were compared to those obtained in previous experiments, including the  $3^1\Pi$  and  $4^1\Pi$  states observed for the first time in our work. The comparison showed very good agreement with experimental results to within 1.3% relative error. In figure 4.4 we plotted all computed PECs of singlet states from [79].

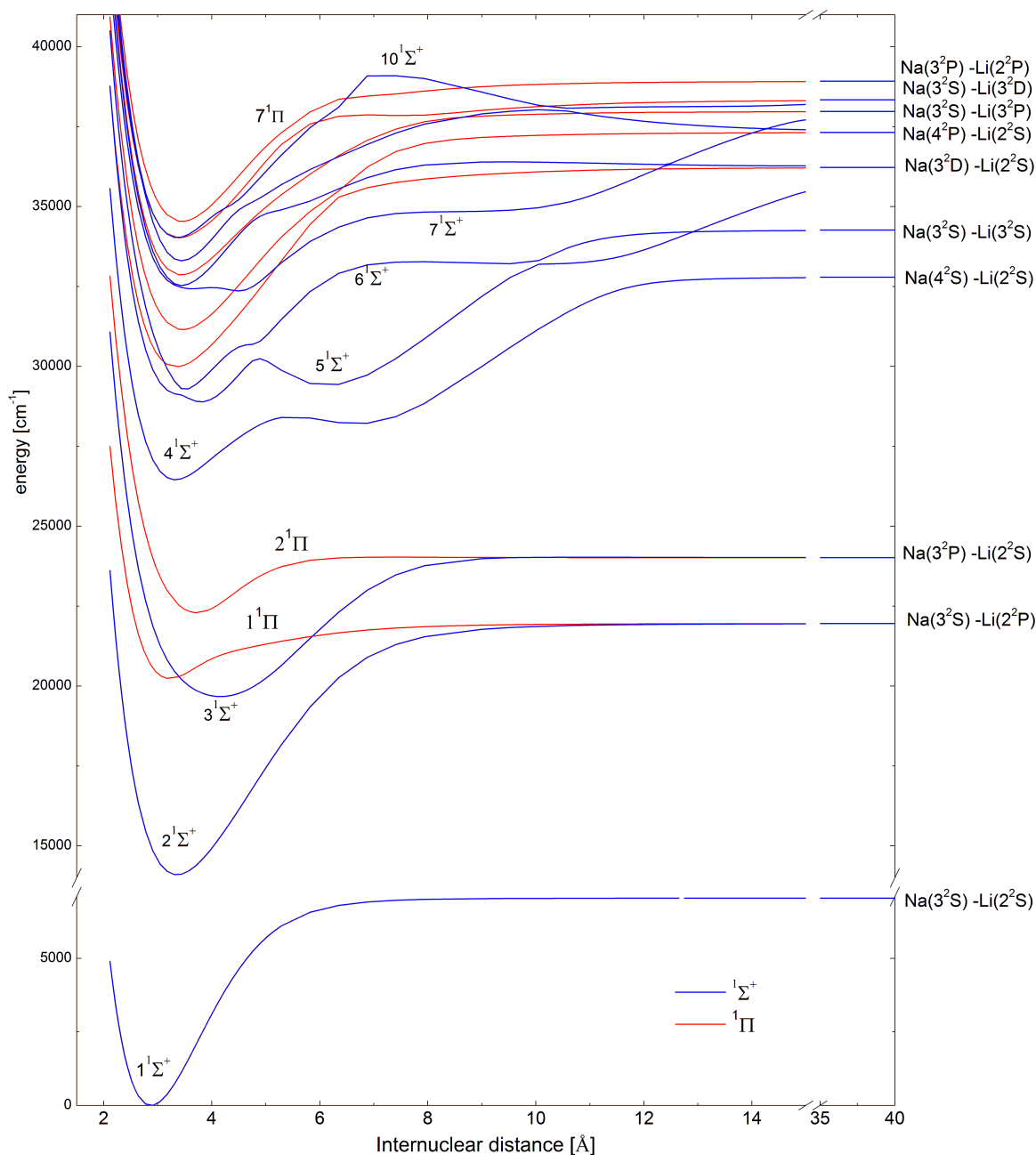


**Figure 4.1.** The PECs of the 1-7 $^1\Pi$  and 1-10 $^1\Sigma^+$  states of NaLi calculated by Mabrouk *et al* [79]. The blue curves stand for  $^1\Sigma^+$  states, and the red ones for  $^1\Pi$  states.

On the experimental side, the spectroscopic study of rovibrational structure in electronic states of NaLi encounters two drawbacks. The first one is the difficulty in producing sufficiently stable concentration of NaLi molecules in the vapour phase. The second one is overlap of the NaLi spectra with spectra of Na<sub>2</sub> and Li<sub>2</sub> which makes their interpretation very difficult. Therefore, despite several attempts since 1928 (see [10] and references therein), the spectrum of NaLi has not been observed until in 1971 Hessel [11] demonstrated for the first time experimental observation of spectrum of NaLi molecule by using laser-induced fluorescence (LIF). He observed fluorescence of transitions assigned to the  $1^1\Pi \rightarrow 1^1\Sigma^+$  band system after excitation with the 496 nm Ar<sup>+</sup> laser line. Since then several groups performed experiments to explore rovibrational structure in electronic states of NaLi. Much attention was focused on the ground state [12, 14-15], and the most accurate measurements were carried out by Fellows [15]. He used the LIF technique combined with Fourier transform spectroscopy and observed over 6400 spectral lines up to almost the dissociation limit of the ground state (experimental data covered 99.5% of the potential well depth). This resulted in determination of spectroscopic constants and the rotationless potential energy curve. For excited states, Kappe *et al* [13] used two-photon ionization techniques to access vibrational structure of the  $2^1\Sigma^+$ ,  $2^1\Pi$ ,  $3^1\Sigma^+$ ,  $4^1\Sigma^+$ , and  $5^1\Sigma^+$  states. Since the experiment was carried out at low resolution (typically 2 cm<sup>-1</sup>), this allowed determination of only a number of molecular constants ( $T_e$ ,  $\omega_e$ ,  $\omega_e x_e$ , and  $D^e$ ), in particular without rotational constants. Next, Fellows [16] reinvestigated the  $2^1\Sigma^+$  state by means of the LIF combined with Fourier transform spectroscopy, and determined molecular constants and the RKR potential. Latter, the same technique was used again by Fellows *et al* [17] to reinvestigate the  $1^1\Pi$  and  $3^1\Sigma^+$  states. Perturbations in spectra of  $1^1\Pi$  and  $3^1\Sigma^+$  as well as energy transfer from  $1^1\Pi$  to  $3^1\Sigma^+$  were experimentally confirmed. Recently, Jastrzębski *et al* [18] performed experiments to investigate the  $4^1\Sigma^+$  state. Those authors used the V-type PLS technique in which the 496.5 nm Ar<sup>+</sup> laser line was used as a probe light beam to explore the rovibrational structure of the  $4^1\Sigma^+$  state. A progression of first ten vibrational levels in the  $4^1\Sigma^+ \leftarrow 1^1\Sigma^+$  (0, 30) band, which consists of two P and R doublets, was identified. Even though data set acquired in that work was rather sparse it was still the first experiment able to resolve the rotational structure in the  $4^1\Sigma^+$  state of the NaLi molecule.

### 4.1.2 Outline of the electronic states observed in this work

In this work we focussed on investigations of excited electronic states of the NaLi molecule, particularly the states which were not observed before. We performed V-type PLS experiments to observe transitions over a wide spectral energy range, from 26000 to 36300  $\text{cm}^{-1}$ , and found spectral lines of transitions from the ground state to several  $^1\Sigma^+$  and  $^1\Pi$  states.

The spectra of the lowest  $^1\Sigma^+$ - symmetry state observed in this work were found in the range 26000-27500  $\text{cm}^{-1}$ . We readily identified this state as the  $4^1\Sigma^+$  (see sect.4.3) since preliminary molecular constants for this state were known from a previous experiment [18].

We have also found several spectral lines in the range 28900 - 36000  $\text{cm}^{-1}$  belonging to the  $5^1\Sigma^+$ ,  $6^1\Sigma^+$ ,  $7^1\Sigma^+$ ,  $8^1\Sigma^+$ ,  $9^1\Sigma^+$ , and  $10^1\Sigma^+$  states which are expected in this region on the basis of theoretical calculations. However the observed lines did not form any regular pattern because of very irregular shapes of the potential energy curves for the  $^1\Sigma^+$  states (fig. 4.1) and the unambiguous assignment and interpretation was not possible.

Therefore we have concentrated on  $^1\Pi$  states which gave rise to much more regular spectral patterns making their analysis possible. Finally we have identified observed states as  $3^1\Pi$ ,  $4^1\Pi$ ,  $6^1\Pi$  and  $7^1\Pi$ . In order to perform such assignment first we compared experimentally determined electronic energy  $T_e$  obtained for each state with theoretical predictions. Such preliminary assignment gave also atomic asymptotes for each state, following theoretical calculations [79]. With  $T_e = 29981.6, 31179.0, 34042.3, 34535.8$  and  $35985.4 \text{ cm}^{-1}$  (section 4.4 - 4.6) obtained for successive states of  $^1\Pi$ -symmetry we assigned the observed states as:



Having this assignment and knowing the dissociation energy of the ground state  $D^e[1^1\Sigma^+] = 7105.5 \text{ cm}^{-1}$  [15] and energy of atomic levels [75] we could calculate the dissociation energy ( $D^e$ ) of each state. Since dissociation energies were independently determined in the theoretical paper [79] this gave additional support for the assignment (4.1) ÷ (4.4). Following (4.1) ÷ (4.4) we obtained the dissociation energy for each state:

$$D^e[3^1\Pi] = \bar{\nu}[\text{Na}(3^2D - 3^2S)] + D^e[1^1\Sigma^+] - T_e[3^1\Pi] = 6296.8 \text{ cm}^{-1} \quad (4.1a)$$

$$D^e[4^1\Pi] = \bar{\nu}[\text{Na}(4^2P - 3^2S)] + D^e[1^1\Sigma^+] - T_e[4^1\Pi] = 6193 \text{ cm}^{-1} \quad (4.2a)$$

$$D^e[6^1\Pi] = \bar{\nu}[\text{Li}(3^2D - 2^2S)] + D^e[1^1\Sigma^+] - T_e[6^1\Pi] = 4346 \text{ cm}^{-1} \quad (4.3a)$$

$$D^e[7^1\Pi] = \bar{\nu}[\text{Li}(2^2P - 2^2S)] + \bar{\nu}[\text{Na}(3^2P - 3^2S)] + D^e[1^1\Sigma^+] - T_e[7^1\Pi] \\ = 4429 \text{ cm}^{-1}. \quad (4.4a)$$

Comparison of our values for electronic and dissociation energies with those calculated in the theoretical paper [79] shows good agreement (deviations are smaller than  $24 \text{ cm}^{-1}$  for  $T_e$  and then  $61 \text{ cm}^{-1}$  for  $D^e$ ), and demonstrates consistency between our assignment for the observed electronic states and assignment in [79]. However, it is surprising that the above assignment leads to missing observation of the  $5^1\Pi$  state even though we did observations throughout the whole spectral region between the  $3^1\Pi$  and  $7^1\Pi$  states. Discussion of the missing observation of the  $5^1\Pi$  state is presented at the end of this chapter.

## 4.2. Methods of data analysis

In order to derive molecular constants of an electronic state, the experimental term values/level energies were fitted to the Dunham formula by using the linear least-squares method. The fitted Dunham coefficients were derived by minimizing the following quantities:

1. Standard error of the individual coefficient.
2. Deviation between the calculated and experimental values for each line.
3. The dimensionless root mean square deviation, *DRMSD*, which is given by

$$DRMSD = \left( \frac{1}{N} \sum_{i=1}^N \left[ \frac{\bar{\nu}_{obs}(i) - \bar{\nu}_{cal}(i)}{\Delta u(i)} \right]^2 \right)^{\frac{1}{2}}, \quad (4.5)$$

where  $N$  is the number of the observed lines,  $\Delta u(i)$  is experimental uncertainty which is taken to be  $0.1 \text{ cm}^{-1}$  for our work,  $\bar{\nu}_{obs}(i)$  and  $\bar{\nu}_{cal}(i)$  are the measured and calculated wavenumbers of the  $i^{th}$  transition, respectively.

In practice, the number of Dunham coefficients is not defined a priori. If the number of coefficients is large this leads to small *DRMSD*, but increase the error (ambiguity) of determined coefficients, so we search for the optimal set of Dunham coefficients looking for the minimum of all above listed quantities.

For the construction of a potential energy curve by the IPA technique also the linear least squares method is used to determine coefficients for the potential correction. Since in this technique the minimization for the *DRMSD* leads to an over-determined system of equations of unknown coefficients, therefore the singular value decomposition (SVD) method [76] is used.

For construction of a potential curve by the DPotFit technique [58] the nonlinear least squares method has to be used because in the DPotFit the eigenvalues of the RSE are nonlinearly dependent on unknown coefficients of a chosen analytical potential function. Therefore, unlike in the linear least squares method, in the nonlinear least squares one needs trial values for the unknown coefficients and then it goes to search iteratively corrections for these coefficients until a convergence is obtained.

### 4.3. The $4^1\Sigma^+$ state

#### 4.3.1 Observation and assignment of the spectra

Spectra of the  $4^1\Sigma^+$  state of NaLi were observed in region 26000-28000  $\text{cm}^{-1}$  for various labelled levels (table 3.5) in the ground electronic state. The pump light was delivered by a 308nm excimer laser-pumped HD 500 dye laser, and was circularly polarized.

Although the  $4^1\Sigma^+$  state was already characterized with some preliminary molecular constants [18] within the current experiment we improved significantly its description by enlarging almost 10 times number of lines used for analysis. Finally we identified 190 spectral lines of the  $4^1\Sigma^+ \leftarrow 1^1\Sigma^+$  band, spanning the range  $v = 0 - 11$ ,  $J = 9 - 46$  in  $4^1\Sigma^+$ . The theoretical calculation of Schmidt-Mink et al [24] shows that the  $4^1\Sigma^+$  state is characterized by a double minimum potential; all presently observed levels are confined in the inner potential well and their numbering follows the progression in this well.

Figure 4.2 shows a part of PLS spectrum in the case of 15486.1  $\text{cm}^{-1}$  probe laser line. This laser line excites three transitions corresponding to the three labelled levels, (0, 30), (1, 21) and (1, 40) in the ground state. In fig. 4.4, the distribution of the data in the field of rotational and vibrational quantum numbers in the  $4^1\Sigma^+$  state is plotted.

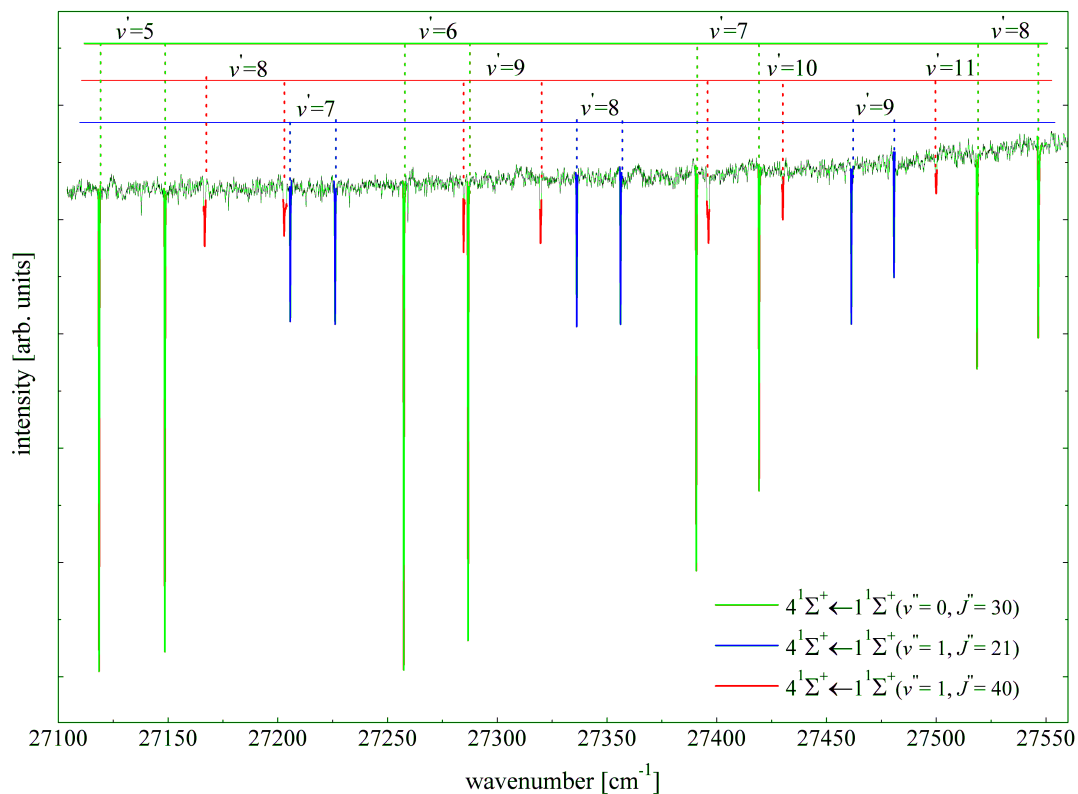


**Figure 4.2.** A part of the PLS spectrum consisting of P and R lines when pump beam is circularly polarized and probe set at  $15486.1 \text{ cm}^{-1}$  excites simultaneously three transitions starting from levels (0,30), (1,21) and (1,40) in the ground state. The vibrational quantum numbers for each progression are shown.

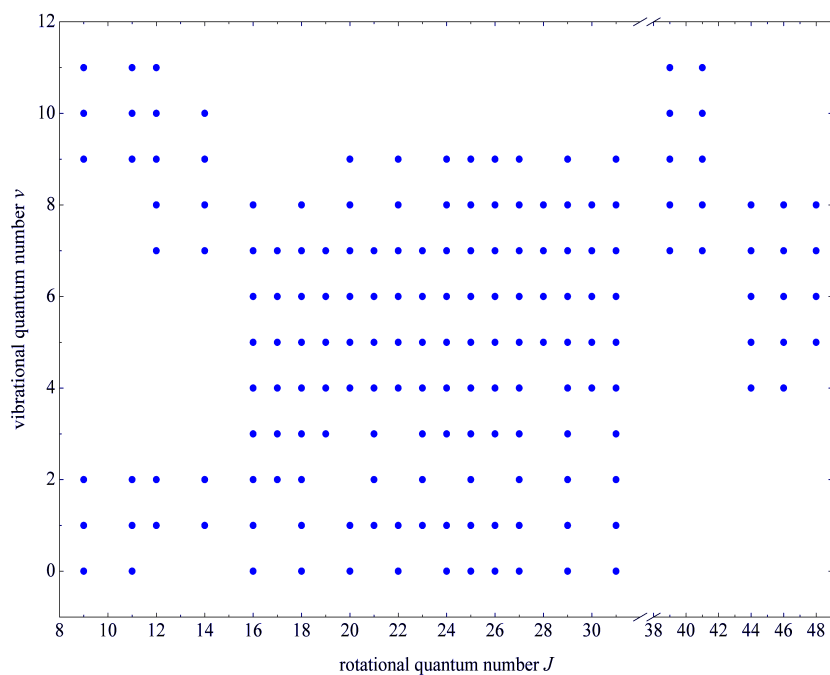


**Figure 4.3.** Distribution of the experimental data for the  $4^1\Sigma^+$  state in NaLi.

### 4.3.2 Molecular constants

In order to derive molecular constants for the  $4^1\Sigma^+$  state the wavenumbers of all observed spectral lines were fitted to the formula:

$$\bar{\nu} = T'(v', J') - T''(v'', J''), \quad (4.6)$$

where  $T'$  and  $T''$  are the spectroscopic term values of the investigated and ground electronic states, respectively. The term values for the labelled levels were calculated by using Dunham coefficients obtained from [15] and fixed during the fitting procedure. The final set of Dunham coefficients for the  $4^1\Sigma^+$  state reproduced the experimental levels with  $DRMSD = 0.44$ . Table 4.1 contains the list of the obtained Dunham coefficients with values obtained theoretically [24] and from previous experiment [18].

**Table 4.1.** Dunham coefficients of the  $4^1\Sigma^+$  state of NaLi.

Coefficient	value [ $\text{cm}^{-1}$ ]	uncertainty [ $\text{cm}^{-1}$ ]	Error (%)	References
$T_e$	26474.64	0.042	$1.59 \times 10^{-7}$	This work
	26474.82			[18] - experiment
	26416			[24] - theory
$Y_{10}$	178.893	0.052	$2.9 \times 10^{-2}$	This work
	180.29			[18]-experiment
	181.66			[24]-theory
$Y_{20}$	-1.952	0.023	1.18	This work
	-3.10			[18]-experiment
	-3.166			[24]-theory
$Y_{30}$	-0.2756	$0.46 \times 10^{-2}$	1.67	This work
$Y_{40}$	$0.2826 \times 10^{-1}$	$0.43 \times 10^{-3}$	1.52	This work
$Y_{50}$	$-0.960 \times 10^{-3}$	$0.15 \times 10^{-4}$	1.56	This work
$Y_{01}$	0.280441	$0.71 \times 10^{-4}$	0.025	This work
	0.28061			[18]-experiment
	0.2812			[24]-theory
$Y_{11}$	$-0.3509 \times 10^{-2}$	$0.65 \times 10^{-4}$	1.86	This work
	$-0.452 \times 10^{-2}$			[18]-experiment
	$-0.425 \times 10^{-2}$			[24]-theory
$Y_{21}$	$-0.603 \times 10^{-3}$	$0.20 \times 10^{-4}$	3.33	This work
$Y_{31}$	$0.738 \times 10^{-4}$	$0.24 \times 10^{-5}$	3.25	This work
$Y_{41}$	$-0.3310 \times 10^{-5}$	$0.98 \times 10^{-7}$	2.97	This work
$Y_{02}$	$-0.2723 \times 10^{-5}$	$0.41 \times 10^{-7}$	1.52	This work
$Y_{12}$	$-0.1089 \times 10^{-6}$	$0.57 \times 10^{-8}$	5.18	This work
$D^e$	6370	1.0	0.015	This work [24]-theory
$DRMSD = 0.44$		-----	-----	This work

In order to test the consistency among some of Dunham coefficients the Kratzer relation (2.45) was used. Taking value of the coefficients from table 4.1, we have:

$$Y_{02} = -0.2723 \times 10^{-5} \text{ (cm}^{-1}\text{)}, \quad -4 \frac{(Y_{01})^3}{(Y_{10})^2} = -0.2757 \times 10^{-5} \text{ (cm}^{-1}\text{)}.$$

These numerical values give a relative deviation about 1.24 % that reveals a fairly regular Morse-like shape of the potential in the investigated region (and only in this region).

It is interesting to compare spectroscopic constants obtained within the current work with those found by theoretical calculations [24] and in previous experimental work [18]. Comparison with the theoretical calculation gives:

$$\begin{aligned} \Delta T_e &= 58 \text{ cm}^{-1}. \\ \Delta \omega_e &= 2.57 \text{ cm}^{-1}. \\ \Delta B_e &= 5 \times 10^{-4} \text{ cm}^{-1}. \\ \Delta R_e &= 0.004 \text{ \AA}. \\ \Delta D^e &= 17 \text{ cm}^{-1}. \end{aligned}$$

Such deviations are usually considered as “very good overall agreement” but one should notice that current experimental accuracy is much higher, since it is of the order of  $0.1 \text{ cm}^{-1}$ .

When we compare present experimental molecular constants with results of previous ones we see also some differences. This is not surprising since, as was already notice, first experimental data [18] consist of only 20 spectral lines.

### 4.3.3 Potential energy curve

As predicted in [24], the  $4^1\Sigma^+$  state of NaLi has a double-minimum potential well due to the non-crossing rule for the states having identical symmetry. The barrier between two minima is  $28423 \text{ cm}^{-1}$  relative to the bottom of the PEC of ground electronic state, what means it is much higher than the last observed presently level  $v' = 11$  and we can assume that all energy levels observed in this work are placed in the inner well of the potential curve.

In order to construct a potential curve of the  $4^1\Sigma^+$  state which is capable to reproduce current experimental data, we employed the IPA method. At the beginning we generated a trial potential by using the experimental potential obtained in the previous work [18] but extended to both sides to ensure proper boundary conditions for solving the RSE. The extended parts for the potential were taken from the theoretical ones [24] but

shifted upwards by  $47 \text{ cm}^{-1}$  to connect smoothly with the potential from [18]. The entire trial potential was then interpolated in a grid of 30 equidistant-points ranging from  $2.1 \text{ \AA}$  to  $6.45 \text{ \AA}$  of internuclear distances. Iterations of the IPA procedure were terminated when the consecutive corrections to the potential were below  $10^{-5} \text{ cm}^{-1}$ . The final IPA potential (table 4.2) reproduced our experimental level energies with a  $DRMSD = 0.21$ .

**Table 4.2.** The rotationless point-wise IPA potential of the  $4^1\Sigma^+$  state of NaLi.

$R [\text{\AA}]$	$U [\text{cm}^{-1}]$	$R [\text{\AA}]$	$U [\text{cm}^{-1}]$	$R [\text{\AA}]$	$U [\text{cm}^{-1}]$
2.10	36028.361181	3.60	26613.971557	5.10	28368.393889
2.25	33307.743156	3.75	26780.504126	5.25	28428.234127
2.40	31049.246273	3.90	26975.230241	5.40	28482.726575
2.55	29377.252365	4.05	27178.334441	5.55	28511.787670
2.70	28186.567614	4.20	27379.581888	5.70	28506.322465
2.85	27376.650797	4.35	27574.539359	5.85	28462.651012
3.00	26864.721248	4.50	27761.180278	6.00	28428.233722
3.15	26584.444191	4.65	27935.656450	6.15	28395.525247
3.30	26478.968000	4.80	28094.134947	6.30	28359.921696
3.45	26502.548474	4.95	28225.148963	6.45	28335.409946

$DRMSD = 0.21$

In figure 4.4, we plotted the IPA potential (the solid circles) and the theoretical one (the solid line) from [24]. It revealed a good consistency between the two curves in the inner well region. We also plotted a curve of energy difference between our IPA potential and the experimental potential obtained in the previous work [18]. It is apparent to see that in the potential region of  $2.8 \div 4.7 \text{ \AA}$ , which was covered by the previous experimental data, the discrepancies between curves are not bigger than  $0.3 \text{ cm}^{-1}$ . Such deviation could be explained by the fact the current IPA potential based on the data consisting of 190 spectral lines while the previous one based on only 20 spectral lines.

According to the theoretical calculations in [24], the bottom of the inner well was predicted about  $2000\text{ cm}^{-1}$  to the barrier, what means that current experimental data cover 83% of the inner well, or cover 27 % of the entire potential depth.

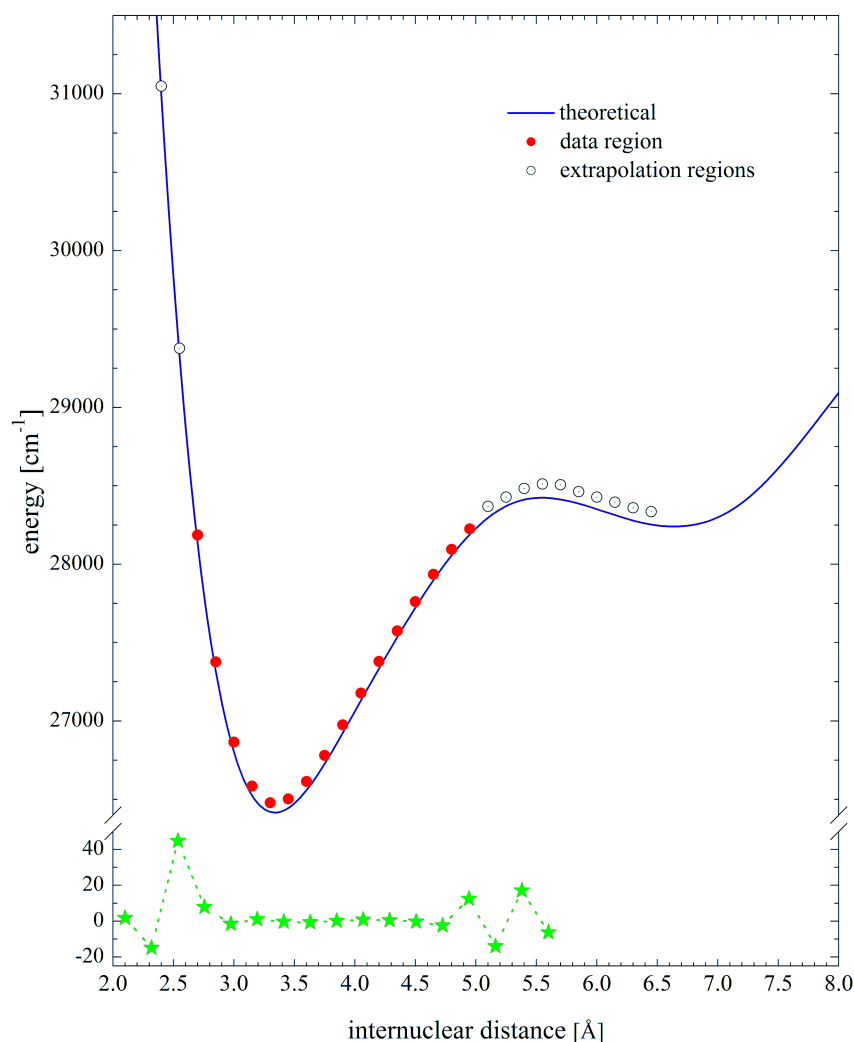


**Figure 4.4.**

Upper part: the solid curve represents the theoretical PEC for the  $4^1\Sigma^+$  state calculated in [24], the solid-circle represents the IPA potential curve in the region covered by experimental data, and the open circles represent the extrapolation of the IPA potential. Bottom: the dot-star represents difference in energy scale between the current IPA potential and the previous one [18].

In summary, we derived a potential curve of the  $4^1\Sigma^+$  state of the NaLi molecule which allows to reproduce with high accuracy energies of 12 vibrational levels in the inner potential well for a broad range of rotational quantum numbers ( $J = 9 - 46$ ). However, with the present experimental scheme employing transitions from thermally populated levels in the ground state, we were not able to access into the outer potential well, neither that above the barrier, and therefore investigation of them would require a different experimental technique.

## 4.4. The $3^1\Pi$ state

### 4.4.1 Observation and assignment of the spectra

The  $3^1\Pi$  state was observed by means of the PLS technique. The wavenumbers of probe light beam was selectively chosen to excite the transitions via  $1^1\Pi \leftarrow 1^1\Sigma^+$  and  $2^1\Sigma^+ \leftarrow 1^1\Sigma^+$  bands (list of the probe transitions is presented in table 3.5).

The pump light was delivered by parametric oscillator/ amplifier system (OPO/OPA, Sunlite EX, Continuum) provided with a frequency doubler (FX-1) and pumped with the third harmonic of an injection seeded Nd:YAG laser (Powerlite 8000). The pump laser system was scanned over a spectral energy range  $29600 - 32300 \text{ cm}^{-1}$  and its light was polarized either linearly or circularly. With linear polarization we observed PLS spectrum of the  $3^1\Pi$  state consisting of P, Q and R lines, whereas only P and R lines occurred in the circular polarization (see tables 3.1 and 3.3). Such appearances are illustrated in figure 4.5, where we show a part of PLS spectrum of the  $3^1\Pi \leftarrow 1^1\Sigma^+$  transitions probed with  $496.4 \text{ nm}$  probe-laser line which excites the  $1^1\Pi(1, 29) \leftarrow 1^1\Sigma^+(0, 30)$  transition for both polarizations.

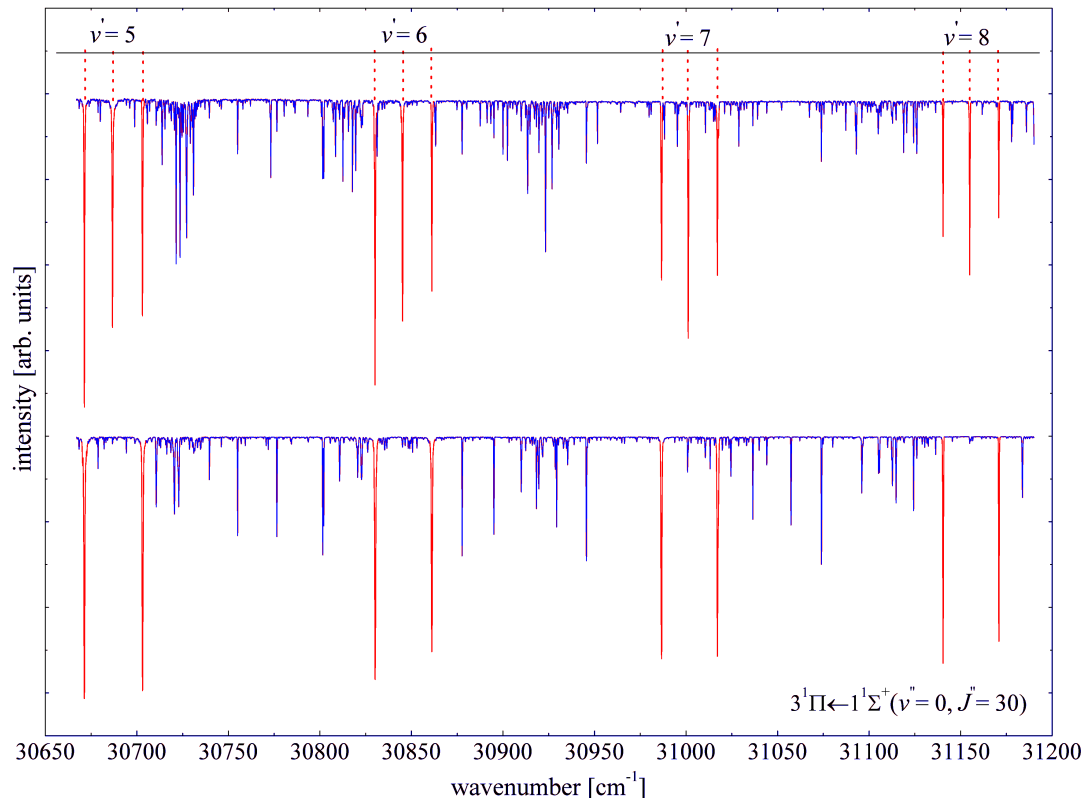


**Figure 4.5.** A part of the PLS spectrum of the  $3^1\Pi \leftarrow 1^1\Sigma^+$  band system observed in cases of linearly (upper) and circularly (lower) polarized pumping light. In both cases the probe line is set at  $496.5 \text{ nm}$ , thus labels level  $(0, 30)$  of the ground  $1^1\Sigma^+$  state.

The rotational quantum numbers of the observed spectral lines can be determined by taking in to account selection rules (2.71) for change of rotational quantum number.

Assignment of vibrational quantum number was more complicated. Particularly identification of lines terminating at  $v = 0$  level in the upper state was necessary in order to assign vibrational quantum numbers to all observed levels in that state. Initially, we assumed that the lowest observed levels was  $v = 0$ . This assignment was confirmed at a later stage of the analysis by comparison of the Franck–Condon factors with the observed relative intensities of spectral lines in the following way.

The wavenumbers of these pre-assigned spectral lines were fitted to the relation:

$$\bar{\nu} = T'(v', J') - T''(v'', J'') + \Delta T(v', J'). \quad (4.7)$$

Here, the  $\Delta T(v', J')$ -term describes the  $\Lambda$ -doubling in the  $3^1\Pi$  state, which is given by

$$\Delta T(v', J') = \delta \left[ \sum_{k=1} \sum_{l=0} q_{kl} (v + \frac{1}{2})^k [J(J+1) - 1]^l \right], \quad (4.8)$$

where  $\delta = 0$  for  $f$ -levels which give rise to  $Q$  lines and  $\delta = 1$  for  $e$ -levels which give rise to  $P$  and  $R$  lines. The spectroscopic term values in (4.7) are determined with the Dunham expansion:

$$T(v, J) = T_e + \sum_k \sum_l Y_{kl} (v + \frac{1}{2})^k [J(J+1) - 1]^l. \quad (4.9)$$

The obtained Dunham coefficients were used to build an RKR potential and then to calculate the Franck-Condon (FC) factors for these transitions. In the next step we compared the envelope-function of the calculated FC factors with the corresponding intensity distribution of vibrational transitions. Such comparison allowed us to check the correctness of the pre-assignment of vibrational quantum numbers. In figure 4.6, we showed a comparison between the observed intensity distribution and the corresponding FC factors (and its envelope function) in the case of labelled (1, 25) level. In this case envelope function has a node at  $v' = 4$  for which spectral lines were not observed what confirms  $v$ -assignment.

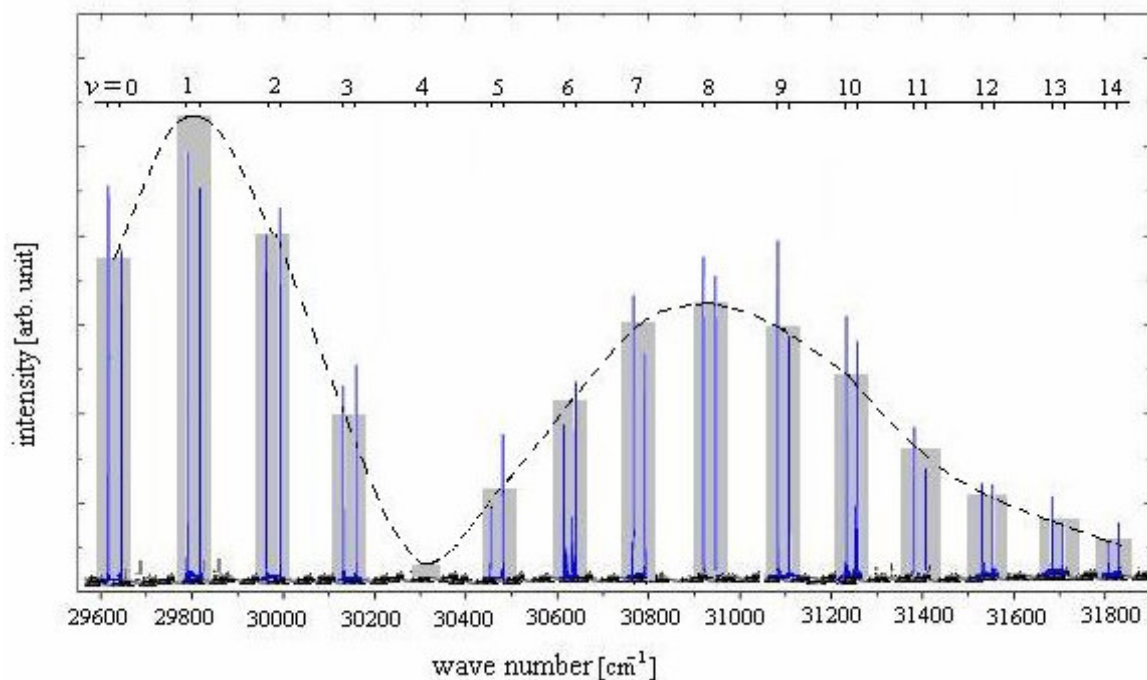


**Figure 4.6.** The envelope function (dashed) of the square of the calculated FCFs (grey bar) and intensity distribution of the observed spectral lines when labelling level was (1, 25).

Once the assignment of the quantum numbers for the chosen progression had been established the preliminary Dunham coefficients were used to find spectral lines of other vibrational progressions. Finally we identified 10 vibrational progressions consisting of 380 transitions in the  $3^1\Pi \leftarrow 1^1\Sigma^+$  band system. Distribution of the experimental data in the field of the rotational and vibrational quantum numbers in the  $3^1\Pi$  is plotted in figure 4.7.

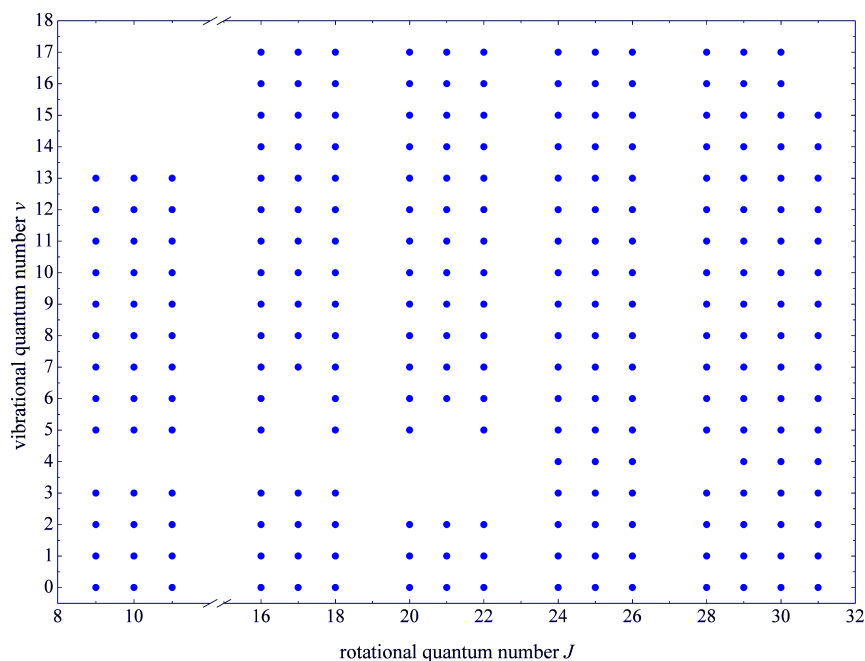


**Figure 4.7.** Distribution of the experimental data in the field of rotational and vibrational quantum numbers of the  $3^1\Pi$  state in NaLi.

#### 4.4.2 Dunham coefficients

Dunham coefficients of  $3^1\Pi$  state were derived by fitting the wavenumbers of spectral transitions to expressions (4.7) ÷ (4.9), where the set of Dunham coefficients of the ground state was taken from [15] and then fixed during the fit. By analysing the deviations between the calculated and observed wavenumbers for different numbers of fitted Dunham coefficients we found that some of transitions in the spectra exhibited local perturbations, especially in vibrational bands of  $v' = 1, 2$  (for  $P$ - and/or  $R$ - lines). The strongly perturbed lines shift from the predicted positions by 0.3- 1.5  $\text{cm}^{-1}$ , and therefore were eliminated from the final fit. Finally we obtained an optimum set of Dunham coefficients describing 360 lines with  $DRMSD = 0.746$ . The calculated electronic energy was 29981.601  $\text{cm}^{-1}$  with an uncertainty of 0.036 $\text{cm}^{-1}$ . Using this electronic energy we calculated the dissociation energy for the  $3^1\Pi$  state as presented in 4.1.2. The uncertainty of the calculated dissociation energy was 1  $\text{cm}^{-1}$  which was mainly due to the uncertainty in determination of the dissociation energy for the ground state [15]. Final list of the Dunham coefficients is presented in table 4.3.

**Table 4.3.** Dunham coefficients,  $T_e$  and  $D_e$  of the  $3^1\Pi$  state of NaLi.

Coefficient	Value [ $\text{cm}^{-1}$ ]	Uncertainty [ $\text{cm}^{-1}$ ]	Error (%)
$T_e$	29981.60	0.036	$1.2 \times 10^{-4}$
$Y_{10}$	178.803	0.020	0.011
$Y_{20}$	-1.6727	0.0042	0.249
$Y_{30}$	0.02577	0.00035	1.325
$Y_{40}$	$-0.1685 \times 10^{-3}$	$0.96 \times 10^{-5}$	5.369
$Y_{01}$	0.281429	$0.80 \times 10^{-4}$	0.029
$Y_{11}$	$-0.3715 \times 10^{-2}$	$0.13 \times 10^{-4}$	0.346
$Y_{21}$	$0.4611 \times 10^{-4}$	$0.75 \times 10^{-6}$	1.638
$Y_{02}$	$-0.2935 \times 10^{-5}$	$0.62 \times 10^{-7}$	2.165
$q_{01}$	$0.388 \times 10^{-3}$	$0.14 \times 10^{-4}$	3.586
$D^e$	6296.8	1.0	0.016
$DRMSD = 0.746$			

We checked consistency among some of the Dunham coefficients by using the Kratzer relation (2.45). Taking the value of the coefficients from table 4.3, we obtained:

$$4(Y_{01})^3 / (Y_{10})^2 \approx 0.2789 \times 10^{-5} \text{ cm}^{-1},$$

what is close (within 5%) to  $Y_{02}$  and means that potential curve of  $3^1\Pi$  state has regular, close to Morse function shape (in the experimentally determined range of PEC).

Having precise value of the coefficient describing  $\Lambda$ -doubling ( $q_{01}$ ) we can try (with some approximation) to check if it is possible to determine term energy of the state responsible for  $\Lambda$ -doubling. Assuming Van Vleck's pure precession model [77] and the unique perturbation approximation [78], and assuming that  $\Lambda$ -doubling strength in the  $3^1\Pi$  state is contributed mainly from the coupling between levels of the  $3^1\Pi$  and  $6^1\Sigma^+$  states we can write for the  $\Lambda$ -doubling coefficient following formula:

$$q_{01} \approx \frac{2B^2l(l+1)}{E_{3\pi} - E_{6^1\Sigma^+}}, \quad (4.10)$$

where  $B$  is rotational constant of the  $3^1\Pi$  state,  $l$  is angular quantum number of the valence electron in the atomic state which correlates to both molecular states. Taking into account  $B = Y_{01}$ ,  $q_{01}$ ,  $E_{3^1\Pi} = T_e[3^1\Pi]$  (from Tab. 4.3),  $l = 2$  we obtained electronic energy  $T_e[6^1\Sigma^+] = 27359 \text{ cm}^{-1}$ . This value is definitely too low compared with the predicted  $29313 \text{ cm}^{-1}$  [24] what shows that the assumed approximations is inadequate. In fact, the Van Vleck's pure precession approximation of the  $\Lambda$ -doubling requires several approximations [61] like : unique perturber, identical shape of potential curves, each state described by a single configuration which are weakly fulfilled in case of the  $3^1\Pi$  state: e.g. the potential shape of the perturbing state ( $6^1\Sigma^+$ ) has not the same shape [24]. Therefore, more sophisticated treatment is needed in order to explain the value of lambda-doubling coefficient determined experimentally for the  $3^1\Pi$ .

### 4.4.3 Potential energy curve

#### RKR potential

In order to construct potential energy curve of the  $3^1\Pi$  state, first we employed the semi-classical RKR method. The molecular constants from table 4.3 were used to generate  $G(v)$  and  $B(v)$  functions ((2.30) and (2.32)). Pairs of turning points were then calculated from (2.51a) and (2.51b). Finally we obtained an RKR potential determined with 18 pairs of the turning points and having a bottom at  $R_e \cong 3.338 \text{ \AA}$ . The turning points range from 2.5499 to 5.0118  $\text{\AA}$  and are listed in table 4.4.

In the next step we tested accuracy of the RKR potential by comparing the term values of the observed spectral lines to corresponding eigenvalues obtained by numerical solving the following RSE (with RKR potential  $U(R)$  from tab.4.4):

$$\left[ \frac{-\hbar^2}{2\mu} \frac{d^2}{dR^2} + \frac{\hbar^2}{2\mu R^2} [J(J+1)-1] + U(R) + \delta q_{01} [J(J+1)-1] \right] \chi(R) = E \chi(R). \quad (4.11)$$

Since the comparison revealed deviations whose magnitude was typically  $\pm 0.9 \text{ cm}^{-1}$  (is far beyond our experimental uncertainty), therefore we used the IPA method to construct a more reliable potential for this state.

**Table 4.4.** The RKR potential energy curve of the  $3^1\Pi$  state of NaLi.

$v$	$G(v) [\text{cm}^{-1}]$	$R_1 [\text{Å}]$	$R_2 [\text{Å}]$
-0.49992376 <sup>(*)</sup>	0.000	3.3381392 ( $R_e$ )	
0	88.973	3.1627491	3.5387561
1	264.513	3.0479296	3.7041971
2	436.935	2.9746980	3.8282442
3	606.385	2.9183373	3.9355783
4	773.006	2.8717266	4.0332828
5	936.937	2.8316347	4.1245502
6	1098.311	2.7962768	4.2111259
7	1257.258	2.7645463	4.2940758
8	1413.907	2.7357025	4.3740992
9	1568.378	2.7092215	4.4516785
10	1720.790	2.6847167	4.5271580
11	1871.256	2.6618931	4.6007906
12	2019.889	2.6405193	4.6727656
13	2166.792	2.6204095	4.7432268
14	2312.069	2.6014117	4.8122851
15	2455.817	2.5833991	4.8800265
16	2598.131	2.5662642	4.9465187
17	2739.099	2.5499149	5.0118153

\* this row corresponds to bottom of the RKR potential

### IPA potential

In order to use the IPA method, at first we generated a trial potential by using the RKR one, but extrapolated up to 2.0 and 6.0 Å to ensure proper boundary conditions for solving the RSE (4.11). The extrapolated parts for trial potential were taken from the Hulbert-Hirschfelder potential model (2.46). The entire trial potential was interpolated to determine in a grid of 41 equidistant points.

In the IPA procedure the radial Schrödinger equation was solved numerically in a step size 0.001 Å by the Numerov-Cooley method [57]. The correction for potential and correction for the  $q_{01}$ -coefficient were sought iteratively. The finally obtained IPA potential reproduced energies of our experimental levels with a  $DRMSD = 0.49$ . Points of the IPA potential and the lambda-doubling coefficient are tabulated in table 4.5.

**Table 4.5.** The point-wise IPA potential energy of the  $3^1\Pi$  state of NaLi.

$R$ [Å]	$U$ [ $\text{cm}^{-1}$ ]	$R$ [Å]	$U$ [ $\text{cm}^{-1}$ ]	$R$ [Å]	$U$ [ $\text{cm}^{-1}$ ]
2.0	41701.591219	3.4	29990.454093	4.8	32265.032716
2.1	39324.148561	3.5	30039.575884	4.9	32467.272127
2.2	37272.360939	3.6	30124.867699	5.0	32717.698934
2.3	35650.796585	3.7	30238.888707	5.1	32840.684973
2.4	34268.133622	3.8	30374.633383	5.2	33056.238931
2.5	33241.699084	3.9	30528.335076	5.3	33249.294449
2.6	32323.263583	4.0	30695.236683	5.4	33431.697644
2.7	31617.540852	4.1	30872.776916	5.5	33608.645015
2.8	31065.943718	4.2	31057.390442	5.6	33857.447897
2.9	30653.441615	4.3	31248.605633	5.7	34050.273246
3.0	30355.701417	4.4	31444.242611	5.8	34243.451584
3.1	30156.495158	4.5	31643.633666	5.9	34437.203861
3.2	30036.700949	4.6	31846.962592	6.0	34632.059192
3.3	29986.654561	4.7	32053.418937		$q_{01} = 0.382 \times 10^{-3} \text{ cm}^{-1}$

$DRMSD = 0.49$

### Morse-Long-Range potential

In addition to the numerical IPA potential, we used a Morse-Long-Range (MLR) function and the DPotFit technique to construct an analytical potential energy curve of the  $3^1\Pi$  state. The motivation for making this approach was to find smooth, analytical connection of the well-defined experimentally potential (for  $R = 2.5 - 5$  Å) with long-range

curve described by (2.53), where  $C_n$  coefficients are taken from theory [49]. We expected that analytical representation of the PEC should be the same as the IPA PEC in the region of experimental data but also should be able to describe long-range behaviour of the PEC. As presented in [58], the analytical form of MLR function is represented by:

$$U_{MLR}(R) = D^e \left\{ 1 - \left( \frac{R_e}{R} \right)^n \left[ \frac{1 + \mathcal{R}_{m,n} / R^{m-n}}{1 + \mathcal{R}_{m,n} / R_e^{m-n}} \right] \exp[-\Phi(R) \cdot y_p(R, R_e)] \right\}^2, \quad (4.12)$$

where  $y_p$  is the radial expansion variable given by

$$y_p(R_e, R) = \frac{R^p - R_e^p}{R^p + R_e^p}, \quad (4.13)$$

and

$$\mathcal{R}_{m,n} = C_m / C_n \quad (4.14)$$

is the ratio between the dispersion coefficients  $C_m$  and  $C_n$ , and function  $\Phi(R)$  is a power expansion of  $y_p$  with the set of coefficients  $\phi(k)$ :

$$\Phi(R) = \sum_{k=0}^{NS} \phi(k) [y_p(R_e, R)]^k \quad \text{for } R \leq R_e, \quad (4.15)$$

$$\Phi(R) = \sum_{k=0}^{NL} \phi(k) [y_p(R_e, R)]^k \quad \text{for } R > R_e, \quad (4.16)$$

where  $NS$  and  $NL$  are integer numbers to be determined in the DPotFit procedure.

In order to use DPotFit technique, first we generated MLR trial function by fitting expression (4.12) to the RKR potential from table 4.4. We took value of  $C_6$  and  $C_8$  coefficients from theoretical calculations [49]. Since the MLR function changes from one set of  $\{p, NS, NL\}$  to the other and it was difficult *a priori* to guess the best one, we therefore generated the trial MLR function with several combinations of  $\{p, NS, NL\}$ . For each combination the DPotFit procedure sought optimum value for the expansion coefficients  $\phi(k)$  minimizing deviations between the experimental term values and the corresponding eigenvalues calculated from the following RSE:

$$\left[ \frac{-\hbar^2}{2\mu} \frac{d^2}{dR^2} + \frac{\hbar^2}{2\mu R^2} [J(J+1) - 1] + U_{MLR}(R) + \Delta T(R) J(J+1) \right] \chi(R) = E \chi(R), \quad (4.17)$$

where  $\Delta T(R)$  is a function representing the lambda-doubling given by

$$\Delta T(R) = \left( \frac{\hbar^2}{2\mu R^2} \right)^2 f_{\Lambda}(R), \quad (4.18)$$

where  $f_{\Lambda}(R)$  is the lambda-doubling strength function to be determined from the DPotFit. Because experimental data were far below the dissociation limit we therefore had to fix values  $D^e$ ,  $C_6$ , and  $C_8$  during fitting:  $D^e$  to the experimental value,  $C_6$ , and  $C_8$  to the theoretical ones [49]. Finally we obtained the MLR functions corresponding to the combinations of  $\{p, NS, NL\}$ .

In the next step we analyzing *DRMSD* obtained for each fit in order to choice the best values for set of  $\{p, NS, NL\}$ , in the following way (described in [58]). For the  $3^1\Pi$  state, an adequate long-range potential is described by:

$$U_{MLR}(R) \xrightarrow{R \rightarrow \infty} D^e - \left[ \frac{C_6}{R^6} + \frac{C_8}{R^8} \right] = D^e - \frac{1}{R^6} \left[ C_6 + \frac{C_8}{R^2} \right]. \quad (4.19)$$

Looking at the last transformation in (4.19) the  $R^6[D^e - U_{MLR}(R)]$  curve versus  $1/R^2$  should approach (for  $R \rightarrow \infty$ ) an intercept of value of  $C_6$  with a slope value given by  $C_8$ . In figure 4.8 we plotted corresponding curves for various combinations of parameters  $\{p, NS, NL\}$ . From the figure we found that the MLR potential has proper long-range behaviour ( $C_6$  and  $C_8$  for  $1/R^2 \rightarrow 0$ ) for  $p = 4$ . On the other hand, by analysing of *DRMSD* in DPotFit procedure we found that the best fit was obtained for  $NS = 5$  and  $NL = 7$  (*DRMSD* = 0.756). Therefore as an optimum set of  $\{p, NS, NL\}$  was found  $\{4, 5, 7\}$ . The obtained values of the expansion coefficients  $\{\phi(k)\}$  of the MLR potential for this case are listed in table 4.6. The final MLR potential and the lambda-doubling strength function are plotted in figures 4.9 and 4.10, respectively.

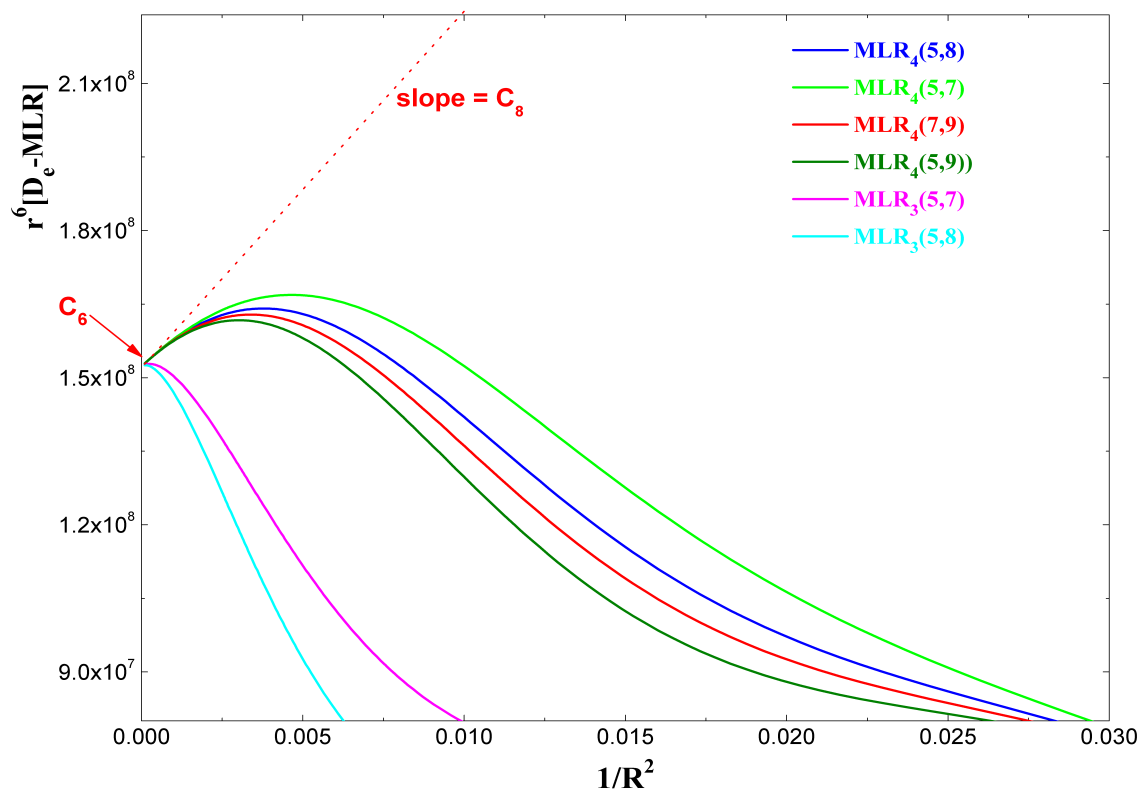


**Figure 4.8.** Plot of  $R^6[D^e - U_{MLR}(R)]$  function versus  $1/R^2$  for different combinations of  $\{p, NS, NL\}$  parameters in the MLR potential function.

**Table 4.6.** The parameters of MLR  $\{4, 5, 7\}$  potential for the  $3^1\Pi$  state of NaLi.

Parameter	Value	Uncertainty	Error (%)
$D^e$ [ $\text{cm}^{-1}$ ]	6296.72	-----	-----
$C_6$ [ $\text{cm}^{-1} \cdot \text{\AA}^6$ ]	$1.5229 \times 10^8$	-----	-----
$C_8$ [ $\text{cm}^{-1} \cdot \text{\AA}^8$ ]	$6.2003 \times 10^9$	-----	-----
$R_e$ [ $\text{\AA}$ ]	3.338943738	$1.6 \times 10^{-3}$	0.048
$\phi(0)$	-2.71837	$9.6 \times 10^{-4}$	0.035
$\phi(1)$	1.225	$1.0 \times 10^{-2}$	0.81
$\phi(2)$	0.151	$2.1 \times 10^{-2}$	13.9
$\phi(3)$	0.955	$7.6 \times 10^{-2}$	7.96
$\phi(4)$	2.25	$1.7 \times 10^{-1}$	7.56
$\phi(5)$	2.39	$3.6 \times 10^{-1}$	15.06
$\phi(6)$	-23.5	1.6	6.8
$\phi(7)$	27.4	1.3	4.74
$DRMSD = 0.756$			

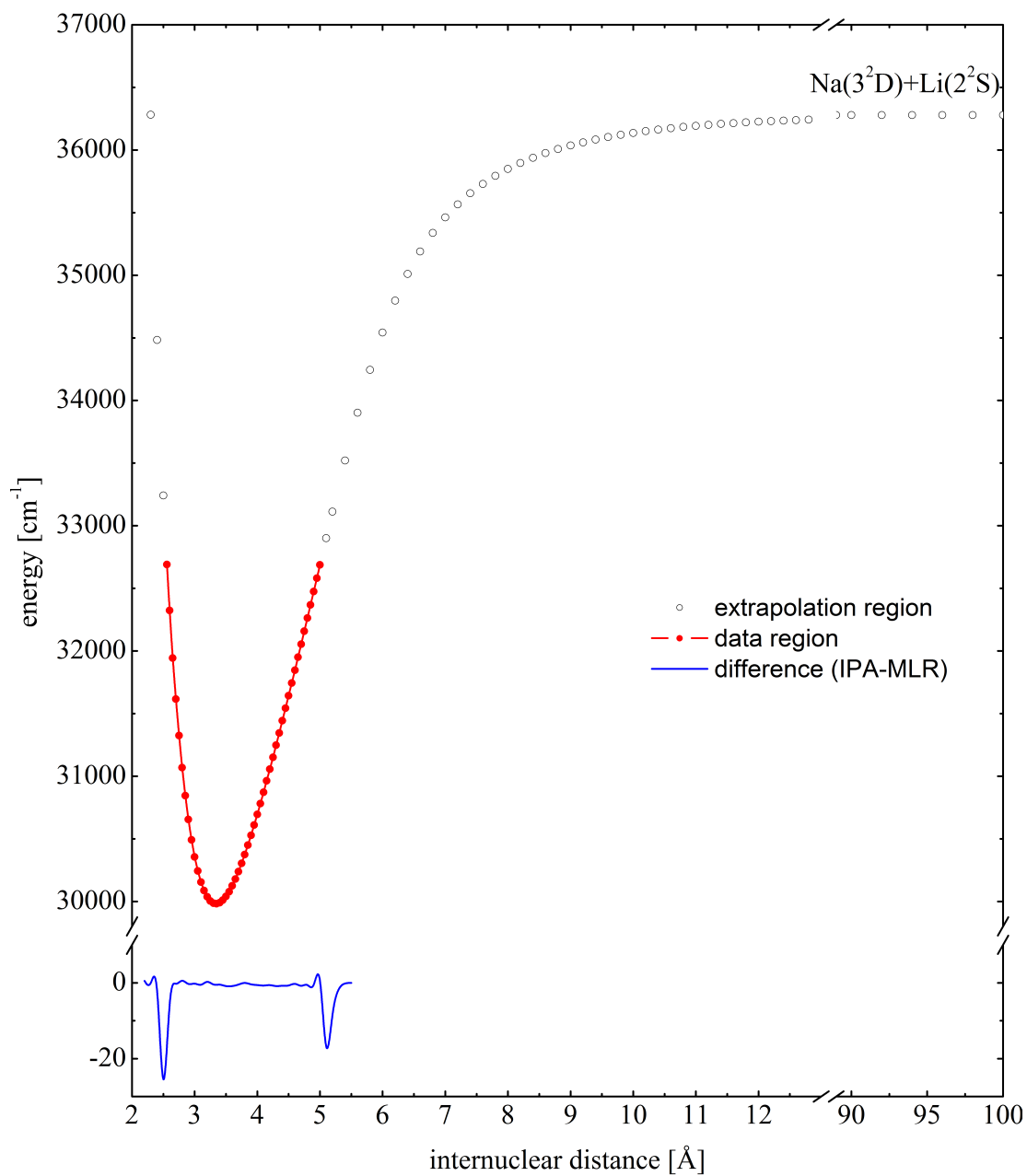


**Figure 4.9.** The analytical MLR{4, 5, 7} potential of the  $3^1\Pi$  state of NaLi (red) and the difference between the IPA and MLR{4, 5, 7} potentials (blue).

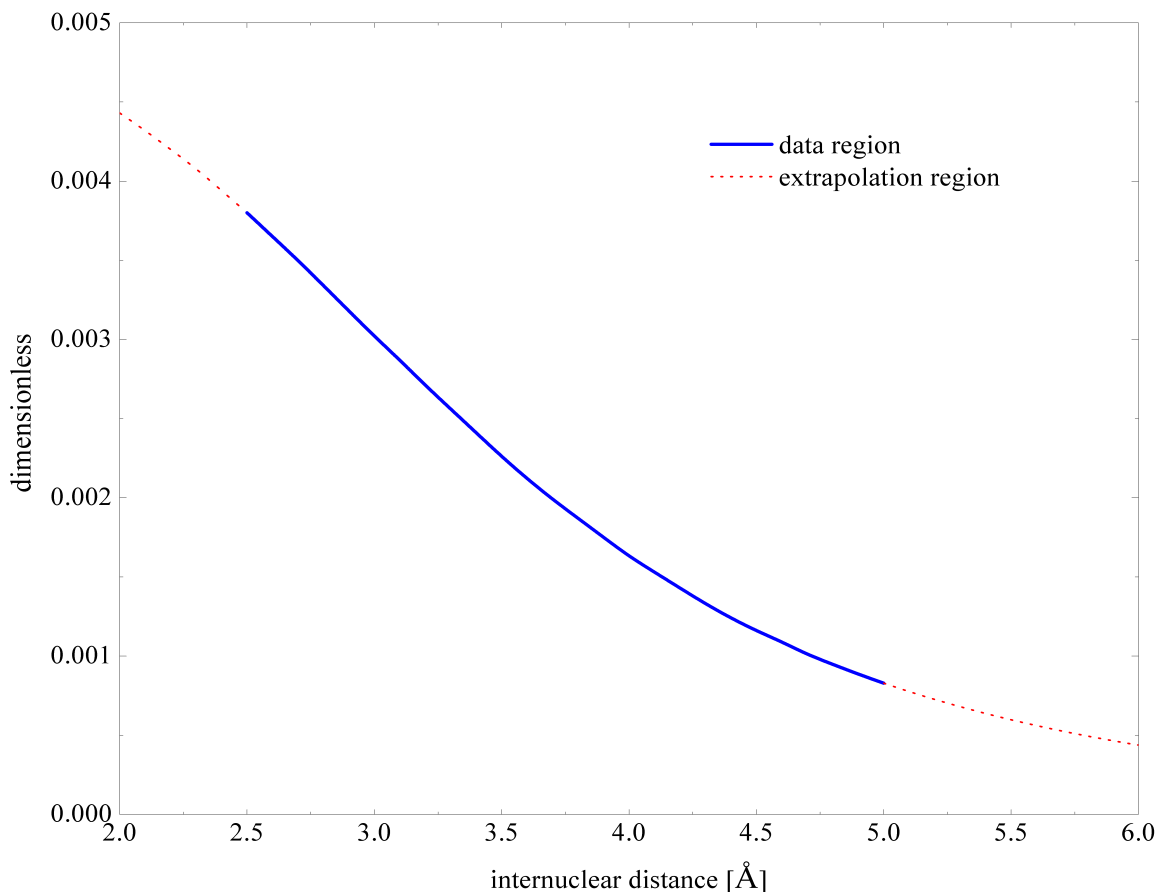


**Figure 4.10.** Lambda-doubling strength function of the  $3^1\Pi$  state.

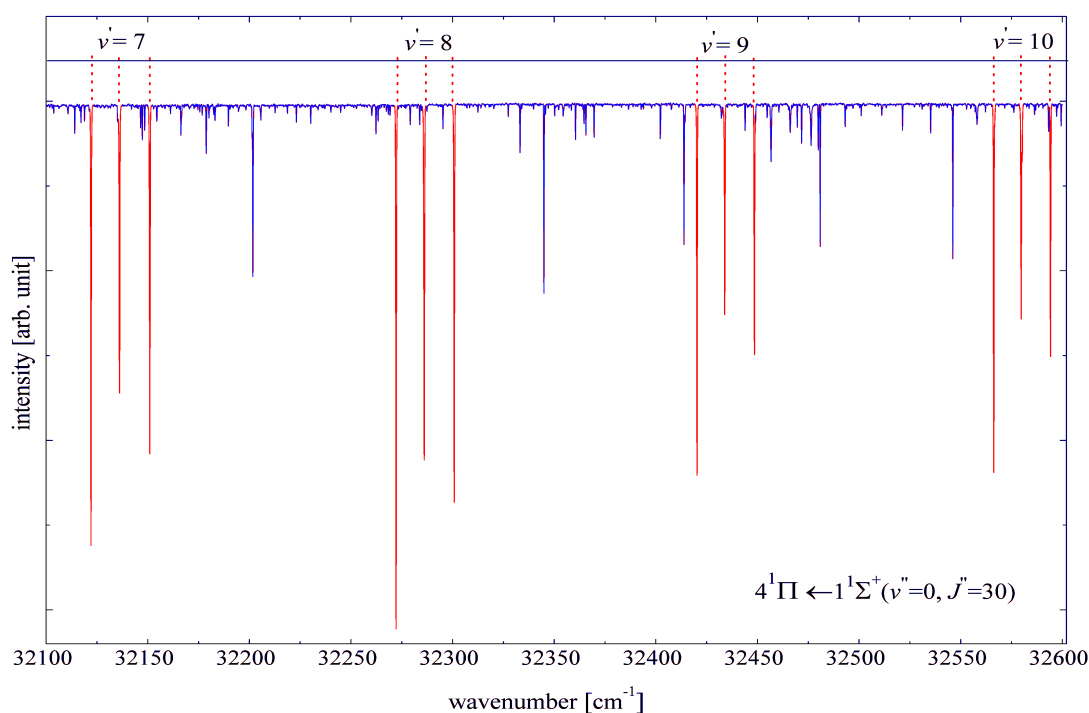
Since last theoretical calculations [79] (which appeared after presented analysis was done) predict irregular shape of the curve around  $R = 6.3 \text{ \AA}$ , so described below analytical potential is definitely not applicable in the intermediate range of  $R$  (around anti-crossing point). So we would rather consider this situation as a pronounced example that we can not infer about the shape of PEC outside the region well-represented with the experimental data.

Finally we compared the MLR potential with the IPA PEC. The comparison showed that in the region covered by experimental data the agreement between two curves is better than  $0.1 \text{ cm}^{-1}$  (see fig 4.9). Therefore one can conclude that though both potentials were constructed in different ways, nevertheless were able to reproduce experimental data within the experimental uncertainty. Analytical MLR PEC has the long-range part consistent with assumed expansion coefficients, however it should be greatly stressed that in the range around anti-crossing point MLR PEC has not physical meaning.

## 4.5. The $4^1\Pi$ state

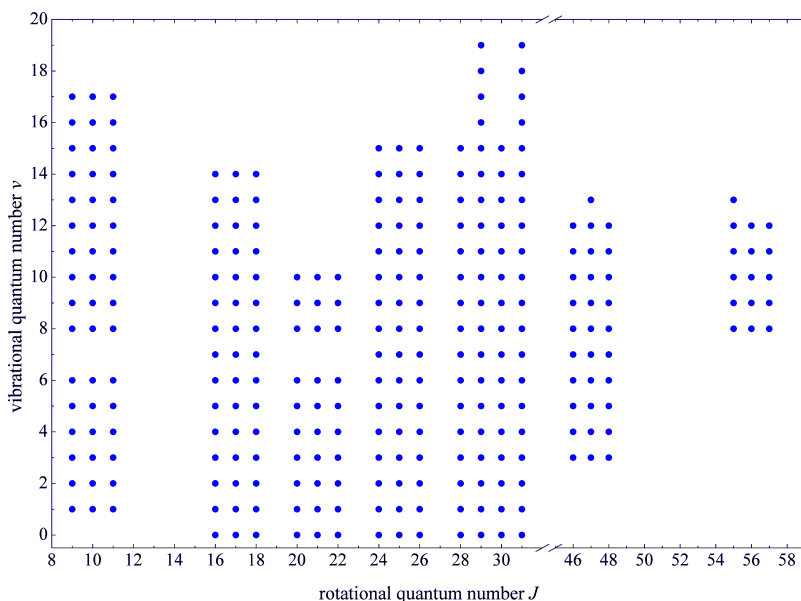
### 4.5.1 Observation and assignment of the spectra

Spectra of the  $4^1\Pi$  state were observed in spectral range  $30700 - 33900 \text{ cm}^{-1}$  with various labelled levels presented in table 3.5. In our experiments, polarization of the pump light was set linearly in order to enrich experimental data (occurrence of Q branches together with  $P$  and  $R$  ones). In figure 4.11, we show a part of polarization spectrum observed in case of  $496.5 \text{ nm}$  probe laser line, which labels level  $(0, 30)$  in the ground state.



**Figure 4.11.** A part of PLS spectrum consists of  $P$ -,  $Q$ -, and  $R$ -lines of the  $4^1\Pi \leftarrow 1^1\Sigma^+$  band in NaLi, observed for linearly polarized pump beam. The  $496.5 \text{ nm}$  probe laser line was used.

In total we observed 12 vibrational progressions consisting of 418 spectral lines. Vibrational quantum numbers for these progressions were determined by comparison between the relative intensity distribution of spectral lines and the calculated FC factors, in a similar way as was done before for the  $3^1\Pi$  state. We finally identified the quantum numbers of all spectral lines, ranging in  $v' = 0 - 19$  and  $J' = 9 - 57$ . Distribution of the experimental data in the field of rotational and vibrational quantum numbers of the  $4^1\Pi$  state is shown in figure 4.12.

**Figure 4.12.**

Distribution of the experimental data in the field of quantum numbers of the  $4^1\Pi$  state in NaLi.

### 4.5.2 Dunham coefficients

In order to derive molecular constants for the  $4^1\Pi$  state, wavenumbers of the spectral lines were fitted to relation (4.7), where the lambda-doubling and term values were represented by (4.8) and (4.9), respectively. The set of Dunham coefficients of the ground state was taken from [15] and fixed during the fit. We finally obtained an optimum set of Dunham coefficients (listed in table 4.7) with corresponding  $DRMSD = 0.62$ . The electronic energy of the  $4^1\Pi$  state was calculated to be  $31178.958\text{cm}^{-1}$ .

**Table 4.7.** Molecular constants of the  $4^1\Pi$  state of NaLi.

Coefficient	Value [ $\text{cm}^{-1}$ ]	Uncertainty [ $\text{cm}^{-1}$ ]	Error (%)
$T_e$	31 178.96	0.024	
$Y_{10}$	169.230	0.014	0.008
$Y_{20}$	-1.1203	0.0029	0.26
$Y_{30}$	$0.767 \times 10^{-2}$	$0.24 \times 10^{-3}$	3.13
$Y_{40}$	$-0.2329 \times 10^{-3}$	$0.67 \times 10^{-5}$	2.88
$Y_{01}$	0.259530	$0.27 \times 10^{-4}$	0.01
$Y_{11}$	$-0.24824 \times 10^{-2}$	$0.71 \times 10^{-5}$	0.29
$Y_{21}$	$-0.414 \times 10^{-5}$	$0.39 \times 10^{-6}$	9.4
$Y_{02}$	$-0.23349 \times 10^{-5}$	$0.55 \times 10^{-8}$	0.24
$q_{01}$	$0.2433 \times 10^{-3}$	$0.61 \times 10^{-5}$	2.51
$D^e$	6193.5 Na( $4^2P_{1/2}$ )	1.0	
	6199.1 Na( $4^2P_{3/2}$ )	1.0	
$DRMSD = 0.62$			

As presented in sect.4.1.2, the  $4^1\Pi$  state dissociates to Li( $2^2S$ ) and Na( $4^2P$ ) atomic states, thus we can determine its dissociation energy by using (4.2a). However because the Na ( $4^2P$ ) atomic state split into two fine structure components ( $4^2P_{1/2}$  and  $4^2P_{3/2}$ ) spaced apart by  $6\text{ cm}^{-1}$  and theoretical calculations do not predict which one is correlated to  $4^1\Pi$  therefore we determined the dissociation energy according to these two possible asymptotes. Both calculated dissociation energies are listed in table 4.7.

The consistency among some of Dunham coefficients was tested with the Kratzer relation,  $Y_{02} = -4(Y_{01})^3 / (Y_{10})^2$ . Taking value of the coefficients from table 4.7 we obtained  $4(Y_{01})^3 / (Y_{10})^2 \approx -0.24416 \times 10^{-5} \text{ cm}^{-1}$ . This leads to a relative deviation from  $Y_{02}$  of about 4.47% which indicates that the potential is close to regular in the data region. But on the other hand recent theoretical calculations showed the anti-crossing with  $3^1\Pi$  which deform both PECs, however it occurs outside the region investigated experimentally.

### 4.5.3 Potential energy curve

#### RKR potential

In order to construct the potential energy curve for the  $4^1\Pi$  state first we used the RKR technique. We took molecular constants from table 4.7 to generate the expressions for  $G(v)$  and  $B(v)$ , given by equations (2.30) and (2.32). The pairs of turning points were then calculated accordingly to (2.51a) and (2.51b). Finally we obtained a RKR potential determined in range  $2.61\text{-}5.31\text{ \AA}$  of the internuclear distance listed in table 4.8.

In the next step we tested accuracy of the RKR potential by comparing the experimental level energies with the corresponding eigenvalues obtained by numerical solving of the RSE (Eq. 4.11) with the RKR potential. The comparison revealed a discrepancy of about  $1\text{ cm}^{-1}$  which is beyond our experimental uncertainty. We therefore used the IPA method to construct a more reliable potential curve.

**Table 4.8.** The RKR potential of the  $4^1\Pi$  state of NaLi.

$v$	$G(v)$ [ $\text{cm}^{-1}$ ]	$R_1$ [ $\text{\AA}$ ]	$R_2$ [ $\text{\AA}$ ]
-0.49993978 <sup>(*)</sup>	0.000	3.4761171 ( $R_e$ )	
0	84.326	3.2939898	3.6800588
1	251.339	3.1728517	3.8452480
2	416.174	3.0949457	3.9677685
3	578.865	3.0347549	4.0731419
4	739.442	2.9848986	4.1687557
5	897.928	2.9420129	4.2579826
6	1054.343	2.9042295	4.3427024
7	1208.697	2.8703833	4.4240943
8	1360.998	2.8396884	4.5029611
9	1511.247	2.8115845	4.5798832
10	1659.441	2.7856536	4.6553018
11	1805.568	2.7615736	4.7295664
12	1949.614	2.7390884	4.8029639
13	2091.558	2.7179892	4.8757385
14	2231.373	2.6981026	4.9481037
15	2369.027	2.6792810	5.0202523
16	2504.482	2.6613967	5.0923630
17	2637.694	2.6443374	5.1646055
18	2768.615	2.6280026	5.2371446
19	2897.190	2.6123007	5.3101439

### IPA potential

For the convenience we chose the RKR potential as the trial one for using IPA method. However, for having proper boundary conditions when solving the RSE (4.11) in the IPA procedure we extrapolated the RKR potential on both sides (to 2.1 and 6.3  $\text{\AA}$ ) by smooth connection with the Hulbert-Hirschfelder potential (2.46). The entire trial potential curve was then interpolated to determine in grid of 0.1  $\text{\AA}$ .

After several IPA iterations, corrections for trial potential and lambda-doubling coefficient  $q_{01}$  were converged then the IPA procedure was completed. The new lambda-doubling coefficient was found to be  $0.2410 \times 10^{-3} \text{ cm}^{-1}$  that is slightly different from the original value  $0.2433 \times 10^{-3} \text{ cm}^{-1}$ . The final IPA potential (table 4.9) reproduced the experimental level energies with  $DRMSD = 0.45$ .

\* this row corresponds to bottom of the RKR potential

**Table 4.9.** The point-wise IPA potential of the  $4^1\Pi$  state of NaLi.

$R$ [Å]	$U(R)$ [cm <sup>-1</sup> ]	$R$ [Å]	$U(R)$ [cm <sup>-1</sup> ]	$R$ [Å]	$U(R)$ [cm <sup>-1</sup> ]
2.1	41479.882079	3.6	31211.801127	5.1	33700.815601
2.2	39453.853450	3.7	31279.752084	5.2	33880.731090
2.3	37749.738712	3.8	31378.226171	5.3	34057.588397
2.4	36325.097739	3.9	31501.554723	5.4	34235.302805
2.5	35142.788140	4.0	31644.658190	5.5	34404.306938
2.6	34166.886860	4.1	31803.723797	5.6	34567.302164
2.7	33393.761119	4.2	31974.971660	5.7	34724.379844
2.8	32750.793204	4.3	32155.735608	5.8	34875.483484
2.9	32248.845284	4.4	32343.079154	5.9	35020.555048
3.0	31863.316898	4.5	32535.276102	6.0	35159.574616
3.1	31580.185573	4.6	32730.964384	6.1	35292.560809
3.2	31382.107334	4.7	32927.520812	6.2	35419.565278
3.3	31257.080047	4.8	33124.231695	6.3	35540.668040
3.4	31192.828038	4.9	33318.979429	$q_{01} = 0.2410 \times 10^{-3} \text{ cm}^{-1}$	
3.5	31180.530195	5.0	33510.649440		

$DRMSD = 0.45$

From analysis of experimental data we found that the current data covered 51% of potential well depth, which correspond to region 2.61-5.31Å of internuclear distance. The IPA potential was plotted in figure 4.13, where solid-circles stand for the experimental data region. It should be noted that the extrapolation points in the IPA potential were just introduced to ensure proper boundary conditions when solving the RSE in the IPA procedure.

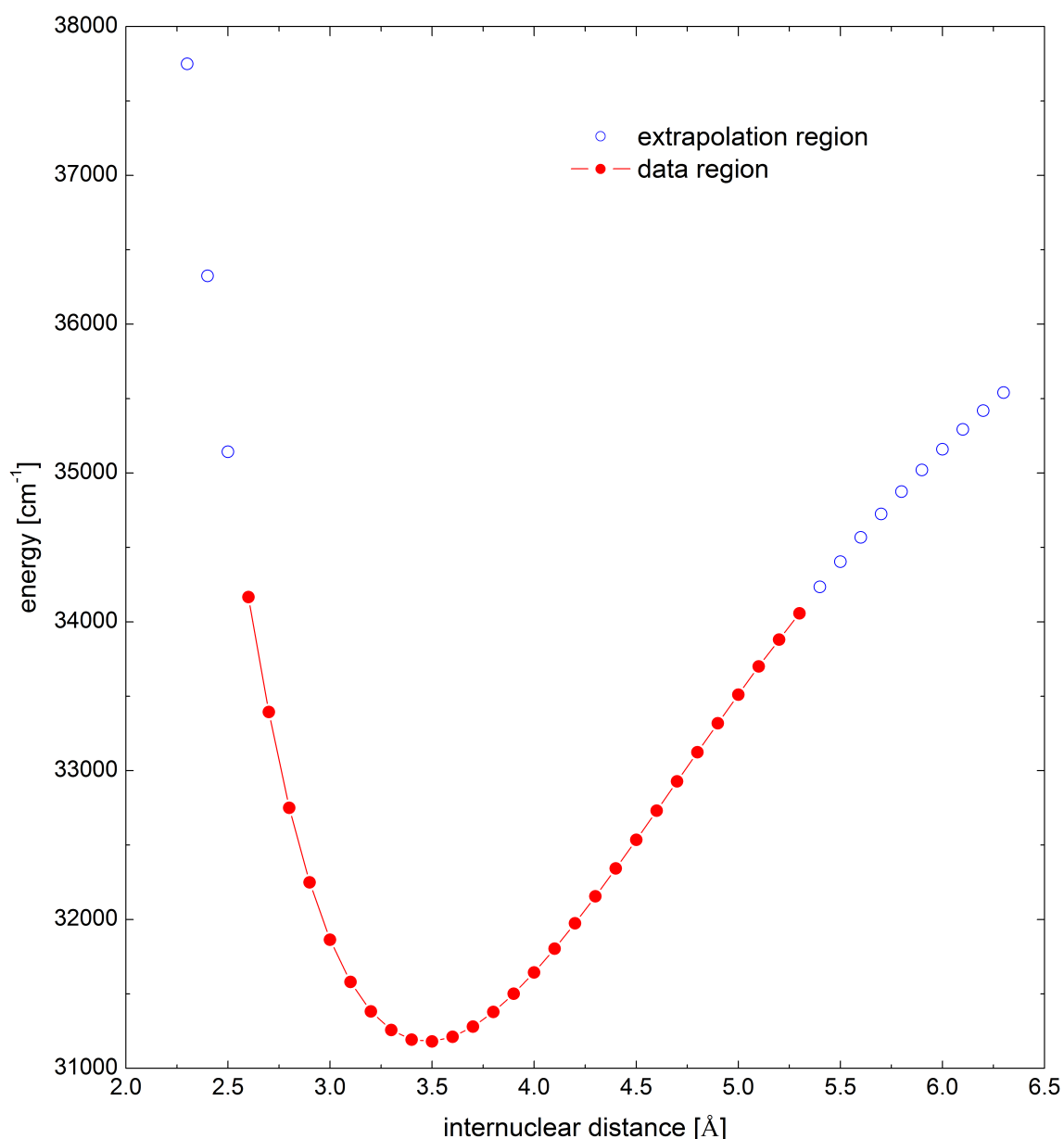


**Figure 4.13.** The IPA potential of the  $4^1\Pi$  state of NaLi, the red-solid circles stand for region covered by experimental data, and the blue circles stand for extrapolation region.

## 4.6. The $6^1\Pi$ and $7^1\Pi$ states

### 4.6.1 Observation and assignment of the spectra

We observed spectra of the two  $^1\Pi$ -symmetry states above the  $4^1\Pi$  in spectral range 33500 - 36400 cm<sup>-1</sup>. Comparison of salient molecular constants with recent theoretical calculations [79] indicates assignment of these states as  $6^1\Pi$  and  $7^1\Pi$ , however such assignment means that  $5^1\Pi$  was missed out on observations. Another possible

interpretation in the light of new theoretical calculations [79] is presented and discussed in section 4.7

We determined vibrational quantum numbers for observed spectra by comparison between the intensity distribution of the observed spectral lines and the calculated FC factors for each progression, by the same way as it was done before for the  $3^1\Pi$  and  $4^1\Pi$  states. In figure 4.14, we showed a part of the PLS spectrum involving transitions to the  $6^1\Pi$  and  $7^1\Pi$  states in the case of  $15539.3\text{ cm}^{-1}$  probe laser line which labels the level  $(v'', J'') = (0, 22)$  in the ground state.

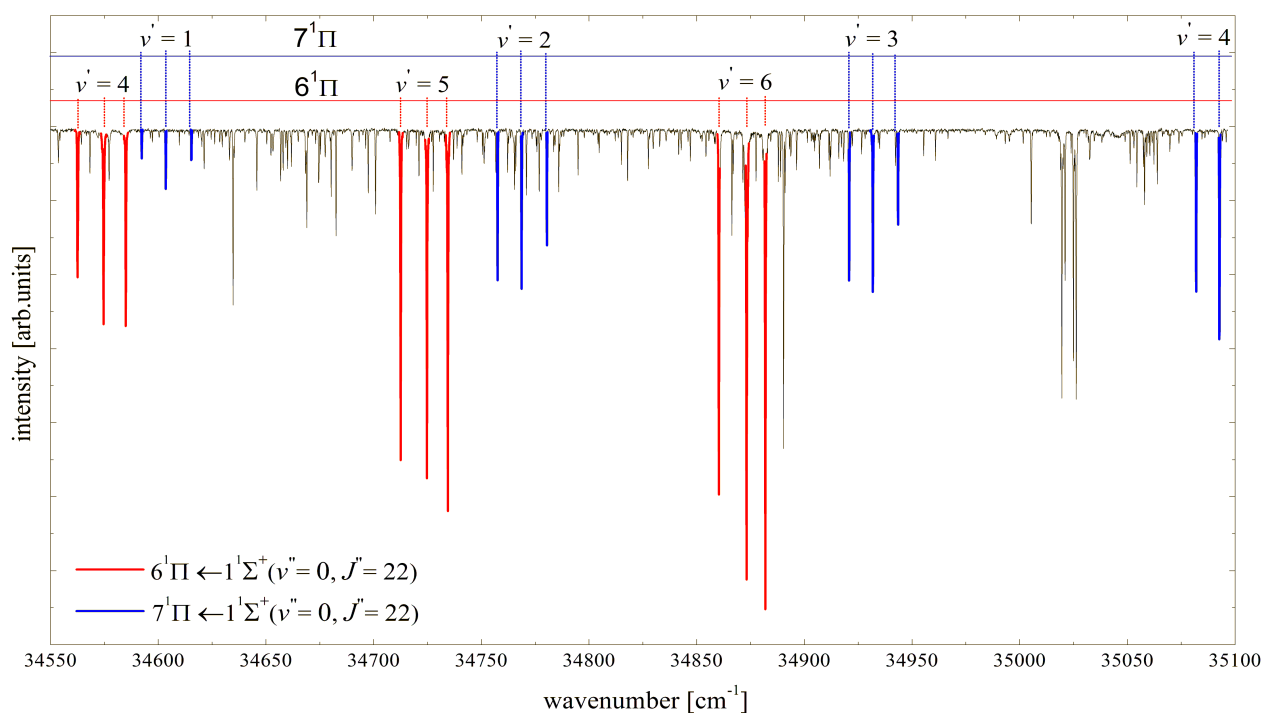


**Figure 4.14.** Part of the PLS spectrum of the  $6^1\Pi \leftarrow 1^1\Sigma^+$  band (red) and  $7^1\Pi \leftarrow 1^1\Sigma^+$  (blue) observed in the case of linearly polarized pump beam and with the probe laser at  $15539.3\text{ cm}^{-1}$ . The labelled level in this case is  $(v'', J'') = (0, 22)$ . The vibrational quantum numbers of the progressions are indicated.

In total we identified 200 transitions belonging to the  $6^1\Pi \leftarrow 1^1\Sigma^+$  band, and 196 to the  $7^1\Pi \leftarrow 1^1\Sigma^+$  band system. Quantum numbers of the observed levels span the range of  $v' = 0 - 6$ , and  $J' = 9 - 31$  in case of the  $6^1\Pi$  state and  $v' = 0 - 8$ ,  $J' = 9 - 31$  for  $7^1\Pi$  state. Distributions of the experimental data are shown in figs 4.15 and 4.16.

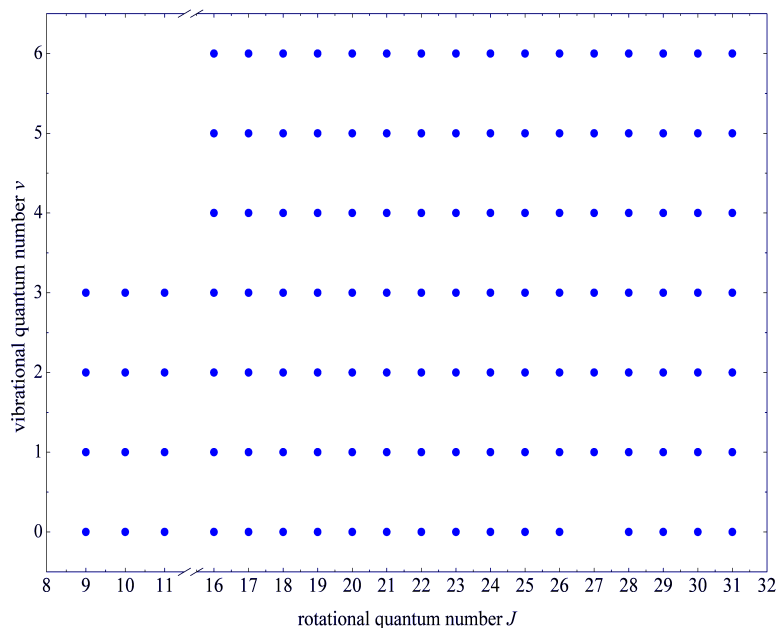


**Figure 4.15.** Distribution of the experimental data in the field of rotational and vibrational quantum numbers for the  $6^1\Pi$  state.

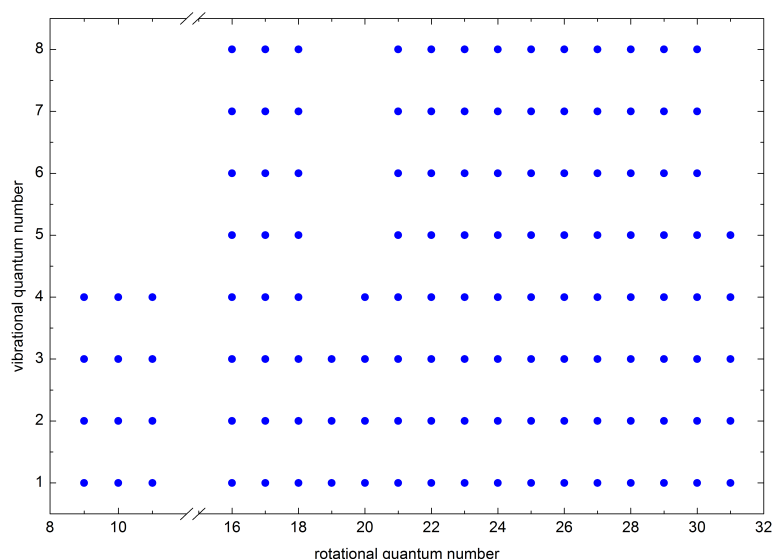


**Figure 4.16.** Distribution of the experimental data in the field of rotational and vibrational quantum numbers for the  $7^1\Pi$  state

#### 4.6.2 Dunham coefficients

Dunham coefficients of the  $6^1\Pi$  and  $7^1\Pi$  states were determined by fitting wavenumbers of all spectral lines to relation (4.7). The fitting procedure for the  $6^1\Pi$  and  $7^1\Pi$  states was similar to that done for the  $3^1\Pi$  state before, however in case of  $6^1\Pi$  state, we encountered a different, unusual situation. In order to find the set of Dunham coefficients describing observed lines we had to take in to account  $v$ -dependence of the lambda-doubling. Therefore, for the  $6^1\Pi$  state the expansion (4.8) was retained up to third term ( $q_{21}$ ). Finally we obtained optimum sets of Dunham coefficients for the  $6^1\Pi$  and  $7^1\Pi$

states, tabulated in 4.10. The determined values for dissociation energies of the  $6^1\Pi$  and  $7^1\Pi$  states have the uncertainty of  $1\text{ cm}^{-1}$  due to the uncertainty in determination of the dissociation energy for the ground state [15].

**Table 4.10.** Molecular constants of the  $6^1\Pi$  and  $7^1\Pi$  states of NaLi.

Coefficient	$6^1\Pi$ state			$7^1\Pi$ state		
	Value	Uncertainty	Error (%)	Value	Uncertainty	Error (%)
$T_e$ [ $\text{cm}^{-1}$ ]	34042.28	0.04	$9\times 10^{-5}$	34535.82	0.037	0.0
$D^e$ [ $\text{cm}^{-1}$ ]	4346	1.0	$2.3\times 10^{-4}$	4429	1.0	$2.2\times 10^{-4}$
$Y_{10}$ [ $\text{cm}^{-1}$ ]	168.990	0.03	0.018	170.497	0.024	0.014
$Y_{20}$ [ $\text{cm}^{-1}$ ]	-2.2559	0.0084	37	-0.9399	$0.58\times 10^{-2}$	0.62
$Y_{30}$ [ $\text{cm}^{-1}$ ]	$0.7397\times 10^{-1}$	$0.76\times 10^{-3}$	0.1	$-0.1285\times 10^{-1}$	$0.42\times 10^{-3}$	3.29
$Y_{01}$ [ $\text{cm}^{-1}$ ]	0.27163	0.00011	0.04	0.2634501	$0.917\times 10^{-4}$	0.035
$Y_{11}$ [ $\text{cm}^{-1}$ ]	$-0.4648\times 10^{-2}$	$0.50\times 10^{-4}$	1.07	$-0.2722\times 10^{-2}$	$0.93\times 10^{-5}$	0.34
$Y_{21}$ [ $\text{cm}^{-1}$ ]	$0.1165\times 10^{-3}$	$0.68\times 10^{-5}$	5.8	-----	-----	-----
$Y_{02}$ [ $\text{cm}^{-1}$ ]	$-0.2347\times 10^{-5}$	$0.76\times 10^{-7}$	3.2	$-0.2492\times 10^{-5}$	$0.8\times 10^{-7}$	3.2
$q_{01}$ [ $\text{cm}^{-1}$ ]	$-0.5972\times 10^{-2}$	$0.58\times 10^{-4}$	0.97	$-0.24122\times 10^{-3}$	$0.164\times 10^{-4}$	6.82
$q_{11}$ [ $\text{cm}^{-1}$ ]	$0.2107\times 10^{-2}$	$0.36\times 10^{-4}$	1.7	-----	-----	-----
$q_{21}$ [ $\text{cm}^{-1}$ ]	$-0.2888\times 10^{-3}$	$0.48\times 10^{-5}$	1.66	-----	-----	-----
	<i>DRMSD</i> = 0.56			<i>DRMSD</i> = 0.66		

### 4.6.3 Potential energy curves

#### RKR potentials

The RKR method was used to construct potential curves for the  $6^1\Pi$  and  $7^1\Pi$ . First we used molecular constants from table 4.10 to generate the vibrational and rotational functions (relations (2.30) and (2.32)), and then calculated turning points by integration of (2.51a) and (2.51b). Finally we obtained RKR potentials for the  $6^1\Pi$  and  $7^1\Pi$  states. The RKR potential of the  $6^1\Pi$  state was determined in seven pairs of turning points ranging from 2.85 to 4.32 Å. The RKR for the  $7^1\Pi$  state was determined in eight pairs of turning points ranging from 2.82 to 4.48 Å. Details of these RKR potentials are listed in table 4.11.

In next step we tested accuracy of the RKR potentials by comparing experimental level energies to the corresponding eigenvalues of the following RSE (with the RKR potentials):

$$\left[ \frac{-\hbar^2}{2\mu} \frac{d^2}{dR^2} + \frac{\hbar^2}{2\mu R^2} [J(J+1) - 1] + U(R) + \delta \sum_{k=0} q_{k1} (v + \frac{1}{2})^k [J(J+1)] \right] \chi = E\chi. \quad (4.21)$$

In (4.21)  $\delta = 0$  for  $f$ -parity levels,  $\delta = 1$  for  $e$ -parity levels,  $k = 0$  for the  $7^1\Pi$  state, and  $k = 0, 1$  and  $2$  for the  $6^1\Pi$ . Our comparison revealed deviations are of about  $1.7 \text{ cm}^{-1}$  for the  $6^1\Pi$  state, and  $0.7 \text{ cm}^{-1}$  for the  $7^1\Pi$  state. Such deviations were too large; therefore we used the IPA technique to construct more confident potentials which are capable of representing the data within the experimental uncertainty.

**Table 4.11.** The RKR potentials of the  $6^1\Pi$  and  $7^1\Pi$  states of NaLi.

$6^1\Pi$				$7^1\Pi$			
$v$	$G(v)/\text{cm}^{-1}$	$R_1 [\text{\AA}]$	$R_2 [\text{\AA}]$	$v$	$G(v)/\text{cm}^{-1}$	$R_1 [\text{\AA}]$	$R_2 [\text{\AA}]$
-0.49976	0.000	3.3978289 ( $R_e$ )		-0.500349	0.000	3.4501610 ( $R_e$ )	
0	83.899	3.2193073	3.6066316	0	85.072	3.2691518	3.6537746
1	248.617	3.1041591	3.7821414	1	253.647	3.1496179	3.8188589
2	409.489	3.0312572	3.9150026	2	420.228	3.0731104	3.9414105
3	566.959	2.9753835	4.0302608	3	584.735	3.0141592	4.0469361
4	721.471	2.9293466	4.1349217	4	747.093	2.9653751	4.1428632
5	873.468	2.8899259	4.2320092	5	907.223	2.9233806	4.2326103
6	1023.394	2.8553708	4.3230687	6	1065.050	2.8862944	4.3181020
				7	1220.495	2.8529395	4.4005614
				8	1373.482	2.8225199	4.4808338

### IPA potentials

In the IPA method we used the RKR potential but extrapolated on both sides up to 2.3 and 5.2  $\text{\AA}$  for the  $6^1\Pi$  state, and up to 2.2 and 5.7  $\text{\AA}$  for the  $7^1\Pi$  as the trial ones. The extrapolations were performed with Hulbert-Hirschfelder potential (2.46) connected smoothly with the RKR potentials. Each potential was then interpolated in grid of 0.1  $\text{\AA}$ .

In the IPA procedure lambda-doubling coefficients  $q_{01}$  were fitted in the case of both states whereas the values of the coefficients  $q_{11}$  and  $q_{21}$  for  $v$ -dependent lambda-doubling in the  $6^1\Pi$  state were fixed to the value obtained from former analysis. The final IPA potentials could reproduce the experimental level energies with  $DRMSD = 0.53$  for the

$6^1\Pi$  state and with  $DRMSD = 0.45$  for the  $7^1\Pi$  state. Details of these potentials are tabulated in tables 4.12 and 4.13.

**Table 4.12.** The point-wise IPA potential of the  $6^1\Pi$  state of NaLi.

$R$ [Å]	$U(R)$ [cm <sup>-1</sup> ]	$R$ [Å]	$U(R)$ [cm <sup>-1</sup> ]	$R$ [Å]	$U(R)$ [cm <sup>-1</sup> ]
2.3	40133.328902	3.4	34041.025103	4.5	35425.358757
2.4	38745.026620	3.5	34066.083430	4.6	35621.494849
2.5	37597.801196	3.6	34120.704594	4.7	35820.960096
2.6	36668.069206	3.7	34209.911801	4.8	36022.172710
2.7	35925.441133	3.8	34310.312763	4.9	36222.916609
2.8	35345.978618	3.9	34440.336109	5.0	36420.638447
2.9	34868.939503	4.0	34561.265147	5.1	36612.613058
3.0	34522.519597	4.1	34730.338976	5.2	36796.448900
3.1	34297.894253	4.2	34848.356054	$q_{01} = -0.5907 \times 10^{-2}$	
3.2	34142.629495	4.3	35044.324286	$q_{11} = 0.2107 \times 10^{-2}$	
3.3	34066.872671	4.4	35232.582679	$q_{21} = -0.2888 \times 10^{-3}$	
$DRMSD = 0.53$					

**Table 4.13.** The point-wise IPA potential of the  $7^1\Pi$  state of NaLi.

$R$ [Å]	$U(R)$ [cm <sup>-1</sup> ]	$R$ [Å]	$U(R)$ [cm <sup>-1</sup> ]	$R$ [Å]	$U(R)$ [cm <sup>-1</sup> ]
2.2	42773.090325	3.4	34542.432452	4.6	36138.867581
2.3	41050.412540	3.5	34541.055600	4.7	36335.564236
2.4	39618.450139	3.6	34582.265169	4.8	36528.672430
2.5	38426.894848	3.7	34658.558468	4.9	36718.513403
2.6	37451.543624	3.8	34764.033784	5.0	36888.187407
2.7	36662.392797	3.9	34893.875295	5.1	37048.964080
2.8	36043.749063	4.0	35042.462253	5.2	37200.853216
2.9	35549.534313	4.1	35206.256394	5.3	37343.888479
3.0	35170.186560	4.2	35381.409116	5.4	37480.373940
3.1	34896.980240	4.3	35564.799307	5.5	37610.396550
3.2	34709.360994	4.4	35752.232486	5.6	37733.503810
3.3	34595.872514	4.5	35939.528873	5.7	37849.243210
$q_{01} = 0.240242 \times 10^{-3} \text{ cm}^{-1}$					
$DRMSD = 0.45$					

Comparison between the observed spectral regions and the dissociation energy we found that the current experimental data covers 24% of the  $6^1\Pi$  potential well depth, and 32 % of the  $7^1\Pi$  potential well depth. The IPA potentials are plotted in figure 4.17.

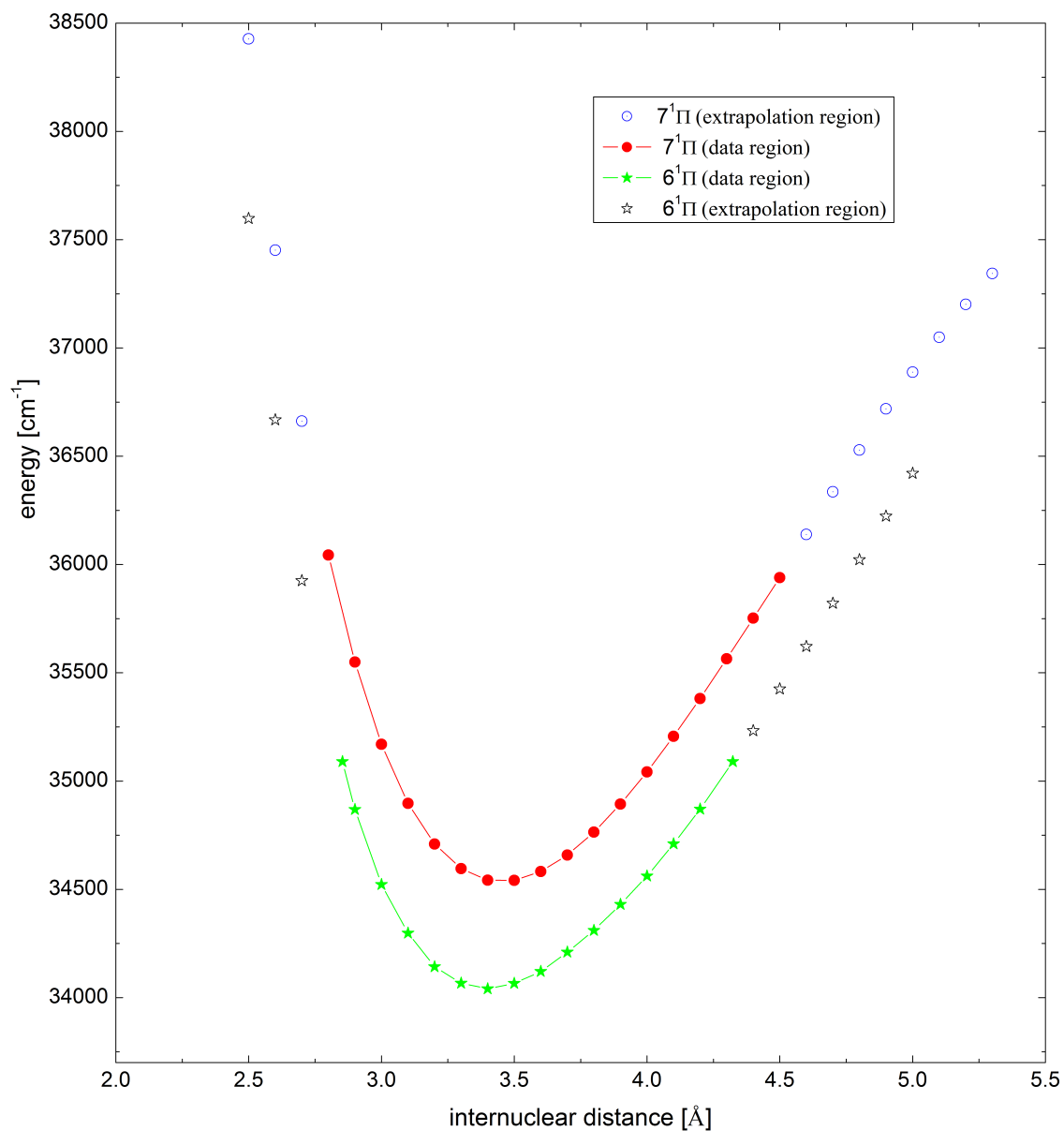


**Figure 4.17.** The IPA potential curves of the  $6^1\Pi$  and  $7^1\Pi$  states of NaLi.

#### 4.7. Comparison of the current results with recent theoretical calculations

Soon after our experimental observations for the  $7^1\Pi$  state, two independent theoretical papers with comprehensive study on electronic structure of NaLi appeared in 2008 [79, 80]. In both theoretical works the electronic structure of NaLi molecule was explored up to the Na ( $3^2P$ ) - Li ( $2^2P$ ) atomic asymptote, which correlates among others to the  $7^1\Pi$  state. The authors calculated important molecular constants (listed in table 4.14) and potential curve for each electronic state. The calculated values of molecular constants in both papers are slightly different for the low-lying states below the Na( $3^2S$ )-Li( $3^2P$ ) asymptote. However, deviations between the two theoretical results increase for higher excited states, particular for the  $7^1\Pi$  state. Considering the values of electronic energy ( $T_e$ ) and dissociation energy ( $D^e$ ) of the  $7^1\Pi$  obtained in [79] and [80], we find following energy differences between two results:  $1615\text{ cm}^{-1}$  for  $T_e$ , and  $1966\text{ cm}^{-1}$  for  $D^e$ . Obviously such differences for  $T_e$  and  $D^e$  are not acceptable and they exceed acceptable inaccuracy, and therefore one can point out the more correct (closer to experimental) theoretical calculations are necessary. Presently, having experimental results it is possible to check reliability of the two theoretical results by comparing them to the experimental ones. In table 4.14 we list the theoretical and experimental values of molecular constants for the  $4^1\Sigma^+$ ,  $3^1\Pi$ ,  $4^1\Pi$ ,  $6^1\Pi$  and  $7^1\Pi$  states.

**Table 4.14.** Theoretical and experimental molecular constants for the  $4^1\Sigma^+$ ,  $3^1\Pi$ ,  $4^1\Pi$ ,  $6^1\Pi$  and  $7^1\Pi$  states of NaLi.

Molecular constant	$4^1\Sigma^+$	$3^1\Pi$	$4^1\Pi$	$6^1\Pi$	$7^1\Pi$	Reference
$T_e$ [ $\text{cm}^{-1}$ ]	26474.19	29981.60	31178.96	34042.28	34535.82	this work
	26457	29992	31155	34027	34541	[79] - theory
	26184	29900	30904	34338	36156	[80] - theory
$\omega_e$ [ $\text{cm}^{-1}$ ]	179.673	178.804	169.325	168.990	170.497	this work
	181.86	176.74	170.33	167.74	171.35	[79] - theory
$R_e$ [ $\text{\AA}$ ]	3.3430	3.3358	3.4710	3.3978	3.4502	this work
	3.328	3.344	3.460	3.397	3.444	[79] - theory
	3.387	3.392	3.493	3.477	3.746	[80] - theory
$D^e$ [ $\text{cm}^{-1}$ ]	6370	6297	6193	4346	4429	this work
	6340	6236	6171	4321	4386	[79] - theory
	5888	6130	5646	4194	2420	[80] - theory

At first we consider the molecular constants calculated in [79] (table 4.14). Looking through these values we find good agreement between theoretical values and the experimental ones, where we find deviations:  $24 \text{ cm}^{-1}$  (for  $T_e[4^1\Pi]$ ),  $61 \text{ cm}^{-1}$  (for  $D^e[3^1\Pi]$ ,  $0.015 \text{ \AA}$  (for  $R_e[4^1\Sigma^+]$ , and  $2.1 \text{ cm}^{-1}$  (for  $\omega_e[3^1\Pi]$ ). Another way for comparison is to examine both theoretical and our IPA potentials on diagram (figure 4.18) with plot of the theoretical and experimental PECs. Such plot displays that the theoretical potential curves are very close to the experimental one (in the scale of the picture). Following [79] shape of all potential curves for the  $4^1\Sigma^+$ ,  $3^1\Pi$ ,  $4^1\Pi$ ,  $6^1\Pi$  and  $7^1\Pi$  states resulted from avoided crossings, however in all cases experimental data are placed in the regular part of the PEC and their description with Dunham constants is physically meaningful in this range.

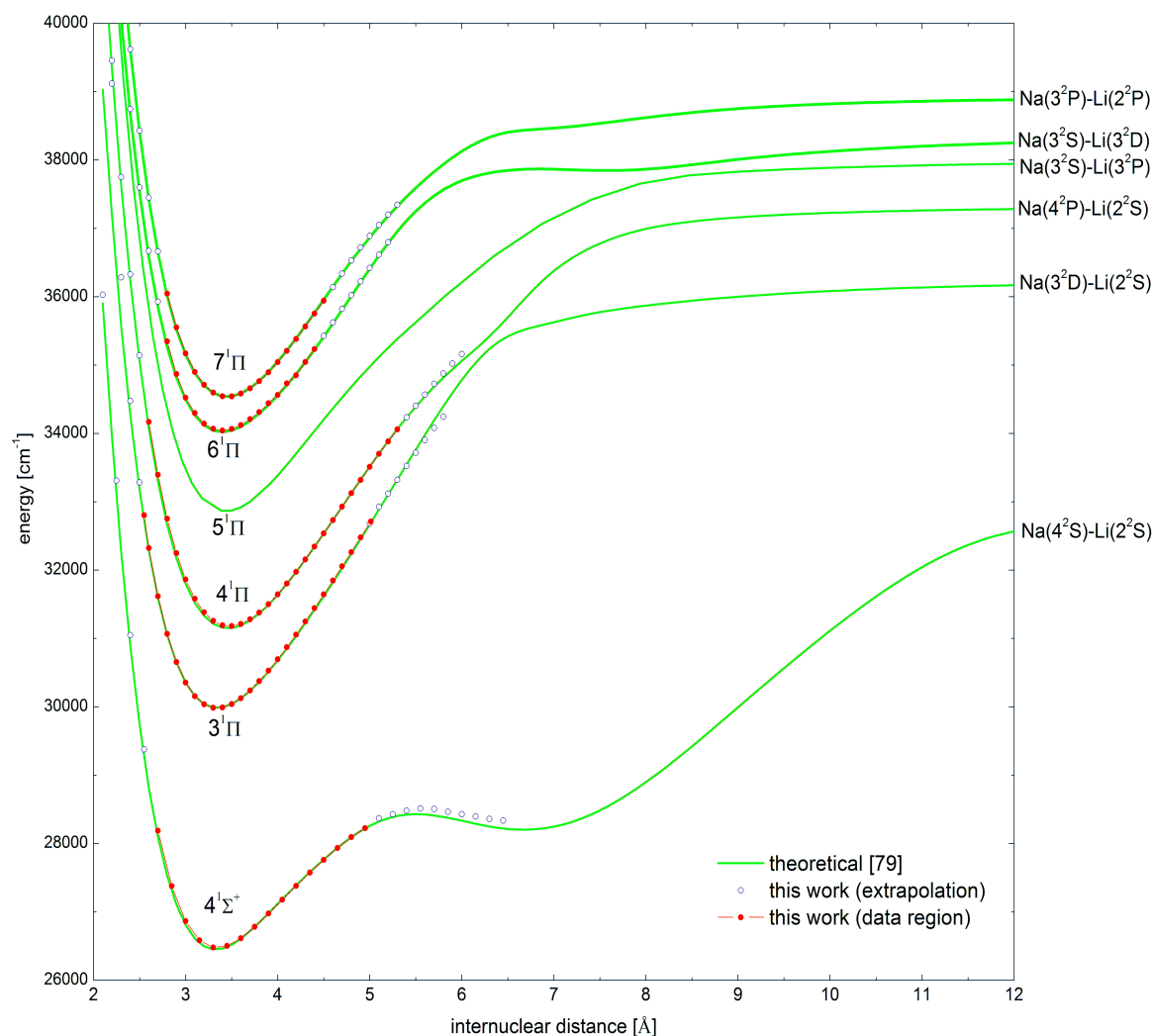


**Figure 4.18.** The potential energy curves of the  $4^1\Sigma^+$  and  $3-7^1\Pi$  states of NaLi calculated [79] (the solid curves) and in our work (the solid-circle). The  $5^1\Pi$  state has not been observed in our experiment.

The relative good agreement with the experimental results indicates the theoretical calculations for NaLi in [79] are quite reliable. However, there appears a problem due to missing of  $5^1\Pi$  from experimental observation. At the moment there is not any reasonable explanation for this but it seems that this is not an experimental fault or oversight. Recorded spectra in region that we expected to observe spectrum of the  $5^1\Pi$  were of very good quality (S/N ratio), all registered progressions were assigned to  $4^1\Pi$  and  $6^1\Pi$  states, or to  $\text{Na}_2$  spectrum which was precisely known from former measurements [30]. There were no any evidences of lines to the  $5^1\Pi$  state. One can not expect unusually small transition dipole moment of the  $5^1\Pi \leftarrow 1^1\Sigma^+$  band system; however there is not actually calculation of it. We would lean towards the suspicion that theoretical calculations are not correct for this state. On the other hand we see that this is somehow in contradiction with very good agreement for other states.

When turning to the comparison between theoretical values calculated in [80] and the experimental ones we see from table 4.14 that agreement between the theoretical and the experimental values is not good, much worse then that were for [79]. Indeed, for the  $7^1\Pi$  state we find huge deviations of  $1620\text{ cm}^{-1}$  for  $T_e$  and  $0.296\text{ \AA}$  for the equilibrium internuclear distance ( $R_e$ ). But if for the moment we would allow for a such big discrepancy one can see from fig. 4.19 that another assignment of the two highest states is possible, namely as  $5^1\Pi$  and  $6^1\Pi$ . This would solve the problem of missing  $5^1\Pi$  state, but would show up big inaccuracy of calculations, e.g. deviations for  $T_e$  and  $R_e$  in these states (with new 5-6 $^1\Pi$ -assignment) would be:  $198\text{ cm}^{-1}$  for  $T_e$  [ $6^1\Pi$ ],  $250\text{ cm}^{-1}$  for  $T_e$  [ $5^1\Pi$ ],  $0.0268\text{ \AA}$  for  $R_e$  [ $6^1\Pi$ ], and  $0.1792\text{ \AA}$  for  $R_e$  [ $5^1\Pi$ ]. The last value of deviation for  $R_e$  is quite big compared to those for other states, and it is well above that expected from nowadays theoretical calculations for alkali dimers.

At the moment, from the experimental side nothing more can be done. We hope that this intriguing situation will be explained with the help of theoreticians when they get our (still not published) results for the highest states. Looking at the comparison of all data in tab.4.14 and potential curves in figs. 4.18 ÷ 4.20 we would incline that the theoretical calculations in [79] are more reliable than of [80], however this leaves riddle of the  $5^1\Pi$  state unravelled.

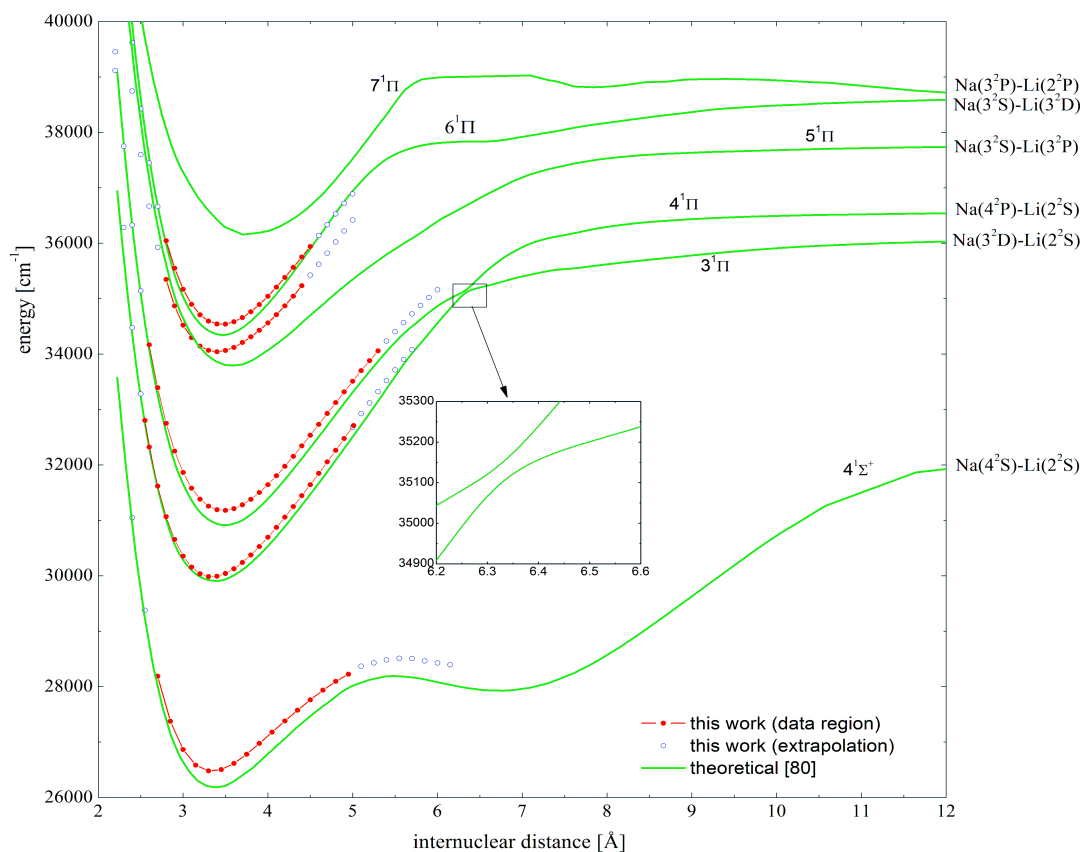


**Figure 4.19.** The theoretical potential energy curves of the  $4^1\Sigma^+$  and  $3\text{-}7^1\Pi$  states from [80] (the solid curves) and the experimental ones (the solid-circles).

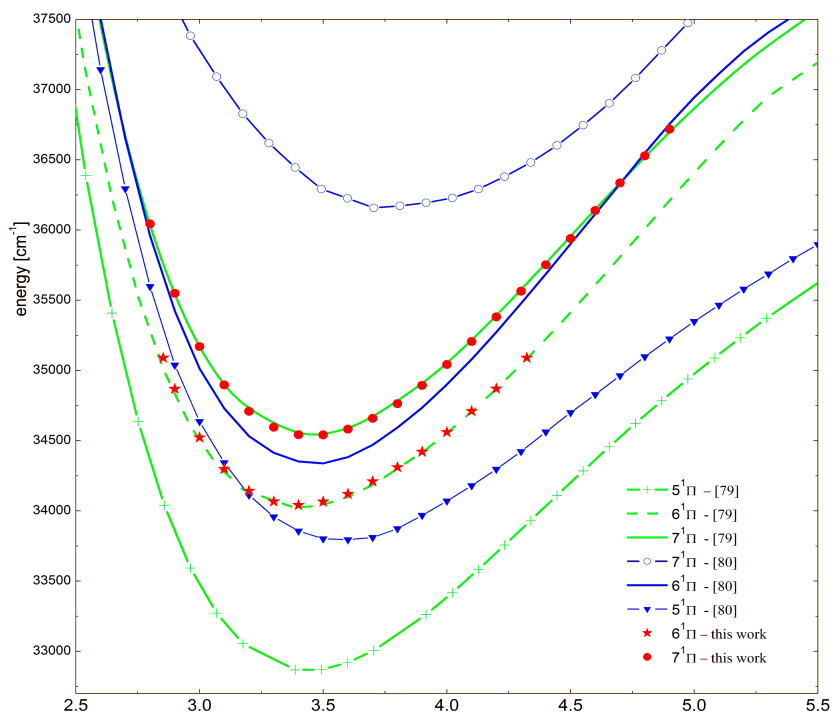


**Figure 4.20.** The theoretical potential curves of the  $5\text{-}7^1\Pi$  states in [79] and [80], and the IPA potential curves of the  $6^1\Pi$  and  $7^1\Pi$  states determined in this work.

## Chapter 5

### Summary and conclusions

Polarization labelling spectroscopy technique has been used to study the rovibrational structure of several excited electronic states of NaLi. All investigated electronic states of  ${}^1\Pi$ -symmetry were unknown (unobserved) before our measurements. There were also no theoretical calculations for them, until August 2008. Nevertheless, on the basis of the characteristic features of the observed polarisation spectra we have identified unambiguously the symmetry of each of these states, and by numerical analysis we characterised them, obtaining molecular (Dunham) constants and constructed reliable potential energy curve for each state. Besides the four  ${}^1\Pi$ -symmetry states, we also recorded transitions to the previously investigated  $4{}^1\Sigma^+$  state [18] and using the much richer current data set we could refine the existing description of this state.

Finally in the 26000-36300  $\text{cm}^{-1}$  spectral region we observed five electronic states accessible directly by optical transitions from the ground state (e.g. singlet states of  $\Sigma^+$ ,  $\Pi$ -symmetry).

The  $4{}^1\Sigma^+$  state was previously investigated by the polarization labelling spectroscopy technique [18]. In that first experiment (with the  $\text{Ar}^+$  laser used as a probe laser) only one progression was registered and molecular constants and a potential energy curve were determined only from a single vibrational progression. Within the current experiments we used the tunable dye laser as a probe laser, and could choose several probing transitions. It turned out that a more precise description of this state was possible with such complementary data. Finally we observed 200 spectral lines and then converted them into the molecular constants and to the IPA potential. According to theoretical

predictions [24, 79-80] the  $4^1\Sigma^+$  state has a double-minimum potential well due to avoided crossing with the  $5^1\Sigma^+$  state. Our analysis showed that the presently collected experimental data cover the inner well of the PEC, which was predicted to be regular. Therefore the determined molecular constants represent spectroscopic characterization of this regular part of the PEC, and only this part.

The measured spectra of the  $3^1\Pi$  and  $4^1\Pi$  states consisted of 367 and 361 lines, respectively. Analysis of the spectra revealed the presence of local perturbations affecting *P*- and/or *R*- lines to  $v = 1, 2$  vibrational levels of the  $3^1\Pi$  state. According to the calculations in the recent theoretical paper [79], the potential curves of the  $6^1\Sigma^+$  and  $3^1\Pi$  states cross each other at a point near the bottom of the potential curve of the  $3^1\Pi$  state. Therefore, we can expect such local perturbations to be mainly due to non-adiabatic couplings between the  $3^1\Pi$  and  $6^1\Sigma^+$  states. By using Dunham expansion we determined molecular constants for the  $3^1\Pi$  and  $4^1\Pi$  states. It turned out that construction of potential energy curves for the  $3^1\Pi$  and  $4^1\Pi$  states by the RKR method yielded important information (equilibrium internuclear distance, position of vibrational levels), and the RKR potentials were sufficiently accurate for comparison with theoretical ones. However in order to obtain PEC that is sufficiently precise to reproduce high resolution data the IPA technique was used to further refine these potential curves. Having the constructed IPA potentials we checked, that the experimental data for the  $3^1\Pi$  and  $4^1\Pi$  states could be reproduced to within our experimental uncertainty. Since the dispersion coefficients for the long-range potential of the  $3^1\Pi$  state were calculated theoretically [49], we tried to connect the long-range potential part of the PEC with the part covered by the experimental data. This was the motivation for the construction of a Morse-long-range (MLR) potential for the  $3^1\Pi$  state by using the DPotFit technique. However, recent predictions in [79, 80] (which appeared after this analysis was done) showed that the outer potential wall of the  $3^1\Pi$  state is deformed in the region of  $6.3 \text{ \AA}$  due to avoided-crossing with the  $4^1\Pi$  state. Therefore, in the region around the anti-crossing point we clearly cannot use regular curve description. The analytical MLR potential presented in this thesis should be considered only as a mathematical connection between the near-equilibrium part of the potential (determined by the experimental data) and the long-range part. Although the analytical MLR PEC has the long-range part consistent with assumed (real) expansion coefficients, it should be stressed that in the range around the anti-crossing point the MLR PEC has no physical meaning.

The  $6^1\Pi$  and  $7^1\Pi$  states were the highest ones studied in this work. In total, 200 spectral lines for the  $6^1\Pi$  state and 196 spectral lines for the  $7^1\Pi$  state were identified in the polarisation spectra. In case of the  $6^1\Pi$  state it turned out that strongly  $v$ -dependent lambda-doubling had to be taken into account in order to interpret the experimental data. The positions of spectral lines were converted to the energies of rovibrational levels in the  $6^1\Pi$  and  $7^1\Pi$  states and then processed in the same way as described above for the  $4^1\Pi$  state. In this manner the molecular constants and the equilibrium internuclear distance were determined for each state, and then RKR potential energy curve, with further refinement with IPA technique was constructed. Finally the constructed IPA potentials for the  $6^1\Pi$  and  $7^1\Pi$  reproduced the experimental data within the experimental uncertainty.

Soon after our observations of the highest  $^1\Pi$  state, two papers [79, 80] with comprehensive theoretical calculations of electronic structure of NaLi appeared (August 2008). For low-lying electronic states, below  $4^1\Pi$ , calculated values for molecular constants in both works are quite close to each other, and also close to those determined experimentally by us. However deviations between these two theoretical results increase for higher excited states. Particularly huge discrepancies between the two calculated results can be found for the  $7^1\Pi$  state, where disagreement between the electronic energy is  $1615\text{ cm}^{-1}$ , and  $0.3\text{ \AA}$  between the equilibrium internuclear distances. Such deviations are very big; they exceed what we can expect from the nowadays precise calculations for alkali-metal dimers. Since both theoretical works considered electronic states up to  $\text{Na}(3^2\text{P})\text{-Li}(2^2\text{P})$  asymptote, which correlates to the  $7^1\Pi$  state, we could compare both theoretical results to our experimental ones, and attempted to assess the reliability of both theoretical approaches. The comparison shows much better agreement of our data with the results by Mabrouk et al [79]. For example, if we accept the numbering of the states given in [79], the deviation of the electronic energy for the  $7^1\Pi$  state is only  $5\text{ cm}^{-1}$ , and of the equilibrium distance is  $0.006\text{ \AA}$ . However an unexpected problem appears: if we keep the assignment for the  $^1\Pi$  states following [79] this would mean that we missed the  $5^1\Pi$  state in our observations. This is hardly an acceptable explanation because we did a systematic, careful spectroscopic search thorough the corresponding energy range and it is not probable that we overlooked a few hundred lines. Since there is no clear reason for a particularly small transition dipole moment to the  $5^1\Pi$  state, this would lead us to the conclusion that the position of this state is not well calculated in [79], which also means

that the numbering of the  $^1\Pi$  states is not correct. However, we see some counterargument, namely that the positions of other states in [79] were predicted very well.

If we compare our results for the  $6^1\Pi$  and  $7^1\Pi$  states with those in [80] generally the shift of the positions of PECs is much bigger. But surprisingly, if we accept such discrepancy, the problem of the missing  $5^1\Pi$  state disappears, since another assignment of the highest experimentally observed states is possible, as  $5$  and  $6^1\Pi$  states. Again, an argument against such explanation is the generally bad agreement of theoretical and experimental PECs for both  $5^1\Pi$  and  $6^1\Pi$  states.

At the present moment we do not have a convincing explanation for inconsistency between our and theoretical results described above, and also between the two theoretical calculations. Since from the experimental side nothing more can be done at the moment, we hope for revisiting of the calculations by theoreticians. Since our last results for the  $6^1\Pi$  and  $7^1\Pi$  states are already prepared for publication (until now they have not published in any form) we believe that this will stimulate theoretical reinvestigation of NaLi electronic structure.

## Bibliography

- [1] W. D. Phillips. *Laser cooling and trapping of neutral atoms*. **Rev. Mod. Phys.** **70** (1998) 721-741.
- [2] J. Weiner, V. S. Bagnato and S. Zilio, P. S. Julienne. *Experiments and theory in cold and ultracold collisions*. **Rev. Mod. Phys.**, **71** (1999) 1-85.
- [3] Thorsten Köhler, Krzysztof Góral, and Paul S. Julienne. *Production of cold molecules via magnetically tunable Feshbach resonances*. **Rev. Mod. Phys.** **78**, (2006) 1311.
- [4] V. Wippel, C. Binder, and L. Windholz. *Cross-section for collisions of ultracold  $^7\text{Li}$  with Na*. **Eur. Phys. J. D** **21** (2002) 101-104.
- [5] C. A. Stan, M.W. Zwierlein, C. H. Schunck, S.M. F. Raupach, and W. Ketterle. *Observation of Feshbach Resonances between Two Different Atomic Species*. **Phys. Rev. Lett.**, **93** (2004) 1-4.
- [6] G Auböck, C Binder, L Holler, V Wippel, K Rumpf, J Szczepkowski, W E Ernst and L Windholz. *Trap loss collisions of  $6\text{Li}$  and  $7\text{Li}$  with  $^{23}\text{Na}$  in a combined magneto-optical trap*. **J. Phys. B: At. Mol. Opt. Phys.** **39** (2006) S871–S879.
- [7] W. C. Stwalley and H. Wang. *Photoassociation of Ultracold Atoms: A New Spectroscopic Technique*. **J. Mol. Spectr.**, **195** (1999) 194-228.
- [8] K. M. Jones, E. Tiesinga, P. D. Lett, and P. S. Julienne. *Ultracold photoassociation spectroscopy: Long-range molecules and atomic scattering*. **Rev. Mod. Phys.** **78** (2006) 435.
- [9] J. M. Walter, S. Barrat. *The Existence of Intermetallic Compounds in the Vapor State. The Spectra of the Alkali Metals and their Alloys with Each Other*. **Proc. R. Soc. Lond. A** **119**, 257-275, (1928)

- [10] B. B. Phillips, H. M. Froslic, and R. H. McFarland. *An Investigation of the Existence of a Sodium Lithium Molecule*. **Phys. Rev.** **81** (1951) 898 – 899.
- [11] M. M. Hessel. *Experimental Observation of the NaLi Molecule*. **Phys. Rev. Lett.**, **26** (1971) 215-218.
- [12] F. Engelke, G. Ennen, and k. H. Meiwes. *Laser Induced Fluorescence Spectroscopy of NaLi in Beam and Bulk*. **Chem. Phys.**, **66** (1982) 391-402.
- [13] M. M. Kappe, K. O. Marti, P. Radi, M. Schöp, and E. Scgumacher. *Resonant two-photon ionization of LiNa. Observation and preliminary characterization of five new singlet states*. **Chem. Phys. Lett.**, **107** (1984) 6.
- [14] C.E. Fellows, J.Vergès, and C. Amiot. *The NaLi electronic ground state studied by laser induced fluorescence and Fourier transform spectroscopy*. **Mol. Phys.**, **63** (1988) 1115.
- [15] C.E. Fellows. *The NaLi  $1^1\Sigma^+(X)$  electronic ground-state dissociation limit*. **J. Chem. Phys.**, **94** (1991) 5855-5864.
- [16] C.E. Fellows. *The NaLi  $A(2)^1\Sigma^+$  electronic state: first high-resolution spectroscopic study*. **J. Mol. Spectrosc**, **136** (1989) 369-379.
- [17] C.E. Fellows, J.Vergès, and C. Amiot. *The  $Na^7Li$   $3^1\Sigma^+(C)$  and  $1^1\Pi(B)$  electronic states through collision energy transfer*. **J. Chem. Phys.**, **93** (1990) 6281-6290.
- [18]. W. Jastrzębski, P. Kowalczyk, R. Nadyak, and A. Pashov. *Spectroscopic study of the  $4^1\Sigma^+(E)$  state in NaLi*. **Spectrochim. Acta, Part A**, **58A** (2002) 2193.
- [19] P.J. Bertocini, G. Das, and A. C. Wall. *Theoretical study of the  $^1\Sigma^+$ ,  $^3\Sigma^+$ ,  $^3\Pi$ ,  $^1\Pi$  States of NaLi and the  $^2\Sigma^+$  state of  $NaLi^+$* . **J. Chem. Phys.**, **52** (1970) 5112-5130.
- [20] S. Green. *Electric Dipole Moment of Diatomic Molecules by Configuration Interaction. I. Closed-Shell Molecules*. **J. Chem. Phys.**, **54** (1971) 827-832.
- [21] P. Rosmus and W. Meyer. *Spectroscopic constants and the dipole moment functions for the  $^1\Sigma^+$  ground state of NaLi*. **J. Chem. Phys.**, **65** (1976) 492- 493.
- [22] W. Müller, Joachim Flesch, and W. Meyer. *Treatment of intershell correlation effects in ab initio calculations by use of core polarization potentials. Method and*

- application to alkali and alkaline earth atoms. **J. Chem. Phys.**, **80** (1984) 3297-3310.
- [23] W. Müller and W. Meyer. *Ground-state properties of alkali dimers and their cations (including the elements Li, Na, and K) from ab initio calculations with effective core polarization potentials.* **J. Chem. Phys.**, **80** (1984) 3311-3320.
- [24] I. Schmidt-Mink, W. Muller, and W. Meyer. *Potential energy curves for ground and excited states of NaLi from ab initio calculations with effective core polarization potentials.* **Chem. Phys. Lett.**, **112** (1984) 120-129.
- [25] P. J. Dagdigian, J. Graff, and L. Warton. *Stark effect of NaLi  $X^1\Sigma^+$ .* **J. Chem. Phys.**, **55** (1971) 4980-4982.
- [26] J. Graff, P. J. Dagdigian, and L. Warton. *Electric Resonance Spectrum of NaLi.* **J. Chem. Phys.**, **57** (1972) 710-714.
- [27] R. Teets, R. Feinberg, T. W. Hansch, and A. L. Schawlow. *Simplification of spectra by Polarization Labelling.* **Phys. Rev. Lett.**, **37** (1976) 683.
- [28] W. Jastrzebski and P. Kowalczyk. *Polarization labelling spectroscopy of  $3^1\Pi_u - X^1\Sigma^+_g$  and  $3^1\Sigma^+_u - X^1\Sigma^+_g$  transitions in  $K_2$ .* **Chem. Phys. Lett.**, **206** (1993) 69.
- [29] Pashov, Jastrzebski, and Kowalczyk. *The  $Li_2 F^1\Sigma^+_g$  "Shelf state: accurate potential energy curve based on the inverted perturbation approach.* **J. Chem. Phys.**, **113** (2000) 6624.
- [30] I. Jackowska et al. *Reanalysis of the  $A \Sigma^+_u$  state of  $Na_2$  by polarization labelling spectroscopy.* **Mol. Phys.**, **89** (1996) 1719.
- [31] W. Jastrzebski and P. Kowalczyk. *Potential curves for selected electronic states of  $K_2$  and  $NaK$ .* **Phys. Rev. A.**, **55** (1997) 2438.
- [32] V. Bednarska, I. Jackowska, W. Jastrzebski, P. Kowalczyk. *The Molecular Constants and Potential Energy Curve of the Ground State  $X^1\Sigma^+$  in  $KLi$ .* **J. Mol. Spectrosc.**, **189** (1998) 244-248.
- [33] P. Kortyka, W. Jastrzebski, P. Kowalczyk. *Experimental characterisation of the double minimum  $6^1\Sigma^+$  state in  $NaRb$ .* **Chem. Phys. Lett.**, **404** (2005) 323-326.
- [34] G. Herzberg: *Molecular Spectra and Molecular Structure. Vol. 1: Spectra of Diatomic Molecules.* Van Nostrand, 1950.

- [35] J. Brown and, A. Carrington: *Rotational Spectroscopy of Diatomic Molecules*. Cambridge University Press, 2003.
- [36] B. H. Bransden, and C. J. Joachain: *Physic of Atoms and Molecules*. Longman Scientific & Technical, 1983.
- [37] J. Hirschfelder, C. Curtiss, and R. B. Brird: *Molecular Theory of Gases and Liquids*, John Wiley & Sons, 1954.
- [38] A. Hinchliffe: *Modelling molecular Structure, 2nd*. John Wiley, 2000.
- [39] Y. P. Varshni. *Comparative Study of Potential Energy Functions for Diatomic Molecules*. **Rev. Mod. Phys.**, **29** (1957) 664-682.
- [40] G. Calder and K. Ruedenberg. *Quantitative Correlations between rotational and vibrational spectroscopic Constants in Diatomic Molecules*. **J. Chem. Phys.**, **49** (1968) 5399-5415.
- [41] J. L. Dunham. *Diatomic Molecules According to the Wave Mechanics. II. Vibrational Levels*. **Phys. Rev.**, **34** (1929) 57-64.
- [42] J. L. Dunham. *The Wentzel-Brillouin-Kramers Method of Solving the Wave Equation*. **Phys. Rev.**, **41** (1932) 713-720.
- [43] C. Beckel and R. Engelke. *Power-Series Expansions of Vibrational Potentials. IV. Radii of Convergence*. **J. Chem. Phys.**, **49** (1968) 5199-5200.
- [44] P. Morse. *Diatomic Molecules According to the Wave Mechanics. II. Vibrational Levels*. **Phys. Rev.**, **34** (1929) 57.
- [45] A. S. Coolidge, H. M. James, and E. L. Vernon. *On the Determination of Molecular Potential Curves from Spectroscopic Data*. **Phys. Rev.** **54** (1938) 726 – 738.
- [46] H. Hulbert, and J. Hirschfelder. *Potential Energy Functions for Diatomic Molecules*. **J. Chem. Phys.** **9** (1941) 61-69.
- [47] C. L. Pekeris. *The Rotation-Vibration Coupling in Diatomic Molecules*. **Phys. Rev.** **45** (1934) 98 -103.
- [48] R. Leroy, in: *Molecular Spectroscopy*, Vol 1, Eds. R. F. Barrow, D. A. Long, and D. J. Millen (Chem. Soc., London, 1973).

- [49] M. Marinescu, and H. R. Sadeghpour. *Long-range potentials for two-species alkali-metal atoms*. **Phys. Rev. A** **59** (1999) 390 – 404.
- [50] M. Marinescu and A. Dalgarno. *Dispersion forces and long-range electronic transition dipole moments of alkali-metal dimer excited states*. **Phys. Rev. A** **52** (1995) 311 – 328.
- [51] M. Marinescu and Anthony F. Starace. *Dispersion coefficients for highly excited molecular states of  $K_2$* . **Phys. Rev. A** **56** (1997) 4321 – 4323.
- [52] M. Marinescu. *Dispersion coefficients for the  $nP$ - $nP$  asymptote of homonuclear alkali-metal dimers*. **Phys. Rev. A** **56** (1997) 4764 – 4773.
- [53] Bing Ji, Chin- Chun Tsai, and W. Stwalley. *Proposed modification of the criterion for the region of validity of inverse-power expansion in diatomic long-range potentials*. **Chem. Phys. Lett.** **236** (1995) 242-246.
- [54] W.M. Kosman and J. Hinze. *Inverse Perturbation Analysis: Improving the Accuracy of Potential Energy Curves*. **J. Mol. Spectr.**, **56** (1975) 93-103.
- [55] C.R. Vidal and H. Scheingraber. *Determination of Molecular Constants using an Inverted Perturbation Approach*. **J. Mol. Spectr.**, **65** (1977) 46-64.
- [56] R. J. Leroy and J. V. Kranendonk. *Anisotropic intermolecular potentials from an analysis of spectra of  $H_2$ - and  $D_2$ -inert gas complexes*. **J. Chem. Phys.**, **61** (1974) 4750-4769.
- [57] A. Pashov, W. Jastrzębski, and P. Kowalczyk. *Construction of potential curves for diatomic molecular states by the IPA method*. **Comp. Phys. Comm** **128** (2000) 622.
- [58] R. J. Leroy: *Computer programs* @: <http://leroy.uwaterloo.ca/programs/>.
- [59] P. Bernath: *Spectra of Atoms and Molecules*. Oxford University Press, 1995.
- [60] I. Kovács: *Rotational Structure in the Spectra of Diatomic molecules*. Akadémiai Kiadó, Budapest 1969.
- [61] H. Lefebvre-Brion and R. Field: *Perturbations in the Spectra of Diatomic Molecules*. Academic Press, 1986.
- [62] W. Kołos, and L. Wolniewicz. *Nonadiabatic Theory for Diatomic Molecules and Its Application to the Hydrogen Molecule*. **Rev. Mod. Phys.** **35** (1963) 473 - 483.

- [63] N.C. Handy, Y. Yamaguchi, and H. F. Schaefer III. *The diagonal correction to Born-Oppenheimer approximation: Its effect on singlet triplet splitting of CH<sub>2</sub> and other molecular effects.* **J. Chem. Phys.**, **84** (1986) 4481- 4484.
- [64] W. Demtröder: *Laser spectroscopy*, 3<sup>rd</sup>, Springer 2003.
- [65] C. Wieman and T. W. Hansch. *Doppler - Free Laser polarization Spectroscopy*, **Phys. Rev. Lett.**, **36** (1976) 1170.
- [66] M. E. Kaminsky, R. T. Hawkins, F. V. Kowalski, and A. L. Schawlow. *Identification of Absorption Lines by Modulated Lower-Level Population: Spectrum of Na<sub>2</sub>*, **Phys. Rev. Lett.**, **36** (1976) 671.
- [67] R.E. Drullinger and R. N. Zare. *Optical Pumping of Molecules.* **J. Chem. Phys.**, **51** (1969) 5532.
- [68] W. Happer. *Optical Pumping.* **Rev. Mod. Phys.**, **44** (1972) 169.
- [69] W. Carlson, A. J. Taylor, K. M. Jones, and A. L. Schawlow. *Two-step polarization-labelling spectroscopy of excited states of Na<sub>2</sub>.* **Phys. Rev A.** **24** (1981) 822.
- [70] G. Wang and H. R. Xia: *Molecules and Laser Spectroscopy*, Springer, Berlin, 1991.
- [71] R. E. Drullinger and R. N. Zare: *Optical Pumping of Molecules II. Relaxation studies.* **J. Chem. Phys.**, **59** (1973) 4225.
- [72] R. Ferber, W. Jastrzębski, and P. Kowalczyk. *Line Intensities in V-type Polarization Labelling Spectroscopy of Diatomic molecules,* **J. Quant. Spectros. Radiat. Transfer**, **58** (1997) 53-60.
- [73] V. Bednarska, I. Jackowska, W. Jastrzębski, and P. Kowalczyk. *A three-section heat-pipe oven for heteronuclear alkali molecules.* **Meas. Sci. Technol.**, **7** (1996) 1291-1293.
- [74] R. Strianov and G. A. Odincova. *Tablicy Spektralnych Linii Atomov i Ionov* (Energoizdat, Moscow 1982).
- [75] S. Bashkin and J. O. Stoner. *Atomic energy levels and Grotrian diagram*, Vol 1. North- Holland 1975.
- [76] H. Press, S. A. Teukolski, W. T. Vetterling, B. P. Flannery. *Numerical Recipes in Fortran 77.* **Cambridge University Press, 1992.**

- [77] J. H. Van Vleck. *The Coupling of Angular Momentum Vectors in Molecules*. **Rev. Mod. Phys.**, **23** (1951) 213-227.
- [78] A. Mulliken and A. Christy. *A-Type Doubling and Electron Configurations in Diatomic Molecules*. **Phys.Rev.****38** (1931) 87-119.
- [79] N. Mabrouk and H. Berriche. Theoretical study of the NaLi molecule: *potential energy curves, spectroscopic constants, dipole moments and radiative lifetimes*. **J. Phys. B: At. Mol. Opt. Phys.** **41** (2008) 155101.
- [80] I. D. Petsalakis, D. Tzeli, and G. Theodorakopoulos. *Theoretical study on the electronic states of NaLi*. **J. Chem. Phys.**, **129**, 054306 (2008).